SINGLE-MOLECULE MICROSCOPY STUDIES OF INTERACTIONS BETWEEN ALZHEIMER'S AMYLOID-β (1-40) AND AMYLOID-β (1-42) ON THE MEMBRANE

by

Chun-Chieh Chang

A dissertation submitted in partial fulfillment
of the requirements for the degree of
Doctor of Philosophy
(Biophysics)
in the University of Michigan
2014

Doctoral Committee:

Professor Ari Gafni, Co-Chair
Professor Duncan G. Steel, Co-Chair
Assistant Professor Michael M. A. Sutton
Assistant Professor Sarah Veatch
Professor Kristen J. Verhey

DEDICATION

This work is dedicated to my parents, Chien-Chen Chang and Bi-Chu Kuan, who raised a little boy and support him flying oversea to pursue his dream.

ACKNOWLEDGMENTS

I would like to express my sincere appreciation and thanks to my gracious and respectful advisors, Professor Ari Gafni and Duncan Steel. Their training in critical thinking, supports in my future career, and mentoring in the attitude of becoming a better scientist have nourished me during the past five years. Their sense of humor also makes me enjoy my work and be creative. I would also like to thank all my thesis committee, Professors Kristen Verhey, Michael Sutton, and Sarah Veatch for serving as the scientific council and providing valuable ideas.

Brilliant, fun and thoughtful co-workers also fill up the joy in Chem 4070. I would like to thank the current graduate student Kian Kamgar-Parsi for discussions in experimental design, programming, and fun YouTube clips as well. Thanks to undergraduate Kaylee Van Dommelen for the help of culturing SH-SY5Y cell lines. I would like to express my deep and grateful appreciations to previous Gafni/Steel lab members who are also lifelong friends; Kathleen Wisser and Joseph Schauerte, Ph.D., were great co-workers and mentors who taught me everything that I needed to learn to become an independent researcher. They also served as a family who took care of my life outside the research. I would like to thank Dr. Robin Johnson for valuable scientific discussions and establishing the first single-molecule live-cell imaging protocol in the lab. Dr. Johnson's research attitude is what I always look up to. Thanks to Dr. Pam Wong and Pavithra Aravamudhan for bringing the fun to every Gafni/Steel lab's social event. Without all these beloved members, my research life in Chem 4070 could not be accomplished with blessed.

Collaborators are an essential part for great research. I would like to thank John Christian Althaus and Cynthia J. L. Carruthers from Professor Sutton's lab for preparing rat's primary neuronal cells with excellent quality and consistency. I would also like to thank Dr. Elin Edwald for thorough guidance for the particle tracking algorithm and data

interpretation even during the preparation period of her dissertation defense. I appreciate Dr. Krishnan Raghunathan for the generous help of the dissertation preparation, and I thank to people in Veatch's lab for sharing the cell culture room. I also would like to thank David Rowland for the help of simulating particle diffusion movies which validated the particle tracking algorithm and analysis.

Being part of the Biophysics and a student at the University of Michigan is proud. I have to thank all the Biophysics 2009 fellows, Teppei Shirakura, Leela Ruckthong, Josh Jasensky, Veronica Taylor, Stephen Norris, and Anthony Mustoe for fighting for the homework and sharing research and fun. I would like to thank the Biophysics staff, Sara Grosky and Ann Titus, for taking care of my student life. As a teaching assistant for five semesters, I have to thank to all the biophysics faculties and students for giving me the opportunity to learn and grow. I would especially thank all the friends from Michigan Taiwanese Student Association, Optical Society at the University of Michigan, and Taiwan Biomedical Journal Club. These five years in Michigan cannot be more wonderful without those memorable funs and supports.

Finally, family is everything. I would like to give my sincere thanks to my parents for their unconditional love and support for almost three decades. I would also like to thank my caring, loving, and supportive wife, Tzu-Hui Wang. Your sweet laughter and encouragements are the driving force toward the completion of my PhD and our better future.

TABLE OF CONTENTS

LIST OF FIGURES

ABSTRACT

Two amyloid-β peptides (Aβ40 and Aβ42) feature prominently in the extracellular brain deposits associated with Alzheimer's disease. While Aβ40 is the prevalent form in the cerebrospinal fluid, the fraction of Aβ42 increases in the amyloid deposits over the course of disease development. The low *in vivo* concentration (pM-nM) and metastable nature of Aβ oligomers have made identification of their size, composition, cellular binding sites and mechanism of action challenging and elusive. Furthermore, recent studies have suggested that synergistic effects between Aβ40 and Aβ42 alter both the formation and stability of various peptide oligomers and as well as their cytotoxicity. These studies often utilized Aβ oligomers that were prepared in solution and at μM peptide concentrations. Here we utilized various single-molecule microscopies to follow peptide binding and association on the model membrane as well as the primary cultured neurons under physiological Aβ concentrations. At these concentrations monomers constitute the dominant Aβ species in solution. These monomers tightly associate with the model membrane and are highly mobile, whereas trimers and higher-order oligomers are largely immobilized. The Aβ dimer appears to exist in a metastable state that can be either mobile or immobile. Additionally, oligomer growth on the model membrane occurs more rapidly for Aβ40 than for Aβ42 while oligomer growth is largely inhibited for a 1:1 Aβ40:Aβ42 mixture. Interestingly, when the neuronal cells were exposed to a 1:1 mixture of nM Aβ40:Aβ42, significantly larger membrane-bound oligomers developed compared to those formed from either peptide alone. Fluorescence resonance energy transfer experiments at the single molecule level reveal that these larger oligomers contained both Aβ40 and Aβ42, but that the growth of these oligomers was predominantly by addition of Aβ42. Both pure peptides form very few oligomers larger than dimers, but either cell membrane bound Aβ40/42 complex, or

Aβ40, bind Aβ42 to form increasingly larger oligomers. These findings provide a hypothesis for the structural differences between Aβ42, Aβ40 and different oligomers, which may explain how Aβ42-dominant oligomers, suspected of being more cytotoxic, develop on the neuronal membrane under physiological conditions.

CHAPTER 1

INTRODUCTION

1-1 Alzheimer's Disease at a Glance

Alzheimer's disease (AD) was first documented by the German psychiatrist Alois Alzheimer in 1901 and represents the most common form of dementia (which accounts for 50–80% of dementia cases), which affects memory loss and other intellectual abilities, particularly in people age 65 or older. However, this disease does not represent a normal aging process. Approximately 5% of Alzheimer's patients exhibit early-onset memory loss in the age range of 40s to 50s. However, effective treatments to prevent, halt, or reverse AD currently remain unavailable. Moreover, certain treatments produce even more severe side effects (1). By 2025, the number of Alzheimer's patients age 65 and older in the United States is predicted to reach 7.1 million, which is a 40% increase from the 5 million people age 65 and older who are currently affected.

Due to extensive research over the past three decades, two abnormal structures, *i.e.*, plaques and tangles, have been identified as key factors that lead to neuronal cell death specifically around the hippocampus region. The plaques consist of large deposits of the fibrillar form of a protein fragment, amyloid-beta (Aβ), which accumulate in the spaces between nerve cells, whereas the tangles, which are twisted fibrillar aggregates of another protein, tau, accumulate within cells. Studies have demonstrated that Aβ may trigger tau hyperphosphorylation, which eventually results in the development of fibrillar tangles (2) and highlights the importance of Aβ.

This thesis focuses on unraveling the molecular mechanisms of Aβ associations using biophysical techniques. Chapter 1 begins by introducing Aβ production, structure, aggregation (termed 'oligomerization' for small aggregates), and possible cell-killing mechanisms as well as the importance of different Aβ isoforms.

1-2 Amyloid-β Production

Aβ peptides consist of between 36 to 43 residues and are generated through proteolytic processing of the amyloid precursor protein (APP). This proteolytic processing occurs through sequential enzymatic cleavage. First, a β-secretase, β-site amyloid precursor protein–cleaving enzyme 1 (BACE-1), removes the APP N-terminal segment. Secondly, γ-secretase, which is a protein complex that contains presenilin-1 at its catalytic core, produces Aβ peptides of different lengths (Figure 1-1) (3).

Several studies suggest that Aβ modulates neuronal and synaptic activities, in which Aβ accumulation in the brain causes an intriguing combination of aberrant network activity and synaptic depression (4). Inhibitory interneuron impairment and aberrant glutamate receptor stimulation, which can result in excitotoxicity, play important upstream roles in this pathogenic cascade (4–6). Aberrant neuronal activity may trigger a vicious positive feedback cycle by augmenting Aβ production, leading to aberrant neuronal activity (7). The immediate-early gene Arc, which directly binds presenilin-1 (PS1) to regulate γ-secretase trafficking, is required for neuronal activity-dependent Aβ production (8). Sections 1-6 will discuss the importance and overproduction of longer Aβ sequences, which specifically increases the Aβ42/Aβ40 ratio due to mutations in the APP gene and/or the gene encoding the γ-secretase complex component PS1.

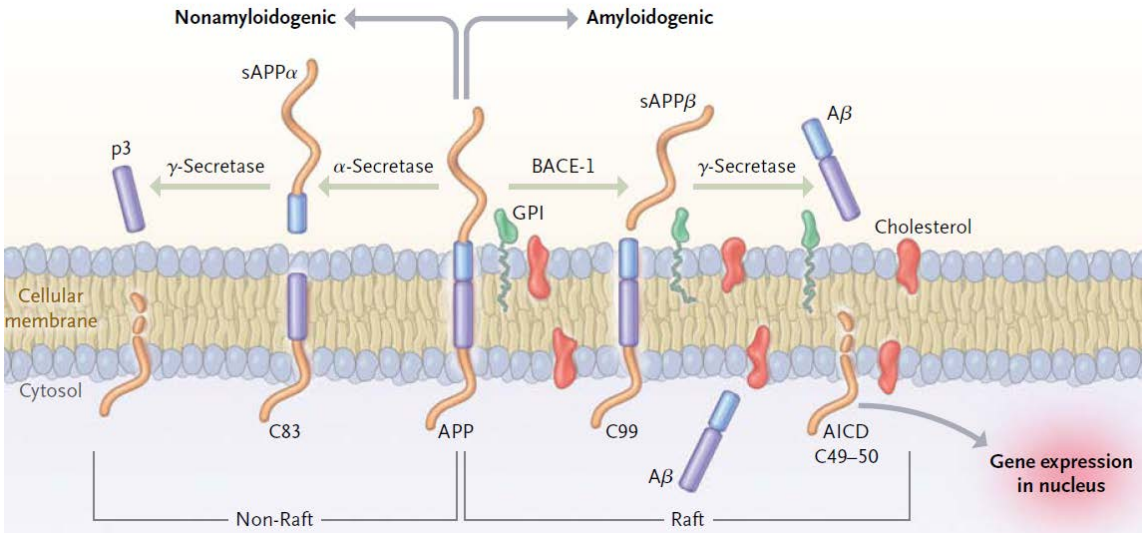

Figure 1-1. Aβ production pathway. Cleavage by α-secretase within the Aβ sequence initiates nonamyloidogenic processing. A large amyloid precursor protein (sAPPα) ectodomain is released, and an 83-residue carboxy-terminal fragment (C83) remains. C83 is subsequently digested by γ-secretase, which liberates extracellular p3 and the amyloid intracellular domain (AICD). Amyloidogenic processing is initiated by the β-secretase beta-site amyloid precursor protein–cleaving enzyme 1 (BACE-1), which releases a shorter sAPPα (sAPPβ). The retained C99 is cleaved by γ-secretase substrate, which generates Aβ and AICD. γ-secretase cleavage occurs within the cell membrane through a unique process termed "regulated intramembranous proteolysis." sAPPα and sAPPβ are APP fragments that are secreted after α-secretase and β-secretase cleavage, respectively. AICD is a short tail (approximately 50 residues) that is released into the cytoplasm after progressive cleavages by γ-secretase. AICD is targeted to the nucleus, which signals transcription activation. The lipid rafts are tightly packed membrane microenvironments enriched in sphingomyelin, cholesterol, and glycophosphatidylinositol (GPI)–anchored proteins. Soluble Aβ is prone to aggregation. Adapted from (9).

1-3 Structural Differences between Amyloid-β Isoforms

Proteolytic processing of APP produces more Aβ40 monomers (Aβ containing 40 residues, as shown in Figure 1-2) than the aggregation-prone and deleterious Aβ42

species (Aβ containing 42 residues). Numerous studies have demonstrated that when Aβ42 is incubated in solution at μM concentrations, it exhibits a considerably higher fibril formation rate than Aβ40 (10–13) and forms larger, more cytotoxic oligomers (14–16). Although these two peptides differ only in two additional hydrophobic residues, *i.e.*, Ile-41 and Ala-42, at the Aβ42 C-terminus, Aβ42 is more prevalent in the insoluble aggregates detected in diseased brains and causes more extensive damage to neuronal cell cultures than Aβ40 (17–22). These observations demonstrate that the presence of these two C-terminal residues significantly affects the physiological and biophysical behavior of the two peptides.

Monomeric forms of Aβ40 and Aβ42 have been classified as intrinsically disordered peptides (IDPs), which means that instead of existing as a single folded structure, they populate a diverse set of conformational states (23–25). On the other hand, the fibrillar form of Aβ40 and Aβ42 adopt highly structured array of β-strands running orthogonal to the fibril axis. They further assemble into intermolecular β-sheets that can extend to microns in length (26–31). Although Aβ40 and Aβ42 adopt similar fibrillar structures, the fibrillization speed for Aβ42 is much faster than Aβ40 under the same incubation condition. Differences in the monomeric conformational ensembles govern the speed of aggregation of both Aβ40 and Aβ42 (32, 33). Experimental and theoretical results have shown that the two additional C-terminal hydrophobic residues of Aβ42 sharply increase the hydrophobic clustering between residues 39–40 and 31–36 as compared to Aβ40. Especially when Ile-41 is included, the number of structures with hydrophobic contacts with 31–36 increases to a decisive hydrophobic clustering, which is directly responsible for the differences in the populations of secondary structure of the two amyloid peptides (34, 35). Moreover, Lazo et al. showed that the Aβ42 C-terminus is resistant to proteolytic digestion (36). Taken together, these observations may explain why the nucleation step for fibrillization may be more difficult for Aβ40 compared to Aβ42.

To date, monomeric and fibrillar forms of Aβ40 and Aβ42 have been structurally characterized in solution. However, structures of membrane-bound small oligomers, which are more directly related to the toxicity discussed in Section 1-5, have not been

characterized because they are heterogeneous, metastable, and continuously interconvert. This thesis will describe how single-molecule microscopy explores the structures of membrane-bound oligomers even when heterogeneity exists.

Figure 1-2. Sequence of Aβ40 and Aβ42. Aβ40 starts from N-terminus to 40th amino acid (Valine) and Aβ42 has additional Isoleucine and Alanine.

1-4 Membranes Accelerate Aβ Aggregation

Aβ interacts with the cell membrane soon after its production by cleavage of the transmembrane amyloid precursor protein. Numerous studies have indicated that binding to phospholipid membranes can accelerate Aβ oligomerization by increasing the local Aβ concentration, stabilizing the Aβ structure, and decreasing the potential barrier for additional oligomerization (37, 38). Because Aβ is a cationic peptide, the initial membrane binding event is largely driven by electrostatic interactions between the basic side chains and the anionic lipid head groups (37, 39). Additional hydrophobic interactions occur between the embedded Aβ C-terminal region and the lipid tail groups, and the subsequent accumulation of the pepetide at the membrane surface increases the local protein concentration and facilitates aggregation (39). The ability of membranes to induce regions of locally concentrated proteins is termed “molecular crowding” (40). In addition to increasing the local protein concentration, other factors have been proposed to play a role in membrane-mediated fibrillogenesis. Adsorption of the unfolded amphipathic peptide on the membrane surface may reduce the peptide conformational entropy and generate structural ordering, thereby inducing secondary structure formation (41). A decrease in the local solvent dielectric constant through the membrane surface microenvironment may facilitate peptide–peptide hydrogen bond formation in the β-sheet aggregate (42). A reduction in the dimensionality from three dimensions in solution to approximately two dimensions at the membrane interface also introduces spatial

restrictions that favor the fibril formation pathway (40). Therefore, depending on the membrane composition and chemical properties, membranes can provide a template to accelerate the aggregation of misfolded amyloidogenic peptides (43). For these reasons and because most cell toxicity mechanisms involve the membrane, this thesis focuses on membrane-bound Aβ and the comparison with Aβ in solution.

1-5 Amyloid Hypothesis and Aβ Toxicity

An imbalance between Aβ production, aggregation, and clearance results in the accumulation of Aβ peptides. Aβ accumulation may represent the initiating factor in Alzheimer's disease, which is referred to as the "amyloid hypothesis" and is based on studies of genetic forms of Alzheimer's disease, including Down's syndrome (44), and evidence that Aβ is toxic to cells (45, 46).

Initial reports that the extent of amyloid plaques correlated with AD severity led to the amyloid hypothesis, which proposes AD may be caused by deposition of Aβ in plaques and fibrils in brain tissue; however, recent extensive studies have revealed that neuronal damage is associated with small, oligomeric Aβ species, which has led to the peptide oligomer hypothesis (47–53). Notably, little or no correlation was observed between the total Aβ peptide deposited in brain plaques and the level of neurodegeneration in patients (54, 55). This discrepancy has been more recently confirmed using modern amyloid imaging techniques (56, 57). Plaques and fibrils are biologically inert but serve as a reservoir that decomposes into soluble aggregates that exhibit different levels of toxicity depending on their conformation (58, 59). Stable versions of Aβ dimers or dimer aggregates reduce long-term potentiation in cultured neurons (59, 60), and a comparison of crosslinked Aβ dimers, trimers, and tetramers revealed that neurotoxicity increases nonlinearly with oligomer size (61). A 56-kDa Aβ species is neurotoxic in Tg2576 mice (62); lipid-induced oligomers from mature fibrils (58), ADDLs (63–65), and annular assemblies (66) exert neurotoxic effects as well as affect synapse function and memory formation in mice. Notably, the reported "soluble oligomers" are stable with defined structures. However, the physiological amyloid

aggregation begins with monomeric Aβ production, which further aggregates into an oligomer. This process occurs under a thermodynamic equilibrium, and the species continuously interconvert. Therefore, alternatively, toxicity may be due to a series of conformers or sizes (58, 61, 67).

Two primary mechanisms have been proposed to explain this cytotoxicity, and both lead to the disruption of Ca^{2+} homeostasis. The first mechanism is amyloid-mediated membrane permeabilization, in which the toxicity of amyloid-forming proteins is directly correlated with their shared ability to disrupt membrane barrier function. An initial discovery by Arispe and coworkers demonstrated that Aβ exhibits ion-channel activity in planar lipid bilayers, wherein Aβ toxicity is based on an ion-channel mechanism that causes membrane depolarization, Ca^{2+} leakage, and a disruption of ionic homeostasis (68–74). Channel activity was also later reported for other amyloidogenic proteins, including IAPP (which is involved in Type 2 diabetes) (73), α-synuclein (which is involved in Parkinson's disease) (75–77), polyglutamine (78), and prion-derived peptides (79). Thus, the toxicity caused by these proteins may be related to channel or pore formation in membranes, which produces ion leakage that is similar to pore-forming toxins (69, 80, 81). This conclusion is consistent with observations that a disruption of Ca^{2+} homeostasis is characteristic of several neurodegenerative diseases, including Alzheimer's and Parkinson's disease (82). Direct visualization of annular (*i.e.*, ring-like) oligomeric protofibril structures of several amyloidogenic proteins using electron and atomic force microscopy has provided additional evidence for the increasingly accepted amyloid-pore hypothesis (Figure 1-3) (66, 68, 80, 83). Although the disruptive effect of amyloidogenic proteins on membranes has been clearly demonstrated, the exact mechanism of pore formation and permeation by Aβ peptides at the membrane is not fully understood. Several chemical similarities between Aβ and antimicrobial peptides, such as an amphipathic structure, support other membrane-disrupting models. For example, several studies suggest that prefibrillar aggregates do not fully penetrate the membrane but rather associate with the membrane surface, where they induce membrane thinning and leakage (Figure 1-3) (84–86). Furthermore, the pore may not be a static structure but rather an intermediate state followed by other processes, such as detergent-like membrane dissolution (87–89). These transient pore structures are characteristic of

the mechanisms of several antimicrobial peptides and may relate to amyloidogenic protein activity (90, 91).

The second mechanism of Aβ induced toxicity may associate with specific cellular receptors or protein complexes (*e.g.*, NMDA receptors (92, 93), α7 nicotinic acetylcholine receptors (94), the receptor tyrosine kinase EphB2 (95), and the receptor for advanced glycation end products (96)), may associate with phosphatidylserine in the membrane (97), or may bind and insert directly into the lipid bilayer (37, 70, 98). Potential downstream mechanisms include alterations in the distribution or activity of neurotransmitter receptors and related signaling molecules (4, 99–102), disruption of intracellular calcium homeostasis (103), and impairment of axonal transport and mitochondrial functions (9, 104–107).

It is important to mention that studies that use physiological concentrations of Aβ peptides are experimentally challenging because they require that cell–bound Aβ species be monitored over long periods of time at nanomolar to picomolar levels, which is beyond conventional detection limit; the cell-disrupting peptides (which are likely a minority) must be individually identified, and the peptide size, composition, and cellular interactions must be characterized. Chapter 2 provides quantitative single-molecule microscopy methods to characterize these oligomeric states.

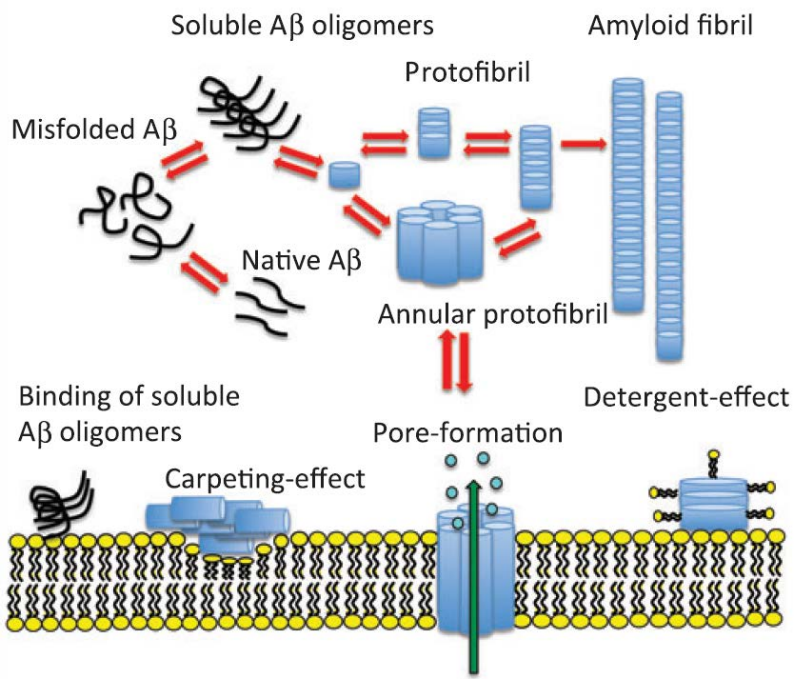

Figure 1-3. Schematic diagram depicting three possible mechanisms of Aβ-induced membrane damage: carpeting, pore formation and the detergent effect. Adapted with permission from Butterfield and Lashuel (108).

1-6 Aβ42:Aβ40 Ratio, Interaction, and Toxicity

Aβ40 peptides are produced in the brain at 10-fold greater level than the aggregation-prone and deleterious Aβ42 species. However, the latter has garnered more interest due to the observation that familial AD patients exhibit strongly stimulated Aβ42 production. Studies have demonstrated that mutations in the APP gene and/or the gene encoding the γ-secretase complex component presenilin, increase Aβ42 production relative to Aβ40 (20, 109, 110). Bentahir et al. reported that clinical presenilin mutations do not necessarily increase Aβ production (111), but they primarily affect the spectrum of Aβ peptides generated by γ-secretase, *i.e.*, they increase the proportion of Aβ42 produced. Because patients with presenilin mutations present an early and aggressive form of the disease, it is logical to propose that the absolute quantity of Aβ peptides produced in the brain may be less important than the quality of Aβ peptides (which is reflected in an altered Aβ42 to Aβ40 ratio) that generates the elusive toxic Aβ species (112). A higher

Aβ42:Aβ40 ratio appears to coincide with more aggressive forms of the disease in comparison to sporadic AD cases (113) and affects synaptic activity, neuronal cell viability, and memory formation in animals (109, 110, 114–116). A lower Aβ42:Aβ40 ratio protects neurons from the deleterious effects of Aβ42 (116, 117). The implications of this hypothesis for current drug development efforts is important because decreasing the absolute levels of Aβ in patients would be less crucial than restoring the correct Aβ peptide ratio.

The molecular mechanisms underlying the synergistic interaction between Aβ42 and Aβ40 are currently poorly understood and under investigation. As previously discussed, Aβ42 is highly fibrillogenic and more prone than Aβ40 to form neurotoxic assemblies (10, 14, 118, 119). Nuclear magnetic resonance (NMR) spectroscopy (28), electron microscopy (EM) (120), and X-ray fiber diffraction methods (30, 121, 122) have been used to discern different architectures for *in vitro*-generated amyloid fibrils from pure Aβ40 and Aβ42 peptides. However, minor alterations in the Aβ42:Aβ40 ratio dramatically influence neurotoxic oligomer formation (10, 11, 123). A limited number of studies have proposed that Aβ42 and Aβ40 affect the aggregation rate of the other; for example, Aβ40 inhibits Aβ42 aggregation (116, 117, 123–129).

To date, most structural and biophysical studies have been performed using Aβ40 or Aβ42 in isolation or at concentrations that are at least 100-fold higher than physiological Aβ concentrations. Little is known regarding the possible cooperative interactions between Aβ42 and Aβ40 under *in vivo* conditions, and their biological outcome. Furthermore, although the Aβ42:Aβ40 ratio affects oligomerization, studies have not addressed how oligomers that contain a mixture of Aβ40 and Aβ42 develop on the cell membrane and potentially cause cytotoxicity. Chapters 3 and 4 will review the current research limitations and discuss single-molecule methods to overcome these hurdles and to directly quantify the Aβ42 and Aβ40 stoichiometry at the cell membrane.

1-7 Thesis Summary

The above reviewed potential pathways that lead to neuronal cell death are based on intense Alzheimer's research over the last decade. However, the elucidation of the physiological molecular mechanism underlying Aβ-membrane interactions requires overcoming current research limitations. For example, due to detection limitations, the higher Aβ concentrations (μM versus nM) that are often used in most studies may yield different aggregation kinetics in comparison to other physiological mechanisms. The term "toxic oligomer" remains ambiguous and even controversial; the interpretation and direct comparison of results from different studies is impossible because a consensus on an experimental description for the toxic Aβ oligomer is lacking. Even if a consistent protocol to produce oligomers were established, it is not known if these preformed oligomers accurately represent the oligomers formed in patient brains. It also is not known if the size and stoichiometry of Aβ42:Aβ40 in solution identical to those of the species that bind to the membrane. Therefore, the ability to directly monitor and quantify the individual Aβ oligomer at the membrane is essential. These concerns highlight the importance of single-molecule microscopy.

Chapter 2 describes single-molecule microscopy and related methodologies that are designed to overcome the current aforementioned limitations in Alzheimer's research. For example, total internal reflection fluorescence (TIRF) microscopy, fluorescence lifetime confocal microscopy, the quantification of oligomer size (*i.e.*, the number of monomeric peptides), a particle tracking algorithm, and the preparation of platforms that mimic physiological protein-membrane interactions. Chapter 3 introduces a model membrane system to study the aggregation kinetics of Aβ40, Aβ42, and a mixture of Aβ42/Aβ40 in solution and at the membrane. A comparison between the membrane-bound oligomeric species formed by Aβ40 and Aβ42 yields information on the effect of the two additional Aβ42 residues on peptide-peptide and peptide-membrane interactions. Furthermore, the dimer contains two distinct populations, mobile and immobile, which suggests the dimer may serve as an important building block. Additionally, membrane-bound Aβ species predominantly consist of dimers and higher-order oligomers, whereas only monomers are present in solution. This result provides structural insights into the

different oligomeric species. After determining the possible fundamental mechanisms for oligomer formation at the model membrane, Chapter 4 extends the single-molecule studies to include conditions that more closely resemble the physiological environment by utilizing rat primary hippocampal neuronal cells. Fluorescence resonance energy transfer (FRET) between Aβ40 and Aβ42 was measured to distinguish stoichiometric interactions. The results indicate that higher-order oligomers contain both Aβ40 and Aβ42, but the oligomers predominantly formed upon the addition of Aβ42. Both pure peptides form few oligomers that are larger than dimers, but either the membrane-bound Aβ42/Aβ40 complex or Aβ42 binds Aβ40 to form increasingly larger oligomers. These findings may explain how Aβ42-dominant oligomers, which may be more cytotoxic, develop at the neuronal membrane under physiological conditions. Finally, Chapter 5 concludes on results from experiments that range from a model membrane to neuronal cells and provides a hypothesis for the structural differences between Aβ42, Aβ40 and different oligomers. Implications from our studies may also explain the toxicity from different oligomers and Aβ42:Aβ40 ratios observed in several studies. Potential future directions are also discussed. Finally, the methodologies developed herein are not limited to Alzheimer's research and are applicable to several other protein-membrane studies.

CHAPTER 2

METHODS

2-1 Rationale for the Selection of Single-Molecule Microscopy

Chapter 1 introduced Alzheimer's research and certain obstacles in these studies, wherein single-molecule microscopy was mentioned as a potential solution for several unanswered questions. As the name suggests, single-molecule microscopy is a technique that allows the identification of individual proteins, DNA, and RNA, among other molecules, depending on the species that is labeled with the fluorescent dye. To study Aβ-membrane interactions, Aβ is labeled with a fluorescent dye that emits fluorescence upon laser excitation at a specific wavelength. The laser light and fluorescence emission are separated by a series of filters, and the fluorescence can be detected through highly sensitive detectors, such as a charge-coupled device (CCD) or an avalanche photodiode (APD), depending on the microscopy technique used. The key factor for the resolution of single molecules that are smaller than the diffraction limit is an enhanced signal-to-noise ratio in comparison to conventional fluorescence microscopy; this ratio is determined by factors that include a strong photoresistant dye, a low density for the labeled species (*i.e.*, a concentration of nanomolar or lower for good spatial resolution), a highly sensitive photon detector, an objective with high numerical aperture (NA), and a coherent laser source (130). Total internal reflection microscopy and confocal microscopy are two common techniques used in single-molecule studies and are briefly reviewed in the following sections.

Conventional fluorescence microscopy measures an ensemble fluorescence signal, which is the average signal from a labeled species (*e.g.*, the average fluorescence intensity of labeled Aβ in solution). In contrast, single-molecule microscopy identifies and classifies individual Aβ species that exhibit different fluorescence intensities; therefore, sample heterogeneity can be characterized without overlooking important species. This aspect is important for Aβ studies because Aβ exists as a mixture of metastable species, and its physiological concentration is approximately pM-nM (47, 48). To study Aβ-membrane interactions, a platform and an appropriate single-molecule method must be designed. A synthetic model membrane combined with total internal reflection microscopy is described first followed by an advanced system using primary hippocampal neuronal cells combined with fluorescence lifetime confocal microscopy.

2-2 Model Membrane System

Given the inherent complexity of biological membranes, many scientists rely on structurally and compositionally simplified model membrane systems. These systems provide the flexibility to systematically manipulate the chemical composition and fluidity of the membrane and monitor the resulting alterations in protein binding and permeabilization activity (131, 132). Model membranes differ from biological membranes in that they lack components such as integral membrane proteins and polysaccharides that may interfere with experimental results and their interpretation. Therefore, model membranes are the preferred systems to determine the specific effects of proteins on lipid membrane components in a systematic, controlled manner. The major disadvantage of model membranes is that the complex array of biochemical processes that influence protein activity cannot be fully represented using model membrane systems alone. Rather, model membrane systems provide a platform to investigate select protein–membrane interactions and key mechanistic events that underlie biological activity. These systems facilitate the interpretation of experimental observations and the development of mechanistic models, and new hypotheses can be subsequently evaluated under more complex biological conditions.

2-2-1 Preparation of a Supported Lipid Bilayer

The cell membrane is composed of approximately 20% anionic lipids in the cytoplasmic leaflet of the plasma membrane (133). To mimic this anionic feature, a lipid composition of 20% 1-palmitoyl-2-oleoyl-*sn*-glycero-3-[phospho-rac-(1-glycerol)] (POPG), which is a liquid phase anionic lipid molecule at room temperature, and 80% 1-palmitoyl-2-oleoyl-*sn*-glycero-3-phosphocholine (POPC), which is a neutral lipid, was used. The lipid bilayer is formed through the rupture of small unilamellar vesicles (SUVs), as shown in Figure 2-1 (134, 135). Freshly prepared and labeled Aβ was subsequently introduced into the sample at a final concentration of 4 nM and was incubated for either 24 or 120 hours. The Aβ solution was gently washed off prior to imaging.

POPC and POPG (Avanti Polar Lipids, Alabaster, AL) were stored at -20°C. 1.6 mg POPC and 0.4 mg POPG were co-dissolved in chloroform, and then dried under gaseous nitrogen in a fume hood. A further removal of residual chloroform was achieved by vacuum drying of the sample overnight. Before the preparation of SUVs, the dried lipids were hydrated in buffer (10mM sodium phosphate and 100mM sodium chloride, pH 7.4) with the concentration of 2 mg/mL for 2 hours at room temperature, during which the sample was vortexed a few times to completely re-suspend the lipids. Lipid solution was stored at -80°C for later use. SUVs were formed by sonication of the lipid suspension in an ice water bath for 2-5 minutes until the suspension became clear. Finally the supported lipid membranes were spontaneously assembled by incubating 400 μL freshly prepared SUVs (final concentration was 1 mg/mL) on a pre-cleaned coverglass overnight. After the formation of the supported lipid membrane, the unbound SUVs were gently washed off with buffer.

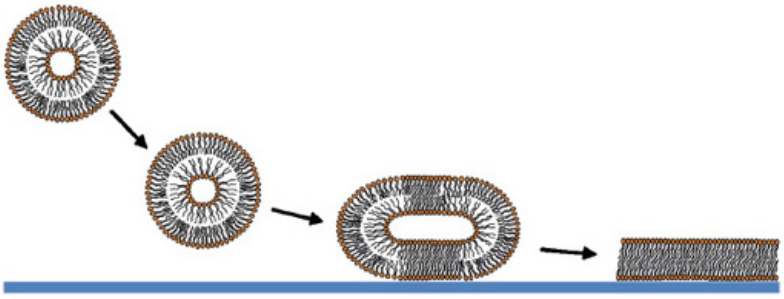

Figure 2-1. Formation of lipid bilayer on a cover glass. Picture is adapted from (136).

2-2-2 Glass Cleaning

A clean and hydrophobic glass surface is essential for successfully forming fluid lipid bilayer. 25mm coverglasses (Fisher Scientific, Pittsburgh, PA) were washed in 10% Liqui-Nox (Alconox, White Plains, NY), laboratory graded detergent, using an ultrasonic water bath for 30 minutes. Detergent was then washed off by rinsing the coverglass with deionized water. And the ultrasonic cleaning cycle is repeated in the order of 1M potassium hydroxide, ethanol, and acetone. The coverglass was rinsed in water and dried it in the oven at 80°C for 15 minutes (53). Finally, the coverglass was kilned at 500°C for two hours. The kilning oxidizes the glass leaving a hydrophilic surface.

2-3 Total Internal Reflection Fluorescence (TIRF) Microscopy

In contrast to epifluorescence microscopy, TIRF presents the advantage that the induced evanescent wave (an illumination depth of less than 100 nm) eliminates the background fluorescence from outside of the focal plane. Because we are interested in membrane-bound Aβ, which lies within 10 nm above the cover glass (Figure 2-2), the utilization of TIRF dramatically improves the signal-to-noise ratio and, consequently, the spatial resolution of the features or events of interest. Moreover, TIRF can be used to collect wide-field and real-time images; thus, multiple photobleaching events and particle diffusion motions can be collected.

For total internal reflection, the laser beam is shifted toward the side of the objective, which increases the incident angle (Figure 2-2). Total internal reflection is generated when the incident laser beam enters just beyond the critical angle from a higher refractive index material (*e.g.*, cover glass, n_1 ~ 1.51) to a lower refractive index sample (*e.g.*, buffer or model membrane, n_2 ~ 1.3-1.4). A static electromagnetic wave (*i.e.*, an evanescent wave) is generated on the sample side, and the energy exponentially decreases as follows:

$$I(z) = I(0) \cdot e^{-z/d}. \text{ Eq, 2-1}$$

The penetration depth constant (d) is dependent upon the wavelength of the incident illumination (λ), the angle of incidence (θ), and the refractive indices of the media at the interface, according to the following equation (137)**:**

$$d = \frac{\lambda}{2\pi}(n_1^2 \cdot sin^2\theta - n_2^2)^{-1/2}, \text{ Eq. 2-2}$$

where d is typically less than 300 nm; therefore, highly specific fluorescence excitation can be induced in a very thin optical section. Although TIRF is limited to imaging at the interface of two different media with suitable refractive indices, numerous applications are ideally suited for this technique. The biomedical field represents one of the most active research areas, in which numerous compelling questions involve processes at the cell surface or plasma membrane, which are appropriate interfaces for TIRF investigations.

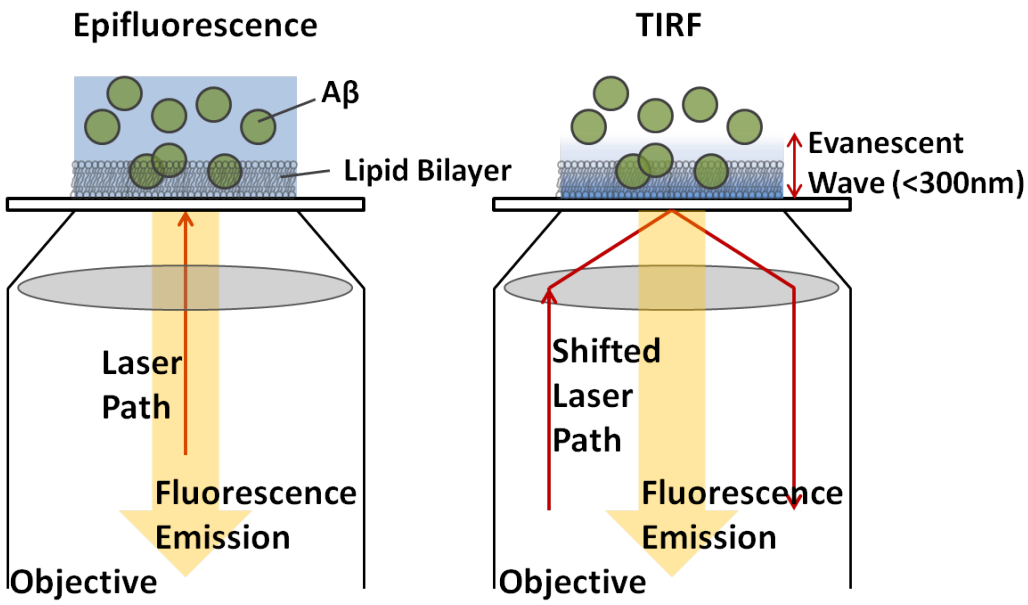

Figure 2-2. Comparison between epifluorescence and TIRF microscopies.

2-3-1 TIRF Data Acquisition

Single molecule TIRF microscopy was performed on an Olympus (Center Valley, PA) IX-71 inverted microscope. A single-mode diode laser (643 nm, Power Technology, Inc., Alexander, AR) was focused onto the back focal plane of a 60x, 1.45 NA Olympus PlanAPO TIRF objective. Through-the-objective TIRF was performed by translation of a mirror just upstream of the objective lens. A multi-band pass SEMRock (Rochester, NY) dichroic mirror was used to separate excitation from emission signal; a 620/60 excitation band pass filter (Chroma Technology Corporation, Bellows Falls, VT) and 700/75 emission filter (Chroma Technology Corporation) were included in the setup. Images were acquired on a back-illuminated Ixon EMCCD camera, model DV887ACS-BV (Andor, Belfast, UK).

2-3-2 Fluorescence Recovery after Photobleaching (FRAP)

To confirm whether the lipid bilayer was successfully formed, a FRAP experiment was performed to measure the mobility of the lipid molecules (138, 139). To

monitor the lipid molecules, 0.5% nitro-2-1,3-benzoxadiazol-4-yl-POPC (NBD-POPC; Avanti Polar Lipids) was mixed with 79.5% POPC and 20% POPG to enable fluorescence photobleaching and monitor the recovery. An argon laser was used for conventional epifluorescence or TIRF microscopy to photobleach a circular membrane area approximately 50 μm in diameter with high-intensity laser illumination for a short duration (5 seconds). Because the laser intensity is higher than the saturation level of the dye molecules, the uneven illumination continues to yield a relatively flat photobleaching profile, which satisfies the assumption used in the following analysis to extract the diffusion coefficient. The fluorescence recovery in the photobleached region was subsequently recorded using a much lower illumination intensity (<1/2500 of the photobleaching intensity). Because all of the free lipid molecules in solution were removed through extensive washing, the fluorescence recovery was purely due to the lateral diffusion of the lipid molecules in the membrane; this mobility measurement of the lipid molecules was also used to confirm the integrity of the lipid membrane. To extract diffusion coefficients from FRAP analysis, the fluorescence recovery curves were fit to the following equation (139) using Mathematica:

$$f(x) = e^{-\frac{2\tau_D}{t}} \cdot [\, I_0(\frac{2\tau_D}{t}) + I_1(\frac{2\tau_D}{t})]. \text{ Eq. 2-3}$$

In this equation, $f(x)$ is the integrated fluorescence intensity over the photobleached region; I_0 and I_1 are the modified Bessel functions of the first kind, as follows:

$$(I_n(z) = \frac{1}{2}\, \pi i \oint e^{\frac{z}{2}(t+\frac{1}{t})} \cdot t^{-n-1}\, dt). \text{ Eq. 2-4}$$

where τ_D=$\frac{w^2}{4D}$ is the characteristic diffusion time, w is the radius of the photobleached region, and D is the diffusion coefficient. As shown in Figure 2-3, after 150 hours of incubation of unlabeled Aβ40 with 0.5% NBD-POPC labeled lipids, lipid molecules continued to uniformly diffuse with the diffusion coefficient D = 1.49 ± 0.23 μm^2/sec, which indicates that the lipid bilayer was successfully formed without disruption by Aβ.

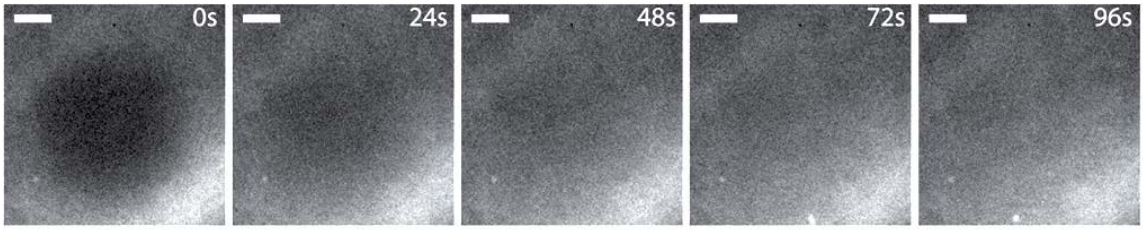

Figure 2-3. Lipid bilayer remains uniform and diffusible after incubating with Aβ for 150 hours. Lipid bilayer with 0.5% labeled POPC-NBD was incubated with for 2nM unlabeled Aβ40 150 hours. Fluorescence recovery after photobleaching (FRAP) shows the lipids are still mobile even immobilized oligomers have been formed as shown in Figure xx. This may suggest the Aβ immobilization and aggregation is not caused by lipid disruption. Scale bar is 10 μm.

2-3-3 Single Particle Tracking and Lateral Diffusion Analysis

Sample contains both immobile and mobile particles on the lipid bilayer; therefore to first monitor the mobile species, we removed most of the immobile particles by subtracting each frame with averaged consecutive ten frames. Each image file contains 150 frames with the accusation time of 0.3 second. Fluorescently labeled Aβ oligomers in each frame of a recording were localized using custom software written in Matlab (The MathWorks, Natick, MA) as described previously (140). Briefly, diffraction-limited spots were fit to a two-dimensional Gaussian shape through least squares fitting using 'fminfunc()', a built-in Matlab function. Identified spots are culled to remove outliers in width, brightness, aspect ratio, and localization precision. Particle tracking were performed using a global minimization algorithm as described in Jaqaman *et al*. (141). Trajectories included had at least 10 displacements. The mean square displacement (MSD) was calculated using the following formula:

$$\mathrm{MSD(ndt)} = \frac{1}{\mathrm{N-n}} \sum_{i=1}^{\mathrm{N-n}} [(\mathrm{x_{(i+n)}} - \mathrm{x_i})^2 + (\mathrm{y_{(i+n)}} - \mathrm{y_i})^2], \text{ Eq. 2-5}$$

where x_i and y_i are the coordinates of an object on frame i, N is the total number of frames of the trajectory, n is the number of interval, dt is the time between two successive

frame, and ndt is the time interval over which the displacement is averaged. The initial diffusion coefficient (D) was determined by fitting the first 2-5 points of the MSD plot versus time with $\mathrm{MSD(t)} = 4\mathrm{D}_{2-5}\mathrm{t}$ (101, 142).

2-3-4 Oligomer-Size Calibration using Photobleaching or Fluorescence Intensity

The combination of TIRF microscopy with single-molecule photobleaching allows the simultaneous monitoring of the fluorescence intensity from multiple single aggregates over a broad area in real time. Each monomeric molecule of interest is labeled with a fluorescent dye (in our case, each Aβ peptide is labeled with one dye molecule) (143); therefore, using a strong laser intensity to photodamage the dye molecules causes a stepwise decrease in the fluorescence intensity. The number of monomeric molecules that form an aggregate can be determined by counting the photobleaching steps from a particular aggregate (143, 144).

The two major difficulties in counting the photobleaching trajectory are due to the following reasons: 1) the aggregate fluorescence signal contains more than seven monomers, which may saturate the CCD camera and produce unresolved initial bleaching steps and 2) the labeled protein fluctuating in the sample may produce a noisy fluorescence trajectory. In our case, a portion of each immobilized oligomer (*i.e.*, the N-terminus, which is labeled with the dye) may continue to freely fluctuate in the membrane, which produces a fluorescence time trace that is too noisy to be resolved.

Rather than directly counting the oligomer size from the photobleaching trajectories, the first frame of the integrated fluorescence intensity was divided by the average monomer intensity to yield the total number of monomeric peptides in a particular oligomer. To obtain the average monomer intensity, we selected at least 30 photobleaching trajectories with two well-resolved bleaching steps (dimer) and equal step sizes. After background subtraction, the initial intensities were divided by two to yield the estimated monomer intensity (Figure 2-4). A single bleaching step is excluded because it may result from two or three dye molecules that bleach faster than the data acquisition time. Therefore, the single bleaching step may not truly represent the

monomer intensity. When the average monomer intensity was determined, the oligomer fluorescence intensity was divided by this value and rounded to the nearest integer to yield the corresponding size. The fluorescence intensity of the selected oligomers was corrected based on their position relative to the center of illumination.

These steps were processed using an in-house LabVIEW program. First, the oligomers were identified by dividing the intensity of each pixel by the average intensity from 80 surrounding pixels (9 × 9 pixels; this box can be adjusted based on the oligomer density). Potential oligomers were selected if their divided intensity was greater than the threshold (1 equals the background) and smaller than the assigned oligomer size (*i.e.*, the pixel number of each oligomer). The background composed of the 80 surrounding pixels was later subtracted. The oligomer intensities were corrected by multiplying an intensity ratio factor based on the oligomer location relative to the center of illumination; this ratio factor was calculated by using a control image of only the lipid bilayer and measuring the ratio of the intensity at the oligomer position to the intensity at the center of the image. This final value represents the oligomer intensity, and its time trace was plotted to search for a clear dimer trajectory (Figure 2-4).

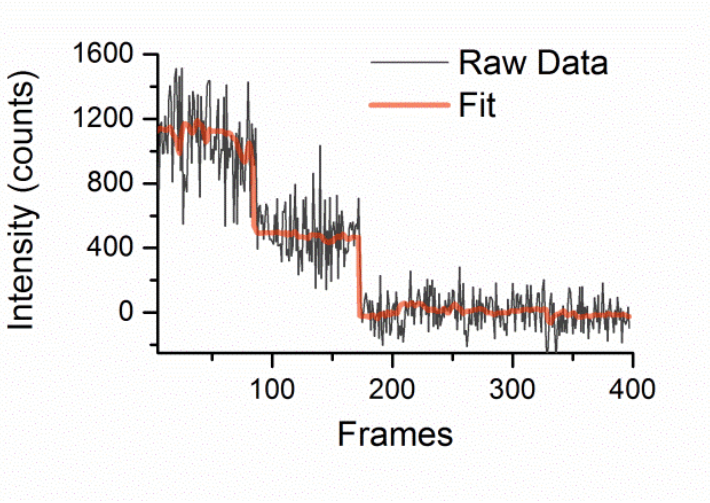

Figure 2-4. Two photobleaching steps indicate that the oligomer is a dimer. The average monomer intensity is approximately 550 counts.

2-4 Confocal Microscopy

If the target molecule is more than 300 nm above the glass surface (*i.e.*, a protein located on top of a cell membrane), TIRF microscopy is inadequate. Confocal microscopy allows for deeper sample measurement and removes the out-of-focus background signal using point illumination and a spatial pinhole to eliminate the out-of-focus light in specimens that are thicker than the focal plane. Additionally, confocal microscopy enables the reconstruction of three-dimensional structures from the obtained images.

In a conventional fluorescence microscope, the entire specimen is evenly flooded with light from a light source (Figure 2-2, left). All areas in the specimen that lie in the optical path are simultaneously excited, and the resultant fluorescence is detected by the microscope photodetector or camera, which includes a large portion of unfocused background. In contrast, a confocal microscope uses point illumination and a "detector pinhole aperture" in an optically conjugate plane in front of the detector to eliminate out-of-focus signals; the name "confocal" stems from this configuration (Figure 2-5). Because only the light produced by fluorescence near the focal plane can be detected, the optical resolution of this image, particularly in the sample depth direction, is superior to the resolution generated using wide-field microscopes. However, because much of the light from the sample fluorescence is obstructed at the pinhole, the enhanced resolution yields lower signal intensity; therefore, long exposures are often required. Because only one point in the sample is illuminated at a time, 2D or 3D imaging requires scanning over a regular raster (*i.e.*, a rectangular pattern of parallel scanning lines) in the specimen. The achievable thickness of the focal plane is primarily defined by the wavelength of the light used divided by the numerical aperture of the objective lens but also by the optical properties of the specimen. These microscopes are particularly suitable for 3D imaging and sample surface profiling due to thin optical sectioning.

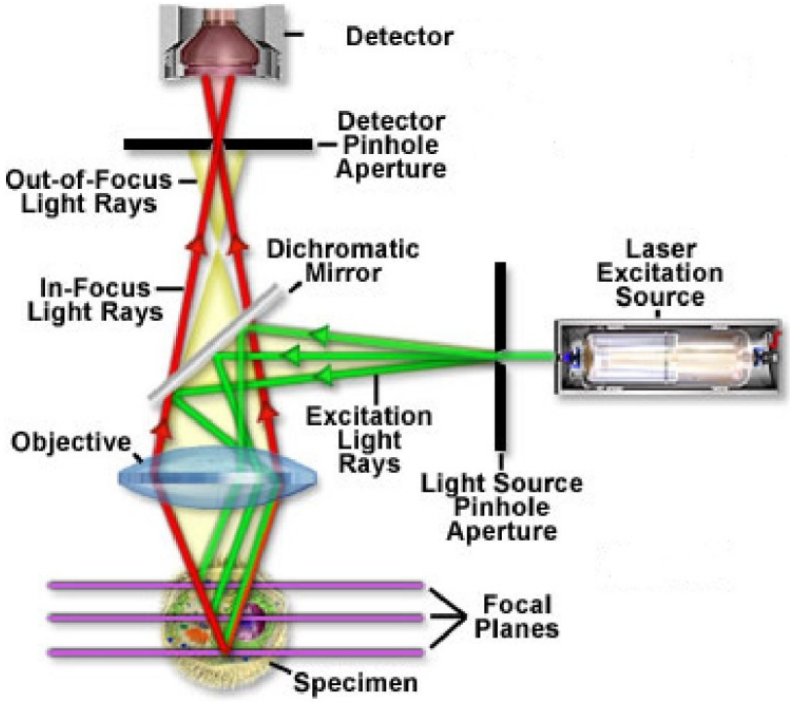

Figure 2-5. Basic setup for confocal microscopy. An aperture (pinhole) is used to block out-of-focus flare in thick sample, leaving only the focal spot got through. Image is adapted from http://www.microscopyu.com

2-4-1 Fluorescence Lifetime Imaging Microscopy (FLIM)

In vivo fluorescence emission detection at the single-molecule level represents a challenge for confocal microscopy because cellular autofluorescence competes with exogenous dye emission (145, 146). Thus, two different fluorophores or different signal sources with overlapping emission spectra cannot be distinguished. Therefore, additional information is necessary to separate multiple signals that exhibit similar fluorescence emission spectra.

Information is collected by the detector, which measures the number of photons (*i.e.*, the intensity). Through manipulation, the detector can also measure how rapidly fluorescence emission is detected upon laser excitation. This additional information represents the "fluorescence lifetime," which depends on the chemical structure and local environment. For example, ATTO-565 and Cy3 exhibit similar emission maxima at

approximately 560 nm; however, ATTO-565 exhibits a lifetime of 3.4 ns, which is much longer than that of Cy3 (0.3 ns). Therefore, by measuring their fluorescence lifetimes, ATTO-565 and Cy3 can be simultaneously detected without ambiguity. FLIM has also been used to discriminate between autofluorescence and sample fluorescence (147–149).

FLIM uses an avalanche photodiode (APD) detector with confocal microscopy and time-correlated single photon counting (TCSPC). In TCSPC, one measures the time between sample excitation using a pulsed laser and the arrival of the emitted photon at the detector. TCSPC requires a defined "start", which is provided by electronics that steer the laser pulse or photodiode, and a defined "stop" signal, which is generated through detection using single-photon sensitive detectors (*e.g.*, APD). This time delay is repeatedly measured to statistically analyze the fluorophore emission. The delay times are sorted into a histogram that plots the occurrence of emission as a function of time following the excitation pulse (Figure 2-6, measured). To acquire a fluorescence lifetime image, the photons must be attributed to different pixels by storing the absolute arrival times of the photons in addition to their relative arrival time with respect to the laser pulse. As shown in Figure 2-6, the lifetime value per pixel is determined by fitting the measured data with the convolution of the instrument response function and a single exponential decay (assuming the fluorescence only includes a single lifetime).

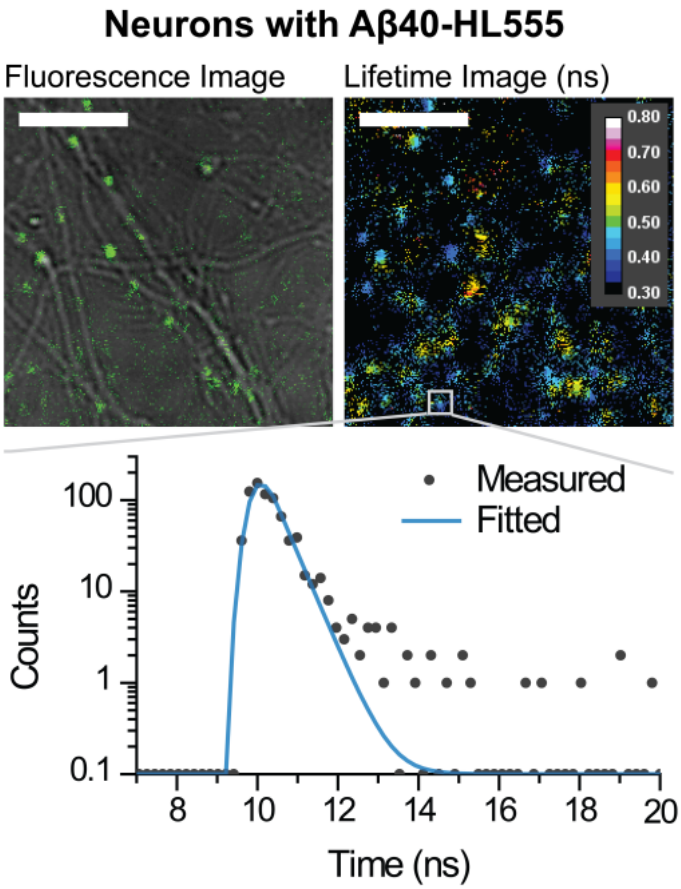

Figure 2-6. Fluorescence lifetime imaging microscopy and lifetime fitting. Upper left is the fluorescence signal from Aβ40-HL555. Upper right shows the lifetime value (nano seconds) in each pixel. The lifetime value is fitted by a single exponential decay as shown in the bottom.

2-4-2 FLIM Data Analysis

While excitation in the red (HL647 or Cy5 dye) results in almost no autofluorescence, an auto-fluorescent signal is generated in the cell when it is excited with a 532 nm laser, which is a common wavelength for the FRET donor. This makes Aβ40-HL555's emission indistinguishable from the autofluorescence based on the gross emission spectrum (Figure 2-7 upper left). However, incorporating single molecule fluorescence lifetime imaging microscopy (smFLIM) gives us another dimension to differentiate signals with similar fluorescence intensity. We performed smFLIM

measurement on two samples, neurons with 2nM unlabeled Aβ40 and neurons with 2nM Aβ40-HL555 (Figure 2-7). The fluorescent spots of these two samples were selected and each spot's lifetime was fitted to a single exponential decay. For the sample with Aβ40-HL555 we only selected those spots that were away from the cell body that possesses strong autofluorescence. The distribution of the lifetime from the selected spots is plotted in Figure 2-7 right. The lifetime distribution of the control sample peaks around 0.58 ns, whereas the lifetime of membrane bound Aβ40-HL555 peaks around 0.48 ns with 6 fold larger density of emitters than the autofluorescence at this lifetime. Based on this distinct difference, fluorescent spots with lifetime greater than 0.53 ns were considered autofluorescence and excluded from our measurement. While this approach may mark a small number of autofluorescent spots as Aβ40, comparison of the results between two different time points minimizes this bias since the autofluorescence remains similar over time.

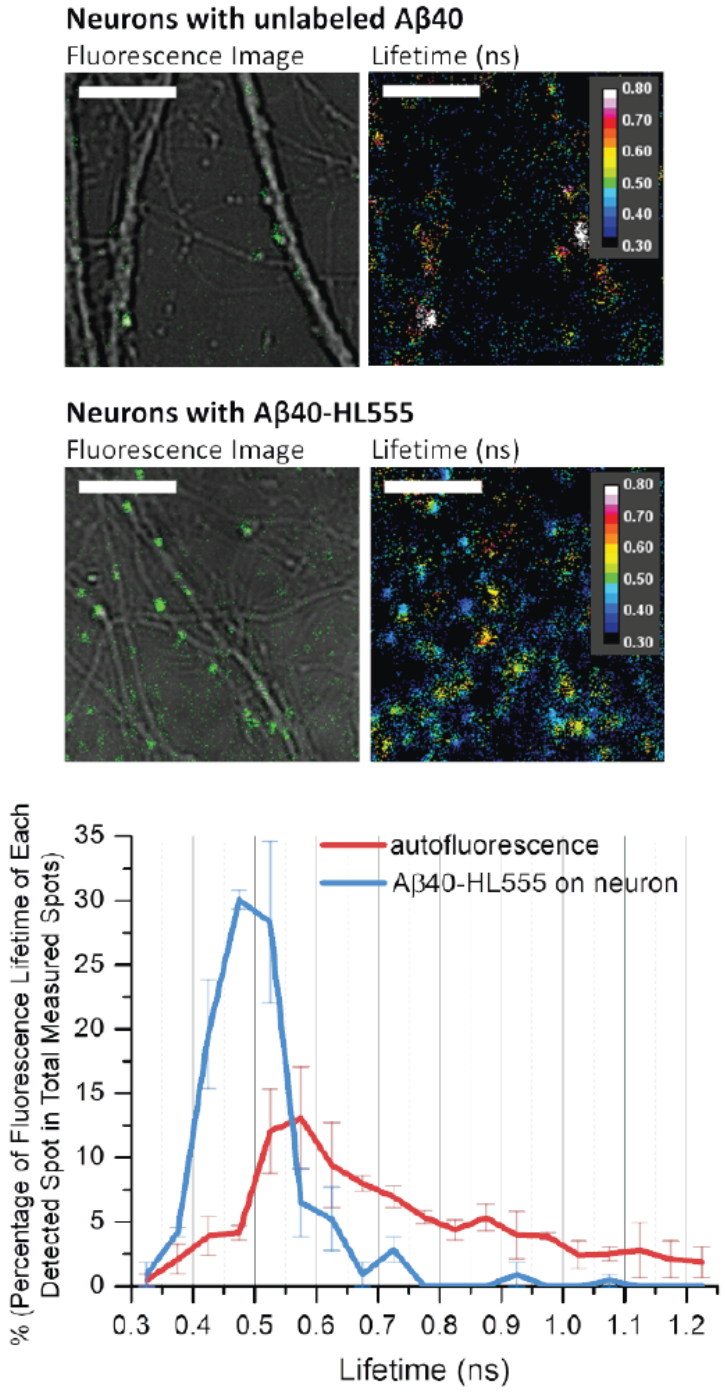

Figure 2-7. Sample with Aβ40-HL555 shows shorter fluorescence lifetime spots than the control sample. The data presented for each sample is the average of two experiments and each experiment contained at least 250 particles. Error bars represent the standard deviation of the mean.

2-4-3 Lifetime Acquisition Parameters

Fluorescence lifetime imaging microscopy (FLIM) was performed at the University of Michigan's Single Molecule Analysis in Real-Time (SMART) Center and was measured by time-correlated single-photon counting (TCSPC) by ALBA microscope system (ISS, Champaign, IL). The microscope was Olympus IX-81, equipped with a 37°C temperature controlling stage, a 1.2NA 60X water-immersion objective (Olympus) and imaged by two APDs. The excitation source was Fianium SC 400-6-PP with acousto-optic tunable filters (AOTF). Laser excitation was selected at 532nm and 635nm with power 41.5 μW and 34.6 μW before the objective respectively. The emission filter for Aβ40-HL555 and Aβ42-HL647 were 582/75 and 697/75 nm band pass filter (Semrock) respectively. The dichroic mirror was 405/470/532/632 quadband dichroic mirror (Alluxa, Santa Rosa, CA). The lifetime is fitted by VistaVision software (ISS, Champaign, IL) with one exponential decay curve.

2-5 Förster Resonance Energy Transfer (FRET)

FRET measures the distance between two molecules that lie within several nanometers of each other, which is a sufficient distance for molecular interactions, whereas two-color colocalization can only resolve a distance on the scale of hundreds of nanometers (which is more than 20 times less sensitive than FRET).

The mechanism of fluorescence resonance energy transfer involves a donor fluorophore in an excited electronic state, which may transfer its excitation energy to a nearby acceptor fluorophore in a nonradiative fashion through long-range dipole-dipole interactions. Upon detection of acceptor emission following donor excitation, the energy transfer efficiency and donor-acceptor distance can be calculated. The theory underlying energy transfer is based on the concept of treating an excited fluorophore as an oscillating dipole that can undergo energy exchange with a second dipole of a similar resonance frequency. In this regard, resonance energy transfer is analogous to the behavior of coupled oscillators, such as a pair of tuning forks vibrating at an identical frequency. In contrast, radiative energy transfer requires the emission and reabsorption of a photon and

depends on the physical dimensions and optical properties of the specimen, the container geometry, and the wavefront pathways. Unlike radiative mechanisms, resonance energy transfer can yield a significant amount of structural information on the donor-acceptor pair.

2-5-1 FRET Efficiency Analysis

The size of individual Aβ oligomers is quantified based on their relative fluorescence intensity to the monomer intensity. For the homogeneous Aβ40 and Aβ42 as well as for Aβ42 in the heterogeneous species this is straightforward because their emission intensities are not significantly modified by quenching. In contrast, when Aβ40 bound to Aβ42, energy transfer occurs and Aβ40 emission is partially quenched. The original intensity of a donor is calculated by

$$I^{0}_{A\beta 40} = \frac{I_{A\beta 40}}{(1-E)} \quad \text{Eq. 2-6}$$

where $I_{\mathrm{A\beta 40}}$ is the measured Aβ40 emission intensity excited at 532 nm. $\mathrm{I}^{0}_{\mathrm{A\beta 40}}$ is the calculated original donor emission before quenching. And E is the FRET efficiency

$$E = \frac{I_{A\beta 42}}{I_{A\beta 42} + \gamma \times I_{A\beta 40}} \quad \text{Eq. 2-7}$$

$$\gamma = \frac{Acceptor's\ Quantum\ Yield\ \times Acceptor\ Channel's\ Detection\ Efficiency}{Donor's\ Quantum\ Yield\ \times Donor's\ Channel's\ Detection\ Efficiency}$$

where $I_{\mathrm{A\beta 42}}$ is the measured Aβ42 emission intensity excited at 532 nm. And γ is the quantum yield of Aβ42 divided by the quantum yield of Aβ40, which has been corrected for its lifetime, and then multiply the detection sensitivity of the acceptor divided by the detection sensitivity of the donor (150).

The degree of bleed through from the donor emission into acceptor channel is calculated by a linear fit to Aβ40 emission appeared in acceptor channel versus different

Aβ40 concentrations in solution containing only the Aβ40. The measured FRET signal is therefore corrected for the bleed through from its donor (Aβ40). The direct excitation of the acceptor at 532 nm was found to be insignificant.

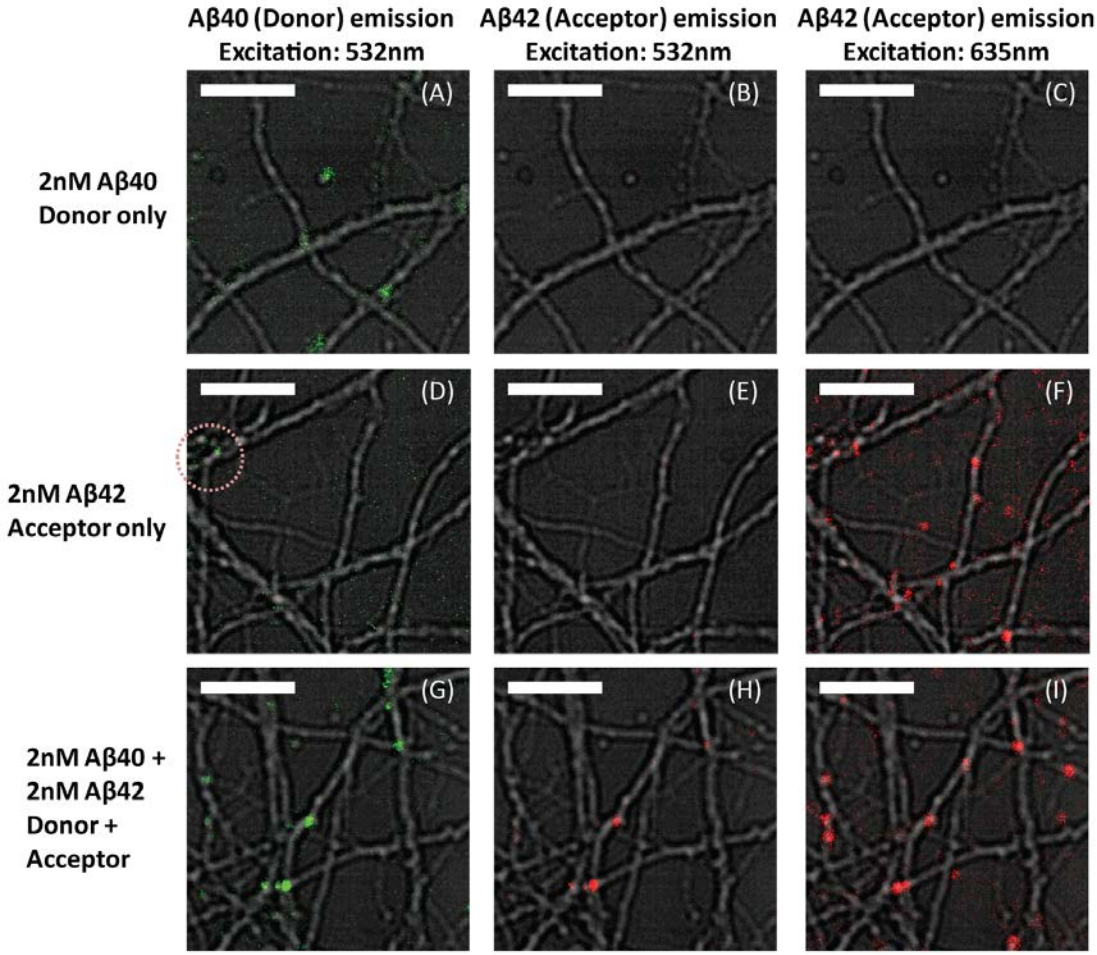

Figure 2-8. FRET is only detected when Aβ40 is mixed with Aβ42. Scale bars are 10 μm. Primary hippocampal neurons incubated with 2nM Aβ40 were excited by 532 nm laser and show Aβ40 (donor) emission (A) but do not show any emission in Aβ42 (acceptor) channel (B), and Aβ40 can not be directly excited by 635 nm (C). Neurons incubated with 2nM Aβ42 only were also excited by 532 nm laser but do not show any signal in Aβ40 (donor) and Aβ42 (acceptor) emission channels (D and E). The sample with just Aβ42 can only be excited by 635 nm laser and shows emission in Aβ42 (acceptor) emission (F). Neurons incubated with 2nM Aβ40 and 2nM Aβ42 were excited by 532 nm laser and show both donor emission (G) and FRET signal (H). Excitation of 635 nm laser confirmed Aβ42 emission co-localizes with acceptor signals (I). The dashed

circle shown in (D) indicates the autofluorescence generated by 532 nm laser, and the donor emission is later distinguished from autofluorescence by their fluorescence lifetime.

2-5-2 Donor Acceptor distance Analysis from FRET

The distance between a donor and acceptor is the most powerful information that can be extracted from single-molecule FRET. The FRET efficiency (E_T) of dipole-dipole interactions can be described as follows:

$$E_T = \frac{{R_0}^6}{r^6 + {R_0}^6}, \text{ Eq. 2-8}$$

where r is the distance between the donor and acceptor. R_0 is the Förster critical distance; when $r = R_0$, the transfer efficiency is 50%.

$$R_0 = 2.11 \times 10^{-2} \bullet [\kappa^2 \bullet J(\lambda) \bullet \eta^{-4} \bullet Q_D]^{1/6}, \text{ Eq. 2-9}$$

where κ^2 is a factor that describes the relative orientation in space between the transition dipoles of the donor and acceptor, $J(\lambda)$ is the overlap integral in the donor emission and acceptor absorbance spectral region (the wavelength is expressed in nanometers), η represents the refractive index of the medium, and Q_D is the quantum yield of the donor. Ideally, the FRET efficiency can be used to calculate the distance between the donor and acceptor and provide structural information on the complex; because the dyes may be randomly oriented in solution, κ^2 is typically assumed to be 2/3. Therefore, R_0 for a Cy3-Cy5 FRET pair is 47 Å (which is corrected for the Q_D on the neurites). Based on Eq. 2-7, the calculated Aβ40-Aβ42 dimer distance distribution is shown in Figure 2-9.

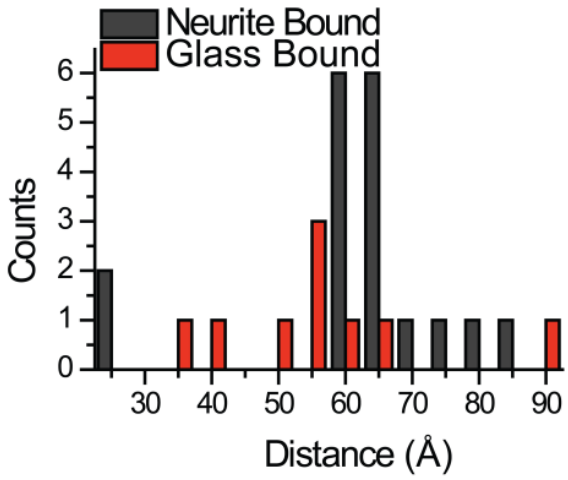

Figure 2-9. Distance of a hetero-dimer (N-terminus to N-terminus) on neurite and the glass surface.

We note that in using the FRET efficiency we estimate the distance between two N-terminus of a dimer is ~60 Å. This is larger than would be expected for a globular association of the peptides forming the oligomer (25 Å) (151). There are at least three possibilities that might account for this. The first is that the assembly is not globular but stretched out, perhaps because it is on a surface, though this seems unlikely. The second is that the calculation for the FRET distance assumes that the dipole orientation between the donor and the acceptor is fully randomized (i.e., $k^2 = 2/3$). If assembly on the lipid bilayer results in steric hindrance, then k^2 could be much smaller resulting in lower transfer efficiency and an increased inferred separation between donor and acceptor. A third possibility is that these oligomers are not structures of pure Aβ peptides, but rather structures that assemble on the membrane surface either by association with some structural scaffold (e.g., a membrane bound protein complex or something associated with the cytoskeletal structure) or by including lipids in the structure leading to a larger assembly. Resolving these models by optical imaging clearly lies outside the bound of even the highest super resolution methods.

2-5-3 Confocal Mode Integrated Intensity-based Oligomer Size Determination

We have used confocal mode fluorescence intensity to measure oligomer size on both black lipid membranes and cell membranes (152–154). To measure oligomer size on living cells, a protocol has been developed to correlate particles' confocal mode fluorescence intensity values with the number of Aβ monomers they contain (153). When the laser power is below saturation, the total fluorophore emission varies linearly with Aβ concentrations in solution. Therefore, the slope of total intensity from a given volume versus the number of molecules present in the volume yields intensity per molecule. The fluorescence intensity of an oligomer can be divided by this value to yield the number of Aβ monomers present in the oligomer. The cell-bound oligomers were defined as those fluorescence spots whose maxima fell on or within 500 nm of a neurite and were boxed with a 12 pixel x 12 pixel (~1.5 μm x 1.5 μm) region of interest (Figure 2-10 solid square). Following subtraction of adjacent background fluorescence counts (Figure 2-10 dashed square), the integrated fluorescence intensity of each region of interest was divided by fluorescence intensity per molecule to determine oligomer size. However, the fluorescence intensity is partially quenched upon binding to the neuronal membrane. For dynamic quenching, the ratio of intensity of the quenched fluorophore (I_q) to that of the unquenched fluorophore (I_0) is equal to the ratio of the fluorophore lifetimes (τ_q and τ_0, respectively) under each condition (155):

$$\frac{I_q}{I_0} = \frac{\tau_q}{\tau_0}$$, Eq. 2-10

The averaged fluorescence lifetimes for Aβ40 and Aβ42 in 10 mM sodium phosphate buffer (τ_0) were 0.75 and 1.56 ns. And the averaged lifetimes of membrane bound Aβ40 and Aβ42 were 0.48 and 1.24 ns.

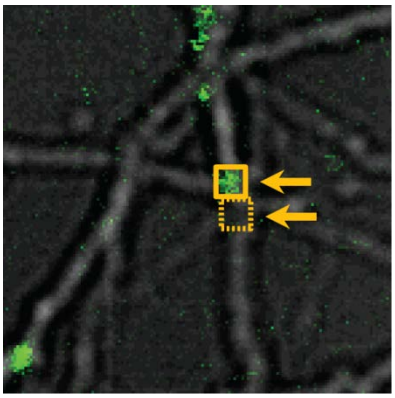

Figure 2-10. Aβ oligomer size is determined by its fluorescence intensity.

2-6 Peptide Preparation

N-terminally HiLyteFluor 555 labeled Aβ40, and N-terminally HiLyteFluor 647 labeled Aβ40 and Aβ42 (Aβ40-HL555, Aβ40-HL647 and Aβ42-HL647, respectively) were obtained from Anaspec (Freemont, CA). Aβ peptides were dissolved in 1% NH_4OH at 0.1 mg/mL and vortexed for 30 s. The peptide solutions were aliquoted into individual microtubes, lyophilized and the solids stored at -20°C. To prepare fresh Aβ samples, single aliquots were dissolved in 10 mM sodium phosphate buffer, pH 7.4, to a concentration of 1-2 μM (as determined spectrophotometrically using ε_{555}=150,000 and ε_{647}=250,000). Freshly prepared Aβ were further diluted down to final concentrations within 15 minutes.

Numerous control experiments have been done in our laboratory and others suggest that various forms of N-terminally labeled Aβ behave similarly to unlabeled Aβ in terms of fibrilization (156), ability to permeabilize synthetic membranes (143, 152) as well as rat basophilic leukemia cell-derived membrane blebs (153), toxicity to cultured cells (157) and microglial activities inside the mouse cortex (158).

2-7 Primary Rat Hippocampal Cell Culture

Dissociated neuron cultures were made from newborn pups (P0−P2). Rats were euthanized by decapitation immediately prior to brain dissection and tissue collection.

This procedure was carried out in strict accordance with the recommendations in the Guide for the Care and Use of Laboratory Animals of the National Institutes of Health. The protocol was approved by the University Committee on Use and Care of Animals (UCUCA) at the University of Michigan. Primary rat hippocampal neuron cultures were prepared as described (159). Cells were plated at 30,000/well on 14 mm poly-D-lysine coated glass coverslips adhered to 35 mm culture dishes (MatTek, Ashland, MA). Imaging experiments were performed between DIV 12 and DIV 18. For single molecule oligomer size measurement experiments, cells were incubated for 10 minutes or 48 hours at 37°C in HBS (HEPES-Buffered Saline: 119 mM NaCl, 5 mM KCl, 2 mM $CaCl_2$, 2 mM $MgCl_2$, 30 mM Glucose, 10 mM HEPES, pH 7.4) containing 2 nM Aβ40-HL555 or Aβ42-HL647 or 4 nM mixed Aβ40-HL555 and Aβ42-HL647 at 1:1 ratio. Before imaging, cells were washed three times in HBS and then imaged within two hours.

CHAPTER 3

STUDIES OF Aβ40 AND Aβ42 INTERACTIONS ON A PLANAR LIPID BILAYER

3-1 Motivation for Model Membrane Studies

Model membranes differ substantially from biological membranes and clearly lack important additional components such as different leaflet compositions, connections to the cytoskeleton, integral membrane proteins and polysaccharides, that may all significantly alter the behavior of Aβ and its corresponding toxicity. Hence, model membranes serve the purpose of understanding the interaction with the phospholipid bilayer, where we recognize even in this that the cellular phospholipid bilayer can be more diverse than what we use here. Model membranes, however, make it possible to study the specific effects of proteins on lipid membrane components in a systematic, controlled manner. Although the complex array of biochemical processes that influence protein activity cannot be fully represented using model membrane systems alone, these membrane systems provide a platform to investigate select protein–membrane interactions and key mechanistic events that underlie biological activity.

Single-molecule microscopy is well suited for studies at physiological peptide concentrations and allows direct monitoring of oligomer formation at the cellular membrane from monomeric Aβ. Recently, our group (152–154, 160, 161) and others (162, 163) have employed single-molecule microscopy in total internal reflection fluorescence (TIRF) and confocal modes to study Aβ oligomer assembly and size distribution at physiological peptide concentrations at the surface of model membranes and at the surfaces of PC12, SH-SY5Y neuroblastoma and cultured neuronal cells. Even at these low concentrations, Aβ tightly associates with the membrane (K_d < 470 pM)

(160), and the membrane facilitates the formation of surface-bound oligomers that exhibit a clearly larger size distribution in comparison to oligomers formed in solution. Using single-molecule microscopy in combination with electrophysiological measurements, we also found that the Aβ40 oligomer size correlates with conductance changes in a model membrane (152).

In this study, total internal reflection microscopy was used to image individual fluorescently labeled synthesized Aβ peptides at physiological concentrations interacting with a supported lipid bilayer combined and to monitor the oligomerization process on the membrane. The membrane's 2D surface, with a wide illumination area, provides an excellent platform for single-particle tracking, thereby enabling us to monitor the movement of individual membrane-bound mobile species and characterize their size (*i.e.*, the number of peptides) based on their fluorescence intensity (*i.e.*, the accumulated intensity). Utilizing fluorescence photobleaching from a fraction of membrane-bound immobile species, the monomer intensity can be readily acquired and further used to calibrate the size of the entire membrane-bound Aβ population. The comparison of the dynamics and size between the mobile and immobile species as well as among Aβ40, Aβ42, and the Aβ40:Aβ42 mixture provides information that further explains several experimental observations over recent decades in more detail.

3-2 Aβ40, Aβ42, and the Aβ40:Aβ42 mixture primarily exist as monomers in solution at nanomolar concentrations and do not exhibit additional oligomerization over 120 hours

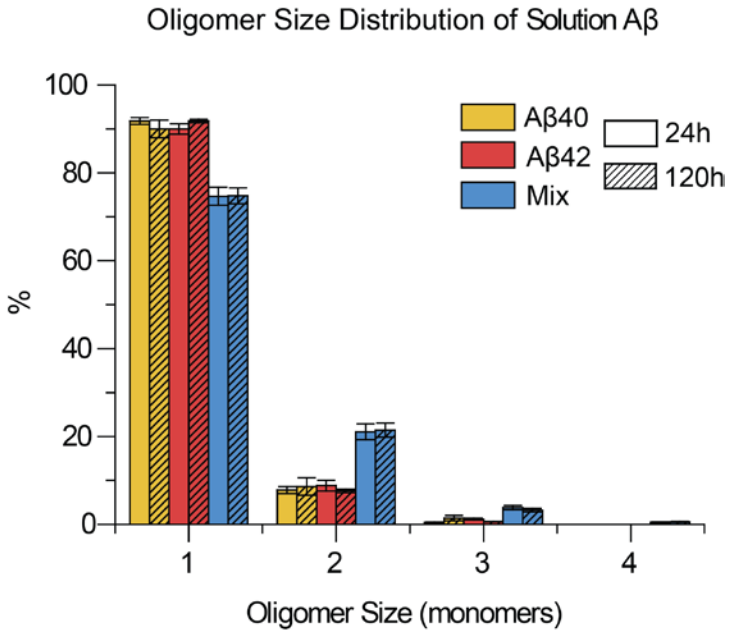

Figure 3-1. Oligomer size distributions for 4 nM Aβ40, Aβ42, and a 1:1 mixture of Aβ40:Aβ42 in solution. The oligomer sizes were determined by counting the photobleaching steps and were corrected for the threshold effect due to fluorophore dipole orientation. The percentage was obtained by normalization to the total number of oligomers. The percentages in each condition were calculated from at least three experiments, and each experiment contained at least 200 oligomers. The error bars represent the standard deviation of the mean.

To compare the size (*i.e.*, the number of monomeric peptides in an oligomer) of the membrane-bound Aβ to Aβ in solution, we first extracted a 10-μL aliquot from peptide solutions that were incubated with a lipid bilayer for 24 and 120 hours and spin-coated each aliquot on a precleaned glass slide at 2000 rpm until the cover glass was dry (~30–40 seconds at room temperature). We did not observe a loss of solution from the slide during this process, assuring that 100% of the Aβ was captured. Because the spin-coated oligomers were dry and exhibited clear photobleaching trajectories, their sizes

were determined by counting the number of photobleaching steps. Due to the different dipole orientations assumed by the fluorophore in this experiment, the emission intensity of some of the oligomers was below the threshold used in our data processing (to reject background fluorescence), leading to undercounting. We corrected this bias for all of our spin-coated sample, as previously described (143). We also assumed that the spin-coating process was sufficiently rapid that the oligomer size distribution was not altered during solvent evaporation.

Both Aβ40 and Aβ42 samples were found to possess similar size distributions of 91.8% and 90.0% monomer, respectively, after a 24-hour incubation (Figure 3-1). These results are consistent with previous studies that indicated the monomer is the dominant species in solution at nanomolar concentrations (153, 154, 164). However, the solution that contained 1:1 Aβ40:Aβ42 exhibited slightly fewer monomers (74.7%) and more dimers, suggesting that Aβ40 and Aβ42 interact to form slightly larger oligomers in solution then either peptide alone (Figure 3-1). This observation is also consistent with previous reports (154).

Although the Aβ40:Aβ42 mixture contains a slightly larger dimer fraction, the monomer remains the dominant species, and the oligomer size distribution does not change over a 120-hour incubation in all cases (i.e., Aβ40, Aβ42, or the Aβ40:Aβ42 mixture), showing that Aβ does not oligomerize in solution at nanomolar concentrations.

3-3 Membrane-bound Aβ monomers and some dimers are mobile and tightly associate with the membrane

We have previously shown that Aβ preferentially interacts with anionic lipid head groups (37) and that the density of bound monomeric peptide is dependent on the fraction of the negatively charged group (POPG) in the membrane. Thus, for the 4:1 POPC:POPG ratio used here, we found that the density of bound Aβ was approximately 3 peptides/μm^2 (calculated by subtracting the peptide density of immobilized species from the total density of membrane bound peptides shown in Figure 3-7), whereas for a 7:3 DiphPC:DiphPG ratio, the density was approximately 5 peptides/μm^2 (152), and a 1:1

POPC:POPG ratio yielded a density of approximately 8 peptides/μm^2 (160). Although the membrane saturation level for the monomeric peptide increased somewhat with the negatively charged lipid density, it is striking that, in all three cases, the binding became saturated at a very low peptide-to-lipid ratio (see Chapter 5).

After 24-hour incubation of Aβ solutions with the lipid bilayer, mobile and immobile oligomers were observed on the membrane (Figure 3-2A). The mobile species maintained a similar density (3 peptides/μm^2) even after a 120-hour incubation with plain buffer (*i.e.*, no Aβ in solution), suggesting that the mobile species are tightly associated with the membrane, which is consistent with previous measurements (K_d < 470 pM) (160).

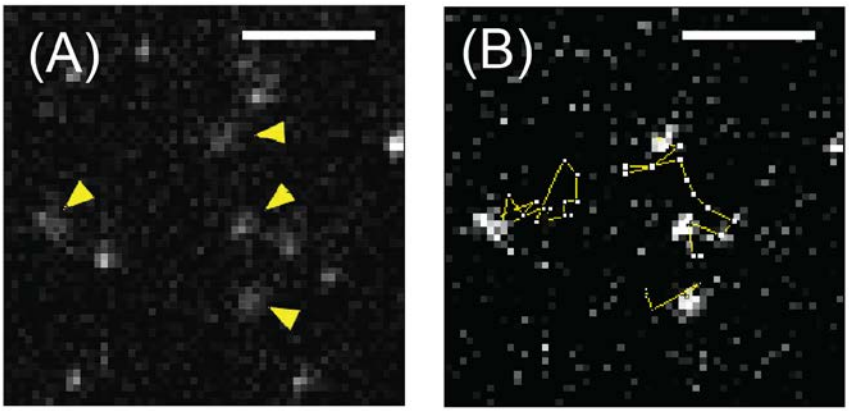

Figure 3-2. Identifying mobile particles. (A) Raw image of membrane-bound oligomers, including both mobile and immobile species. The mobile species are indicated by yellow arrows. To clearly elaborate the mobile and immobile species, only less crowded images are shown here. They do not represent the actual peptide density. (B) The mobile species that remained after image processing and their trajectories indicated by yellow lines. Scale bar is 5 μm.

To monitor the mobile species, we excluded most of the immobile particles by subtracting each frame from the average image obtained from the subsequent ten consecutive frames (Figure 3-2A: raw image; Figure 3-2B: processed image). Mobile particles were tracked by the single-particle tracking method described in Chapter 2-2-3.

An example of the tracked trajectories is shown in Figure 3-3. The mean square displacement (MSD) versus Tau plot for each mobile species is shown in Figure 3-4A. The tracked mobile species were predominantly monomers and dimers, which were categorized based on their fluorescence intensity. Because the mobile species move faster than our camera acquisition speed, fast-diffusing particles often appear dimmer based on peak intensity and wider than slowly-diffusing or immobile particles. Therefore, the accumulated intensity for each oligomer was calculated by fitting a particle to a 2D Gaussian function and integrating the intensity under the area rather than measuring the peak fluorescence intensity. As a result, the accumulated intensities and the corresponding sizes are independent of the diffusion coefficients.

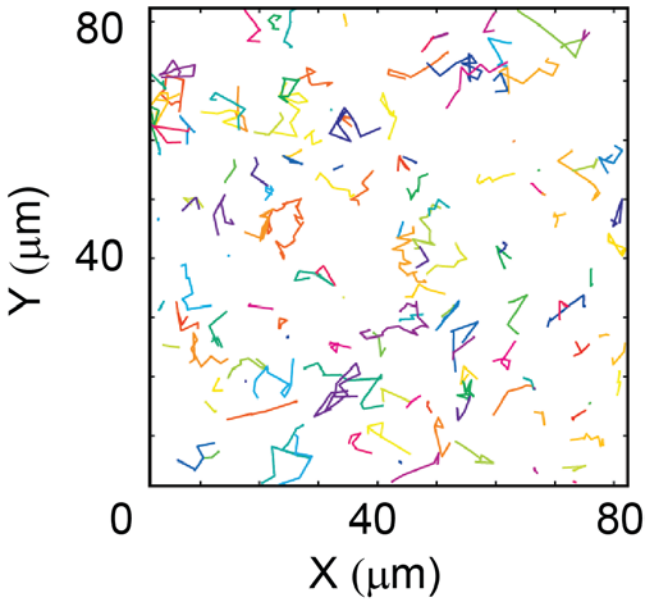

Figure 3-3. The trajectories of mobile species identified by the particle tracking algorithm as mentioned in Chapter 2-3-3.

The diffusion coefficient of tracked particles is determined by fitting the first 2-5 points of the MSD-Tau plot (101, 142):

$$\mathrm{MSD}(\tau) = 4D_{2-5}\tau \quad \text{Eq. 3-1}$$

where D is the diffusion constant. And τ is the time interval as described in the Methods. As shown in figure 3-5A, the D values are not significantly different for most of the species (within 1-1.5 μm^2/second) except Aβ40 dimer (0.8 μm^2/second). The differences can also be observed in the MSD curves (Figure 3-4); almost all the mobile species show a similar trend, whereas most of the Aβ40 dimers possess smaller MSD values at larger values of Tau. Please note that an even larger variation occurs for longer Tau. This is due to the lack of data points for longer diffusing time intervals. The diffusion behavior can be approximated by fitting the first 20 points of the averaged MSD-Tau plot with the following equation (165, 166):

$$\mathrm{MSD}(\tau) = 4D\tau^{\alpha} \quad \text{Eq. 3-2}$$

where α represents the level of confinement; if $\alpha = 1$, the particle motion is a simple two-dimensional Brownian motion; if $\alpha > 1$, the particle motion is driven by an external force; if $\alpha < 1$, the particle motion is anomalous. It has been shown that shorter track length may result in a lower alpha value (165). Here, all the tracked particles for each species have similar distribution of the track length. Therefore, the fitting yields the lowest α value for Aβ40 dimer compared to others (Figure 3-5B), suggesting the motions of mobile Aβ40 dimers are more anomalous than the other species (see Chapter 5 and Figure 3-6 for more detailed analysis).

.

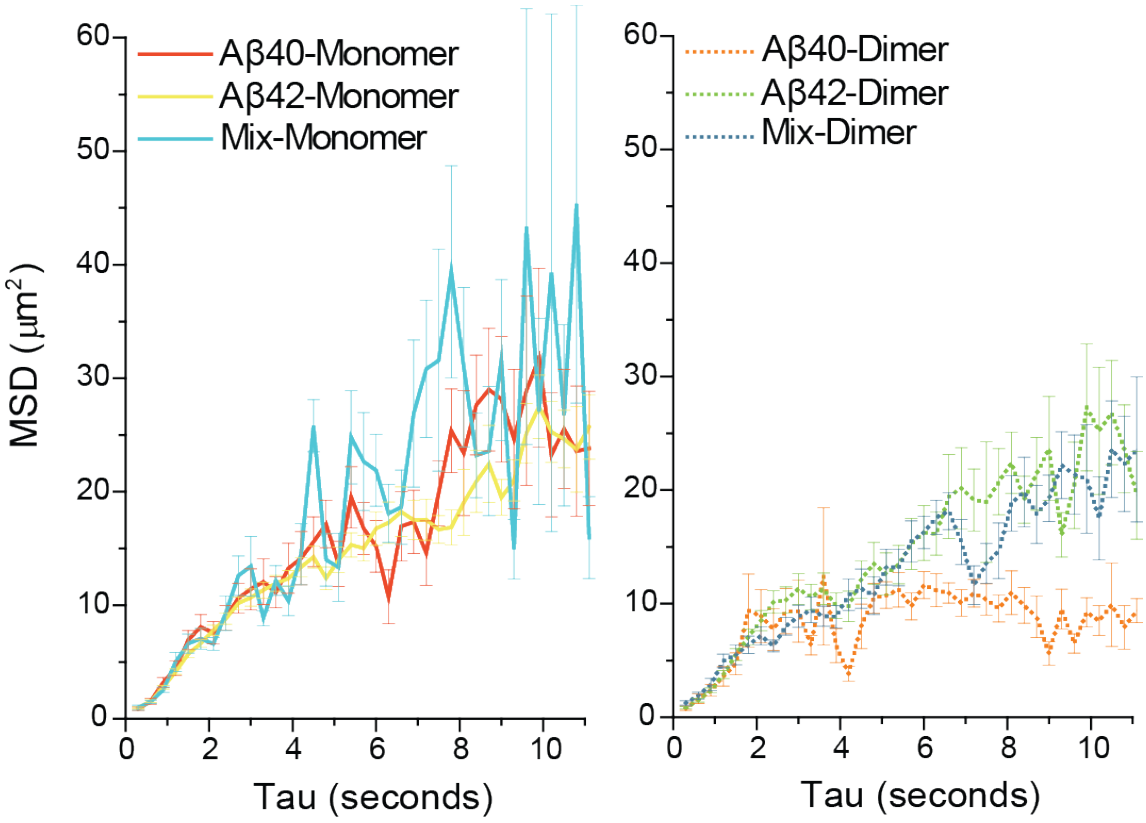

Figure 3-4. MSD curve analysis. MSD-Tau plot for each species. Each MSD curve was averaged from six samples. Each sample contained at least 40 tracked particles. Error bars represent the standard error of the mean.

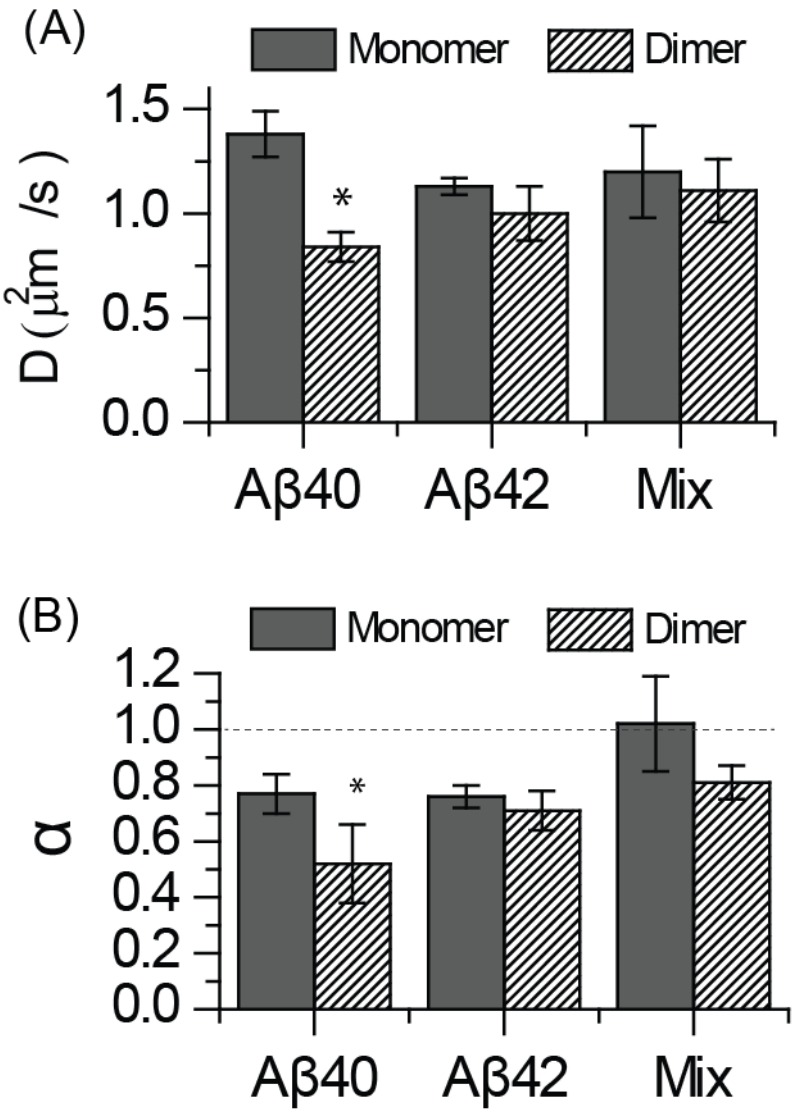

Figure 3-5. Diffusion coefficient and particle motion. (A) The diffusion coefficients of mobile species fitted from their MSD plot as described in the text. (B) The level of confinement (α) of each mobile species fitted by eq. 2. α=1 represents a simple two-dimensional Brownian motion, which is indicated by the dashed line. Error bars represent the standard error (*P<0.05).

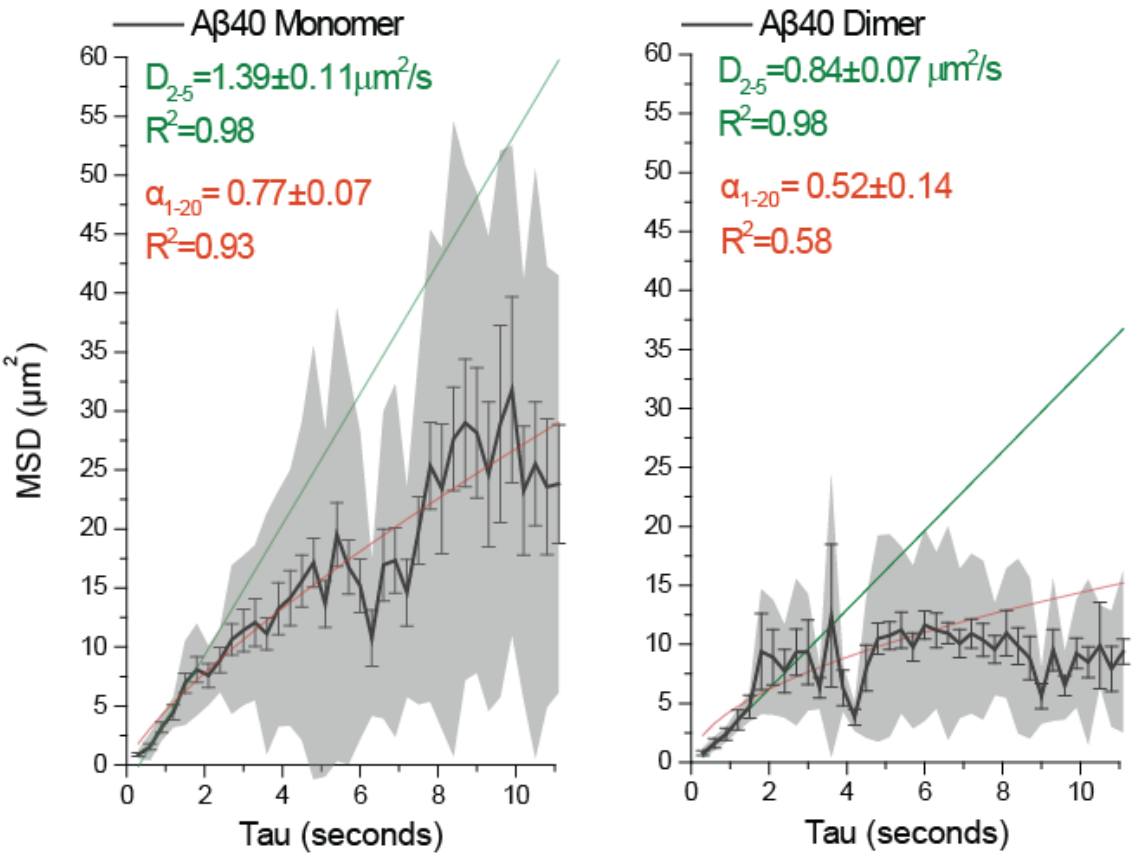

Figure 3-6-1. Aβ40's MSD-Tau curves fitted by both equations 3-1 (green) and 3-2 (red) described in the text. Error bars represent the standard deviation of the mean. The shaded area represents the variation of the data.

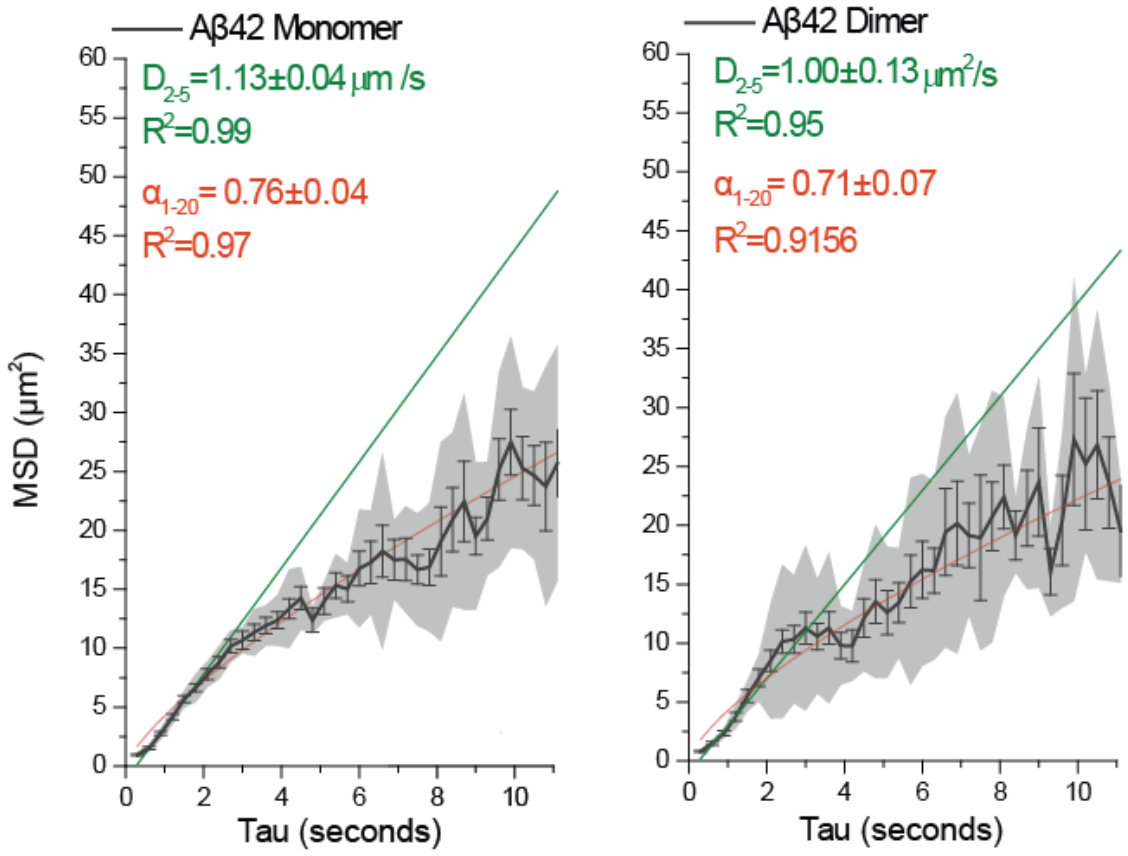

Figure 3-6-2. Aβ42's MSD-Tau curves fitted by both equations 3-1 (green) and 3-2 (red) described in the text. Error bars represent the standard deviation of the mean. The shaded area represents the variation of the data.

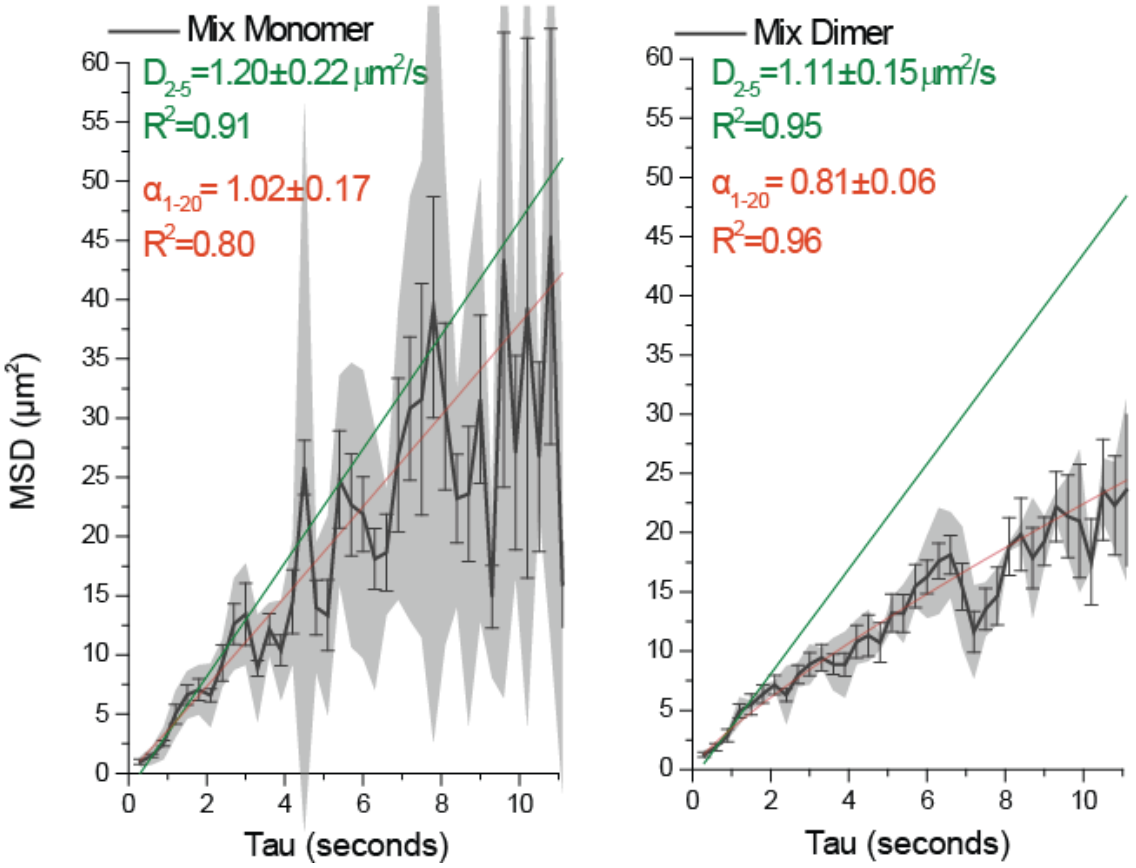

Figure 3-6-3. Mixed species' MSD-Tau curves. The diffusion coefficient $D_{2\text{-}5}$ is determined by fitting the first 2-5 points of equation 1 (green). The level of anomalous diffusion is assessed by fitting the first 20 points with equation 2 (red) described in the text. Note that the MSD values at larger Tau of Aβ40 dimer appear lower than the anomalous fit; this may indicate the motion of mobile Aβ40 dimer is more restricted. However, the detailed model describing such behavior is beyond the scope of this study. Each MSD curve was averaged from at least 40 tracked particles. Each shaded area represents the standard deviation (please note, this represents the spreads of the data, not the error of the data) of MSD curves between tracked particles.

The median oligomer diffusion coefficient at the primary neuron membrane is 0.042 μm^2/second (154). This value is very close to the diffusion coefficient for

extrasynaptic Aβ42 oligomers determined by Renner et al. (0.0341 μm^2/second) (101). The diffusion coefficient for a living cell is, thus, 10- to 100-fold lower than that for the peptides that diffuse in the model membrane, which may be due to the abundance of other membrane-bound proteins, cytoskeletal structures, and lipid-raft domains that hinder the mobility of Aβ.

3-4 Membranes immobilize some dimers and all higher-order oligomers

Figure 3-2A indicates that the membrane-bound Aβ consists of mobile and immobile species. To select the immobile species and exclude the mobile particles, the first ten frames were averaged, and each pixel was divided by its local background (the surrounding 9 by 9 pixels) to exclude pixels with photon counts below a set threshold. Because mobile particles appear dimmer and cover a larger area than the immobile particles, only the immobile particles were identified after this image processing. The size of the membrane-bound immobile oligomers was then determined from their fluorescence intensity (see Chapter 2-3-4). It is believed that when Aβ is immobilized in the lipid bilayer, its N-terminus is not inserted and, hence, remains more flexible than the C-terminus, which likely inserts into the lipid bilayer (151, 167). Because the fluorescent label resides at the N-terminus and is relatively free to fluctuate with the fluid lipid bilayer, most of the photobleaching trajectories are too noisy to resolve the number of steps. Therefore, only clear photobleaching trajectories that contained two and three bleaching steps (dimer and trimer) were collected and further averaged to obtain the corresponding monomer intensity. The oligomer fluorescence intensity was then divided by the monomer intensity to yield the oligomer size (*i.e.*, the number of monomers).

Within one minute of incubation of 4 nM Aβ40 with the supported lipid bilayer, larger membrane-bound oligomers were observed in comparison to the oligomer size determined for Aβ in solution (Figure 3-6). Specifically, approximately 29.5% and 30.3% of the total membrane-bound species are monomer and dimer, respectively, and the remainder consists of higher-order oligomers, whereas the Aβ in solution remains predominantly (90%) monomeric with less than 10% dimer, even after a 24-hour

incubation (Figures 3-1 and 3-6). This result suggests that the lipid bilayer may preferentially incorporate and immobilize dimers and higher-order oligomers rather than the monomer in a short period of time. Oligomers could be incorporated through two pathways: aggregation from monomers facilitated by the membrane or direct insertion of the dimers and higher-order oligomers from the solution (160).

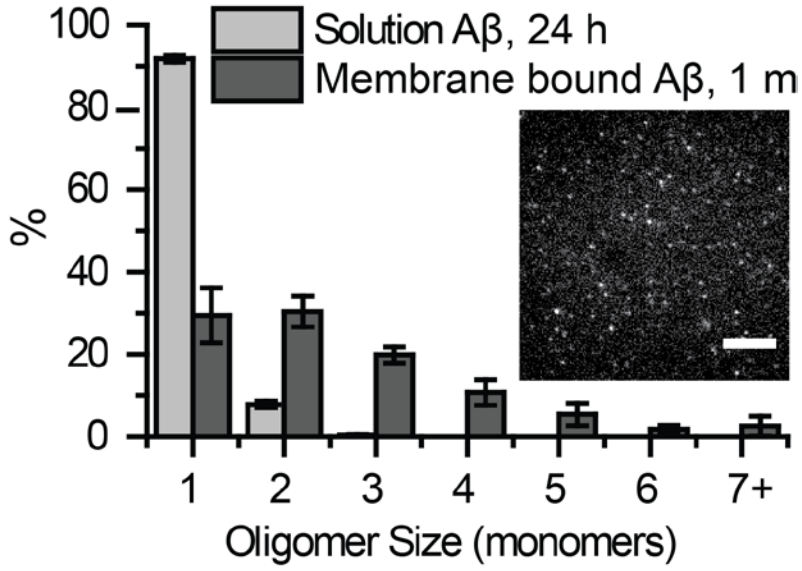

Figure 3-7. A comparison of the size distribution between Aβ in solution and membrane-bound immobile Aβ indicates that the membrane selectively incorporates dimers and higher-order oligomers rather than the monomer. The data for Aβ in solution is adopted from Figure 1. The membrane-bound Aβ40 was immediately monitored after a 1-minute injection of Aβ40 onto the model membrane (inset; image of membrane-bound oligomer right after the Aβ40 injection. The scale bar represents 10 μm). The percentages of the membrane-bound species were calculated from three experiments, and each experiment contained at least 300 oligomers. The error bars represent the standard deviation of the mean.

3-5 Free Aβ40 is more readily incorporated into existing immobile oligomers than free Aβ42, whereas oligomers of the Aβ40:Aβ42 mixture remain unaltered

Building on the observation that the membrane contains immobilized dimers and higher-order oligomers, we monitored the formation of these species over longer periods of time. We incubated 4 nM fluorescently labeled Aβ40, Aβ42, or the 1:1 Aβ40:Aβ42 mixture with the supported lipid bilayer for 24 hours, and the size and oligomer density (i.e., number of fluorescent spots per 100 μm^2) of membrane-bound immobile Aβ was subsequently determined (Figures 3-8A and 3-8D).

To examine whether the membrane-bound immobile Aβ can self-assemble into higher-order oligomers or whether the addition of Aβ peptide from solution is required to support oligomer growth, the initial 24-hour incubation was followed by an additional 96-hour incubation in the absence and presence of the Aβ peptide in solution. In the first case, the membrane was washed with peptide-free buffer to remove Aβ in solution (Figure 3-7B), whereas in the second case, Aβ in solution was present throughout the 120-hour incubation period (Figure 3-7C). Notably, the number and size of oligomers present on the membrane at 24 hours remained unaffected after washing to remove Aβ in solution for both Aβ40 and Aβ42, which suggests that the extensive washing does not greatly affect the system (Figure 3-7).

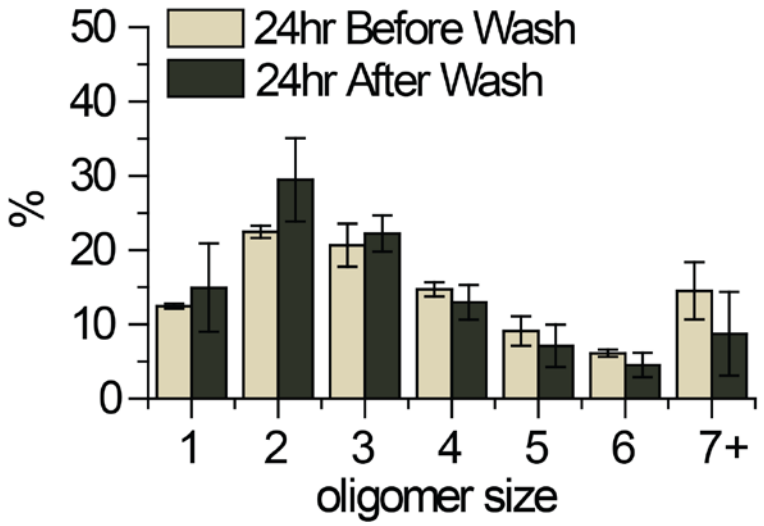

Figure 3-8. Extensive wash of the lipid bilayer does not affect the population of immobile oligomers. The size distributions of Aβ40 oligomers on the model membrane remain similar before and after the solution Aβ is washed off, indicating the extensive wash has minor effect to the membrane and immobile oligomers.

After the initial 24 hours incubation, membrane-bound Aβ40, Aβ42, and the Aβ40:Aβ42 mixture all exhibited similar size distributions consisting of few monomers (~10%), more dimers (~20%), with the remaining 70% of immobile species consisting of trimers and higher-order oligomers (Figure 3-8A), whereas the solution contained approximately 90% monomers. This observation further supports the notion that the membrane facilitates higher-order oligomer formation regardless of whether Aβ40, Aβ42, or their mixture is used. However, the oligomer density indicates that the membrane contains a similar number of Aβ40 and Aβ42 oligomers when the peptides are individually incubated (~9 oligomers/100 μm^2; Figure 3-8D, 24 h), but the membrane incorporates fewer oligomers when Aβ40 and Aβ42 are mixed (~4 oligomers/100 μm^2; Figure 3-8D, 24 h). Given that the amount of total peptides present in the sample was identical for the three cases (4 nM), the mixture of Aβ40 (2 nM) and Aβ42 (2 nM) may have a lower oligomer formation capacity at the model membrane. Interestingly, Chapter 4 and our previous results demonstrate that the mixed peptides sample formed larger oligomers on cellular membranes (154, 161). This apparent contradiction is likely due to the fact that the cell membrane is more complex, contains proteins, and cell-clearance and internalization processes must be considered. A potential explanation to resolve this discrepancy is presented under Chapter 5.

To assess whether membrane-bound Aβ can self-assemble into larger oligomers in the absence of Aβ in solution, we replaced solution Aβ with buffer alone after a 24-hour incubation and continued incubation for a total of 120 hours (this case is labeled as '120 h (x)' in figure 3-8). We found that samples of either Aβ40 or Aβ42 alone contained larger immobile oligomers, whereas the oligomer size distribution of the Aβ40:Aβ42 mixture exhibited a similar distribution as at 24 hours (Figure 3-8B). Additionally, the oligomer density for each sample decreased in comparison to that at 24 hours (Figure 3-

8D, 120 h (x)), whereas the number of total membrane-bound Aβ40 and Aβ42 peptides (including both the mobile and the immobile species) remained similar, except for their mixture which exhibited lower peptide association with the membrane. A plausible explanation is that in the absence of Aβ in solution, both Aβ40 and Aβ42 self-assemble into larger oligomers, thereby reducing the number of immobile oligomers but maintaining the total peptide density (Figures 3-8E and 3-8D, 120 h (x)). However, in the Aβ40:Aβ42 mixture, both small and larger oligomers have equal ability to dissociate into the solution; therefore, both the oligomer and the peptide density are reduced, but the size distribution is maintained (Figures 3-8D and 3-8E, 120 h (x)).

In contrast, when incubated for a total of 120 hours in the presence of Aβ in solution (this case is labeled as '120 h (o)' in figure 3-8), the oligomer size distribution was significantly different for samples of the individual peptides but not for the Aβ40:Aβ42 mixture (Figure 3-8C). The size of the membrane-bound immobile Aβ40 species dramatically increased (73.4% for 7+ species at 120 hours *vs*. 26.7% for 7+ species at 24 hours), and its oligomer density was also slightly higher than at 24 hours (Figure 3-8D, 120 h (o)). These two effects increased the level of Aβ40 bound to the membrane (Figure 4E, 120 h (o)). On the other hand, Aβ42 oligomers grew at a slightly slower rate than Aβ40 oligomers (57.4% for 7+ species at 120 hours *vs*. 24.5% for 7+ species at 24 hours), and the oligomer density was similar to that at 24 hours and slightly lower than that for Aβ40. Therefore, the increase in the total membrane-bound Aβ42 peptide was less dramatic than for Aβ40 (Figures 3-8D and 3-8E, 120 h (o)). Interestingly, the sample containing the Aβ40:Aβ42 mixture did not change in oligomer size or peptide density at 120 hours in comparison to at 24 hours (Figure 3-8, 120 h (o)). Considering that the solution predominantly contained monomers (~90% for either Aβ40 or Aβ42 and ~75% for the Aβ40:Aβ42 mixture), the dramatic growth in the size of either Aβ40 or Aβ42 oligomers and the nearly unaltered oligomer density after 24 hours provides additional support for the notion that the membrane facilitates oligomerization and also indicates that the oligomerization mechanism involves the incorporation of free Aβ into originally immobile oligomers. The additional Aβ peptides originate either directly from Aβ peptides in solution or from membrane-bound mobile Aβ peptides that interact with immobile Aβ. After prolonged incubation, the binding of free Aβ40 is more favorable

than that of Aβ42, whereas the presence of both Aβ40 and Aβ42 effectively arrests oligomerization of either peptide on the membrane. This result appears to contradict the results in Chapter 4 in which the mixed species formed larger oligomers than Aβ42 and Aβ40 alone at the cell membrane. Chapter 5 will summarize and provide potential mechanisms to explain these observations.

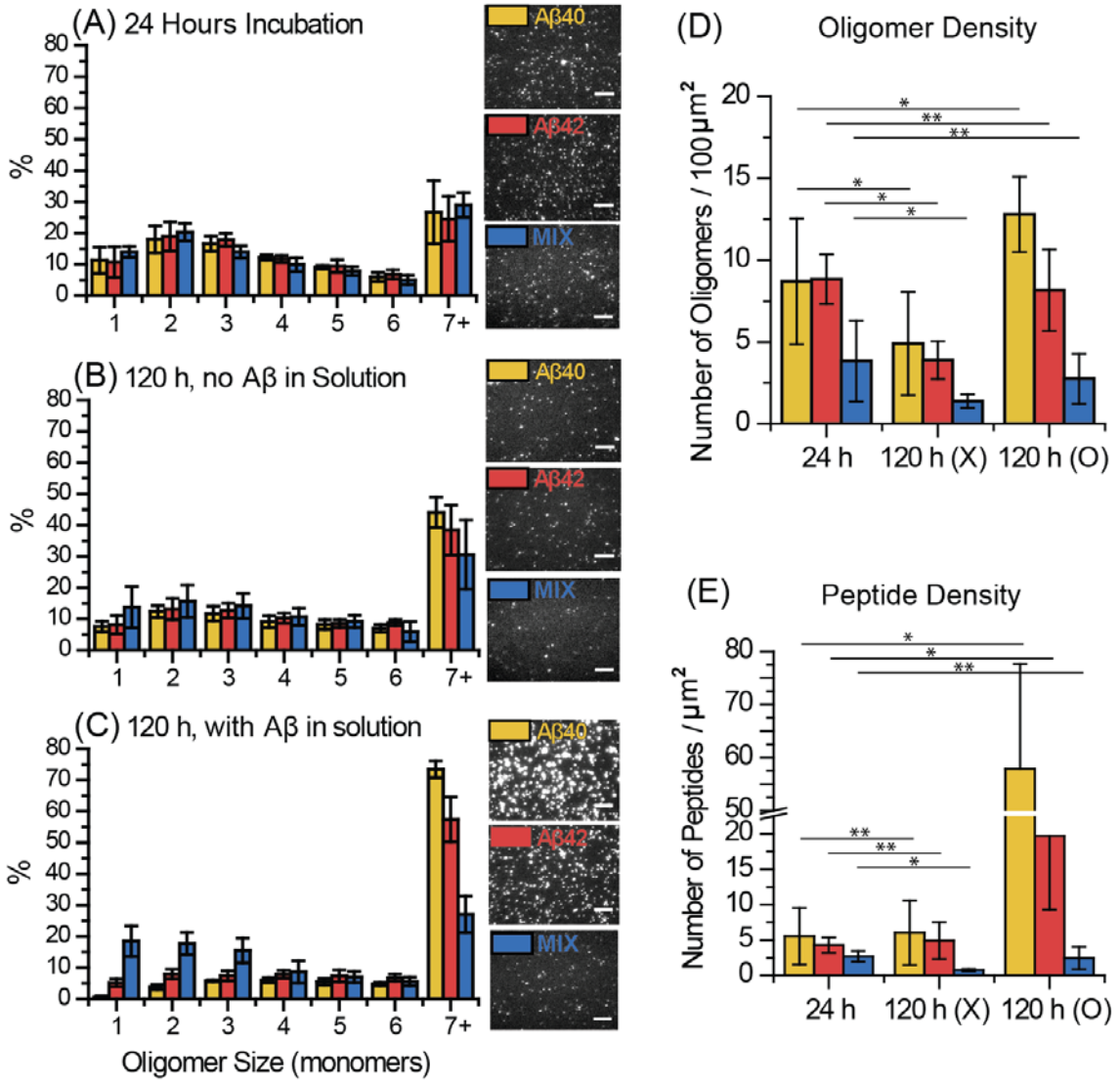

Figure 3-9. Size distribution and density of membrane-bound immobile Aβ. (A) Aβ (Aβ40, Aβ42, or a 1:1 Aβ40:Aβ42 mixture) at a concentration of 4 nM was incubated with the lipid bilayer for 24 hours. (B) Aβ in solution was removed with washing after

the initial 24-hour incubation, and the system was then incubated for an additional 96 hours. The image was collected after a total 120-hour incubation. (C) Aβ was incubated with the lipid bilayer for 120 hours followed by imaging. The raw image of each Aβ sample is shown next to each condition. The scale bars represent 10 μm. (D) Oligomer density (*i.e.*, the number of immobile oligomers) per 100 μm^2. (E) Total peptide density (*i.e.*, the number of monomeric peptides including mobile and immobile species) per μm^2. The percentage represents the fraction of each oligomer size to the total immobile oligomer in each experiment. The data were collected from at least four experiments, and each experiment contained at least 300 oligomers. The error bars represent the standard deviation of the mean (*$P < 0.05$; **$P > 0.05$). Here (x) means incubated in buffer without Aβ and (o) means with Aβ.

CHAPTER 4

STUDIES OF Aβ40 AND Aβ42 INTERACTIONS ON THE PRIMARY NEURON NEURITES

(This work has been published: Chang et al, PLOS ONE, 2013 (161))

4-1 Motivation for study of Stoichiometry of Aβ40 and Aβ42 on the primary neuron neurites

Although *in vitro* model membrane provides a pure platform for monitoring and characterizing individual membrane–bound Aβ species over long periods of time at nanomolar to picomolar peptide levels, an added complexicity is the fact that *in vivo* Aβ oligomers are heterogeneous and metastable, continuously interconverting between species (34, 143, 168) and their cellular membrane interactions are potentially complex and variable. For example, there is evidence that the peptide may associate with specific cellular receptors or protein complexes (e.g. NMDA receptors (92, 93) and α7 nicotinic acetylcholine receptors (94)), it may associate with phosphatidylserine in the membrane (97), or bind to and insert directly into the lipid bilayer (70, 98). Since Aβ is an amphiphilic peptide, the initial binding affinity of Aβ is correlated with the polar interactions and anionic charge of lipid head groups (37). Each of these modes of interaction reflects a different potential pathway to cell disruption.

Recently, our group and other employed single molecule microscopy, both in Total Internal Reflection Fluorescence (TIRF) and confocal to study the assembly and size distribution of Aβ oligomers generated at physiological concentrations on the surface of live cells. Nag et al., first documented small Aβ40 oligomers is capable of attaching to

the PC12 cell membrane and further aggregate. The size of membrane bound oligomer correlates with the Aβ concentration in solution (163). Johnson et al. specifically discovered Aβ40 forms mostly dimer and larger oligomers upon binding to SH-SY5Y neuroblastoma cells, those oligomers also induces mild, sporadic calcium leakage (153). Narayan et al. also found both Aβ40 and Aβ42 form larger oligomers on Murine hippocampal HPL cell as compared to mostly monomers in solution. Larger oligomers also diffuse slower and their interactions with membrane are inhibited by the presence of ATP-independent molecular chaperones (162). Overall we found that at these low peptide concentrations, only insignificant oligomerization occurred in solution even after five days of incubation, whereas the membrane facilitated the formation of surface bound oligomers with an obviously larger size distribution.

Alzheimer's disease causes loss of neurons and formation of amyloid plaques near hippocampus region. Therefore, choosing a hippocampal cell as a platform will be more physiological relevant. Johnson et al., first observed Aβ40 as well as Aβ42 initially form larger oligomers on rat's primary hippocampal neurites than on glass slides. Especially with 1 nM peptide in solution, Aβ40 oligomers do not grow over the course of 48 h, Aβ42 oligomers grow slightly, and oligomers of a 1:1 mix grow substantially.

In the present study we extend our previous work to focus on synergistic interactions between Aβ40 and Aβ42 during their assembly into oligomers on the surface of primary cultured neurons, at physiological concentrations of peptides. As discussed above, such synergy is potentially of great significance for the development of our understanding of the molecular events underlying cell disruption in AD. The identification of those oligomers that develop on the membrane at nM peptide concentrations is of special relevance.

4-2 FRET Confirms Aβ40 and Aβ42 Form Heterogeneous Species on Neurites

In order to explore potential cooperative interactions between Aβ40 and Aβ42 when they are incubated together with cultured neurons, we employed a FRET pair that enables us to distinguish the heterogeneous oligomers from homogeneous oligomers;

only when Aβ42 binds to Aβ40 and forms heterogeneous oligomer do the systems generate a FRET signal (Figure 4-1). In addition, labeling Aβ40 and Aβ42 with fluorophores that emit significantly different wavelengths enables us to distinguish Aβ40's signal from Aβ42 when both are present. Aβ40 is labeled with HilyteFluor555, a Cy3 derivative as the FRET donor, and Aβ42 is labeled with HilyteFluor647, a Cy5 derivative as the FRET acceptor. The Förster radius (R_0) for this pair is estimated ~ 53 Å (169), providing a sensitive reporter on the distance between these two fluorophores.

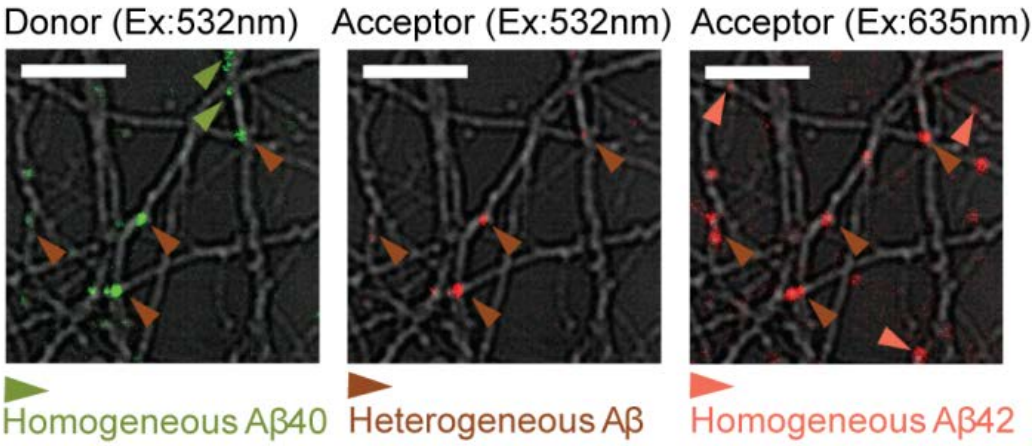

Figure 4-1. Mixed Aβ40-HL555 and Aβ42-HL647 are incubated with neurons and show FRET. Homogeneous Aβ40 (green arrow) is imaged by 532 nm excitation but does not show signal in acceptor's channel. Heterogeneous Aβ (brown arrow) is determined by FRET in Acceptor's channel upon 532 nm excitation. Homogeneous Aβ42 (pink arrow) is imaged by 635 nm excitation but without FRET. Scale bars are 10 μm.

When Aβ40 and Aβ42 are mixed together, three different classes of oligomers develop on the neurites: those that contain Aβ40 only (homogeneous oligomer), those made of Aβ42 (homogeneous oligomer), and mixed Aβ40/Aβ42 (heterogeneous oligomer). Only the heterogeneous mixed species show FRET signal (Aβ40 and Aβ42 that are co-localized within the laser beam focus but do not form heterogeneous oligomers do not show FRET). Three quantitative steps are used to identify the FRET species: first, possible FRET pairs are selected by exciting the sample at 532 nm and recording the position of the spot that emitted in Aβ42 channel. Second, those selected

fluorescent spots showed in Aβ40 channel with lifetime above 0.53 ns are excluded as autofluorescence. Third, the remaining selected spots showed in Aβ42 channel are double confirmed as the FRET signal by excluding those spots that do not co-localize with spots directly excited by the 635 nm laser. Using this process, the heterogeneous species is filtered out from homogeneous Aβ40 and Aβ42. The homogeneous Aβ40 is determined as those spots that showed fluorescence lifetime below 0.53 ns but do not co-localize with the heterogeneous species. The homogeneous Aβ42 is the one that is directly excited by 635 nm but does not co-localize with the heterogeneous oligomer (see Chapter 2-4-2).

4-3 Aβ40 and Aβ42 Form Mainly Dimers on Neurites and Show Little Growth upon Incubation

We have previously shown that 1 nM of either HilyteFluor647 labeled Aβ40 (or Aβ42) forms predominantly dimers on neurites, whereas the incubating media still contains 90% monomeric Aβ (154). This may suggest dimeric Aβ preferentially interacts with the membrane. Similar results have been observed in the current study for using 2 nM Aβ40-HL555 or Aβ42-HL647. Aβ40 species bound to the neuritic membrane are mostly dimeric showing minimal additional growth even after additional 48 hours of incubation. Aβ42 behaved similarly, though some additional growth beyond that at 10 minutes was detected at 48 hours with the appearance of some trimer and larger specie (Figure 4-2). The incremental growth of Aβ42 (compared to what we reported earlier (154)) could be due to a higher peptide concentration used in the current experiment than the previous work (2 nM vs. 1 nM). Nevertheless, the important point is that the overall oligomeric growth for both Aβ40 and Aβ42 is limited. We note that for the dimers found on the membrane at 10 minutes, we cannot distinguish whether these are formed from bound monomers through assembly on the membrane or from residual dimers in solutions.

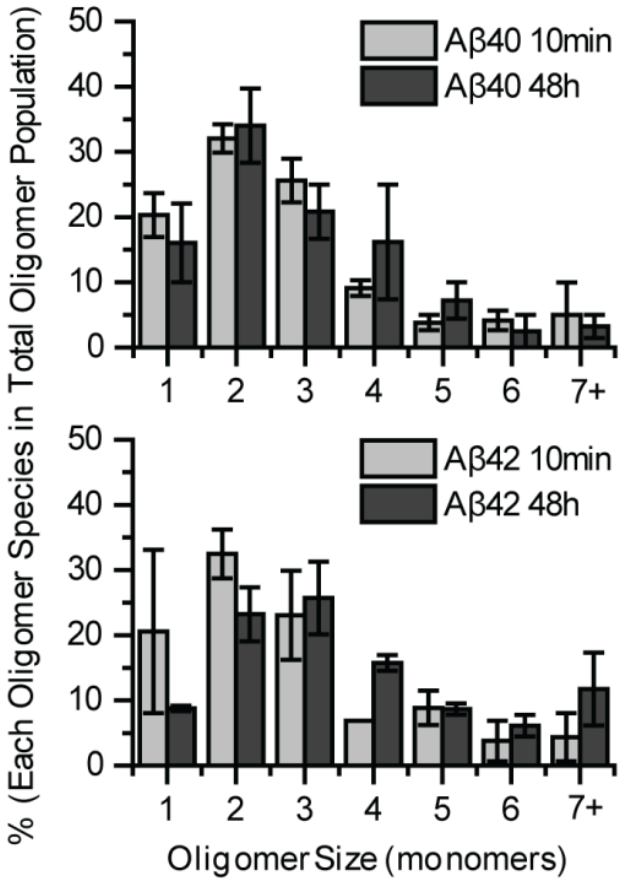

Figure 4-2. Aβ40 or Aβ42 oligomers form mainly dimers and show little growth on neuritis. 2nM Aβ40-HL555 or Aβ42-HL647 was incubated with primary hippocampal neurons for 10 minutes and 48 hours before imaging. Comparison of the oligomeric size distribution between 10 minutes and 48 hours shows limited growth for both Aβ40-HL555 (Mann-Whitney U test, $p > 0.1$) and Aβ42-HL647 (Mann-Whitney U test, $p = 0.001$). The distribution is normalized to total Aβ oligomers. Percentages of each condition were calculated from two different experiments, 5 images each. Each image contained at least 50 oligomers. Error bars represent standard deviation of the mean. The percent is obtained by normalizing to the total number of oligomers.

4-4 Number of Heterogeneous Species (i.e., oligomers comprised of both Aβ40 and 42) Increases Over Time due to Continuous Binding of Aβ42 to Heterogeneous Oligomers on the Neurites

As illustrated in Figure 4-3, when a mixture of 2 nM Aβ40 and 2 nM Aβ42 is incubated with cultured neurons at the same time, four fluorescent species are detected: homogeneous Aβ40 oligomer (green), homogeneous Aβ42 oligomer (red), heterogeneous Aβ40-Aβ42 oligomer showing FRET (brown), and co-localized Aβ40-Aβ42 oligomers with no FRET (blue). To get information on the changes of Aβ40 and Aβ42's populations over time, we compared the percentage of each species at two incubation time points. By counting the number of different oligomer species on the neurite, we found that less than 10% of either Aβ40 or Aβ42 oligomers co-localized without showing a FRET signal and that most of the co-localized assemblies containing 40 and 42 showed FRET. Approximately 35% of Aβ40-HL555 oligomers formed FRET pairs with Aβ42-HL647 after 10 minute incubation, and this number increased to ~45% by 48 hours (Figure 4-3A). This was not due to dissociation of homogeneous Aβ40 oligomers because the total number of Aβ40 oligomers remained unchanged while the total number of Aβ42 oligomers slightly increased over time (Figure 4-3B). Therefore, the increased fraction of Aβ40 oligomer that is bound to Aβ42 was due to continued binding of solution Aβ42 to homogeneous Aβ40 oligomers over time.

Figure 4A reveals that ~25% of Aβ42 oligomers formed FRET pairs with Aβ40 after 10 minute incubation, and the 25% remained nearly constant over 48 hours. In addition, at 48 hours the total number of Aβ42 oligomers was significantly higher than Aβ40 oligomers (Figure 4-3B). These results indicate that not only did the additional Aβ42 bind to homogeneous Aβ40 oligomers thereby increasing the number and fraction of heterogeneous Aβ40-Aβ42 over time, but that additional Aβ42 also bound to homogeneous Aβ42 oligomers and likely also formed new oligomers. This explains the increased number of heterogeneous Aβ40-Aβ42 oligomers (and the increased fraction of heterogeneous Aβ40) but the much smaller effect on Aβ42 distribution. This is illustrated by the diagram in Figure 4-4.

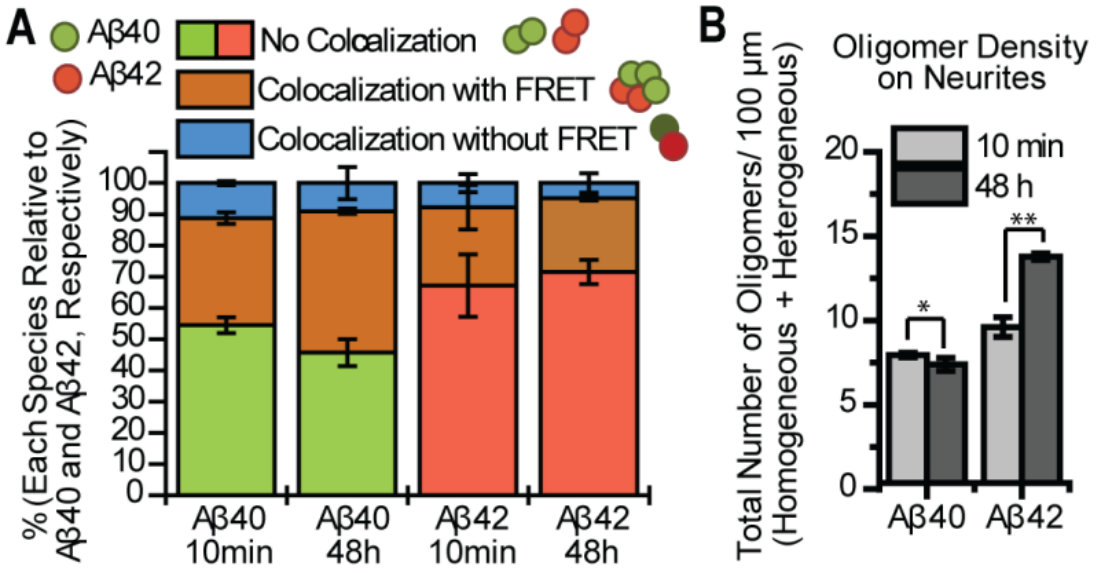

Figure 4-3. Heterogeneous species increases over time due to continuous binding of Aβ42 to the neurites. 2 nM Aβ40 and 2 nM Aβ42 were mixed and incubated with cultured neurons at the same time. By comparing the population changes of each species, we get general idea of how these species interact over time. (A) The relative number of oligomers of each species in each sample (percentage of each species). The blue shading (colocalization without FRET) represents the co-localized Aβ40 and Aβ42 that do not show a FRET signal. This species accounts for at most 10% for both Aβ40 and Aβ42. The green shaded sections represent the percentage of homogeneous Aβ40 in total Aβ40 species, and show the fraction of homogeneous Aβ40 to decrease over time. The red bar represents the percentage of homogeneous Aβ42 in total Aβ42 species. This number remains almost unchanged over time, indicating the fraction of homogeneous Aβ42 remains unchanged. The brown bar represents the percentage of heterogeneous mixed species in total Aβ40 (left two) or Aβ42 (right two) species. The fraction of heterogeneous species among the whole Aβ40 species increases over time (from 35% to 45%), whereas the fraction of heterogeneous species among whole Aβ42 species remains similar. (B) The density (number of Aβ42 per 100 μm) of Aβ42 oligomers on the neurites (including both homogeneous and heterogeneous species) is slightly higher than Aβ40 at 10 minutes and becomes significantly larger by 48 hours, whereas the total number of Aβ40 is only slightly changed (unpaired two-tailed t-test, *$P > 0.1$ and **$P < 0.05$). Data was averaged from two different experiments, at least 5 images each and each image

contained at least 50 oligomers. Error bars represent standard deviation of the mean. Figure 5 provides a pictorial display of the implications.

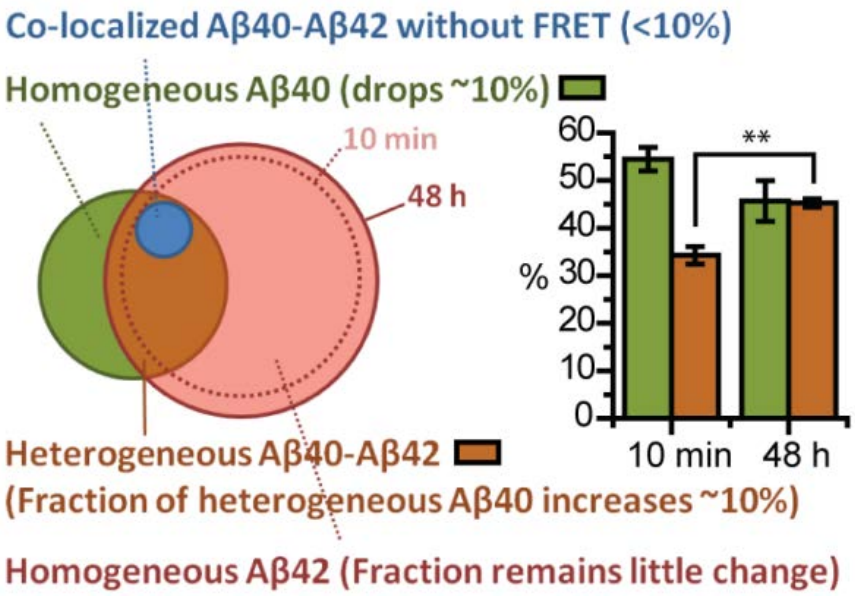

Figure 4-4. Diagram of the number of Aβ40 and Aβ42 oligomers on the neurites. The color assignments are the same as in Figure 4. Green and red circles represent the total number of Aβ40 and Aβ42 species respectively (including both homogeneous and heterogeneous species). The overlap region of the two circles (brown area) represents the heterogeneous species. And the blue circle inside the brown area represents those heterogeneous species that do not show FRET signal. At 10 minutes, there are slightly more Aβ42 species than Aβ40, therefore larger red circle. By 48 hours, the number of Aβ40 species remains similar; therefore the green circle remains the same. The number of Aβ42 species increases over 48 hours (the dashed red circle depicts the population at 10 minutes). Since additional Aβ42 also binds to homogeneous Aβ40, the fraction of heterogeneous species among Aβ40 increase (unpaired two-tailed t-test, **$P < 0.05$), and the fraction of homogeneous Aβ40 decreases over 48 hours.

4-5 Heterogeneous Oligomers are Larger than Homogeneous Oligomers

In order to study how different Aβ species oligomerizes on the membrane over time, we further analyzed the size of each type of membrane bound oligomer by measuring their fluorescence intensity (see Chapter 2-5-3). This examination of the relative oligomer sizes (number of peptides in a single oligomer) in the sample containing both Aβ40 and Aβ42 reveals that both homogeneous Aβ40 and Aβ42 remain mostly dimeric over 2 days (Figure 4-5A and 4-5B), very similar to samples incubated with only Aβ40 or Aβ42 (Figure 4-2).

For the heterogeneous oligomers, Aβ40's emission is quenched due to energy transferring to Aβ42, therefore to obtain the true Aβ40's original emission intensity, we collected all the photons emitting from both donor and acceptor and corrected the quantum yield and detection efficiency (see Supporting Information). The size of Aβ42 was measured by direct excitation of 630 nm laser. To calculate the size of each heterogeneous oligomer, we rounded each Aβ40 and Aβ42's calculated size to the nearest integer and summed them up (Figure 4-5C). The minimal heterogeneous oligomer is of course dimeric (~5%), while ~20% are heptamers or larger at 10 min. This suggests the interactions between Aβ40-Aβ40 and Aβ42-Aβ42 favor dimeric structure on the membrane, where the interaction between Aβ40-Aβ42 favors trimeric, tetrameric and larger structures, which show further growth on the membrane.

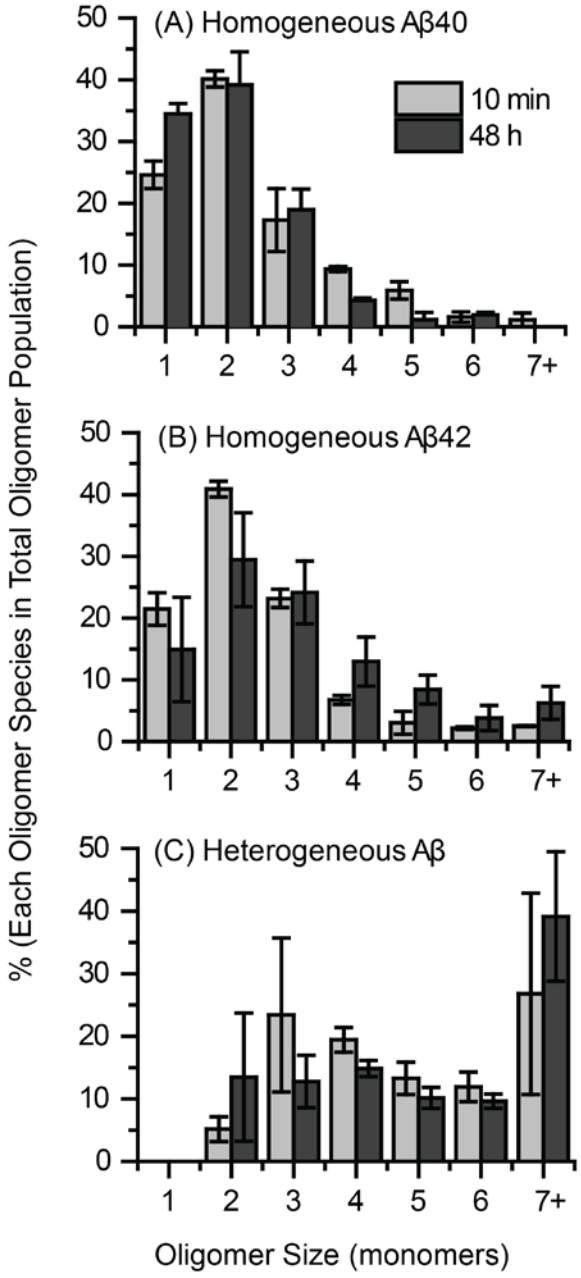

Figure 4-5. Heterogeneous oligomers are larger than homogeneous oligomers. (A) Homogeneous Aβ40 remains mainly dimeric on the neurites over 48 hours. (B) Homogeneous Aβ42 also forms mainly dimeric with slight increase in size over 48 hours. (C) Heterogeneous species contains mainly trimer and tetramer and many other oligomers larger than heptamer. The size of heterogeneous species was calculated by summing the number of Aβ40 and Aβ42 in that particular mixture. Percentages of each condition were calculated from two different experiments, at least 5 images each. Each

image contained at least 50 oligomers. Error bars represent standard deviation of the mean.

4-6 Determining the Relative Fractions of 40 and 42 in Heterogeneous Oligomers

We further analyzed the stoichiometry of Aβ40 and Aβ42 in each heterogeneous oligomer by comparing the size distributions of Aβ40 and Aβ42 inside the oligomer. Results show the fraction of Aβ40 in the heterogeneous species has declined by 48 hours (Figure 4-6A) which is caused by the continued binding of Aβ42 from solution to homogeneous Aβ40 oligomers (primarily monomeric and dimeric Aβ40) while additional Aβ40 does not bind (Figure 4-4 and 4-5). As a result, by 48 hours, the newly formed heterogeneous species contain more monomeric and dimeric Aβ40. Also, the increase in the monomeric fraction is larger than the homogeneous Aβ40, this could indicate that Aβ40 in heterogeneous oligomers may be cleared by cell or dissociate into solution. In contrast, the relative fraction of Aβ42 in the heterogeneous oligomer increased markedly, producing about 4 fold larger oligomers (7+) at 48 hours (Figure 4-6B). Combining this knowledge with the fact that Aβ42 continues to bind to neurites over time (Figure 4-4), where the size distribution of homogeneous Aβ42 remains largely constant (Figure 4-5B), suggests Aβ42 binds equally to homogeneous Aβ42 and new locations on the neurite, but it preferentially binds to the heterogeneous species, increasing the fraction and size of Aβ42 in the heterogeneous species (Figure 4-6B).

Another way to present the stoichiometric relationship is by calculating the ratio of Aβ42/Aβ40 for each heterogeneous oligomer (Figure 4-6C). At 10 minutes, there are typically more Aβ40 than Aβ42 in each heterogeneous species (Aβ42/40 ratio < 1, below the dashed line). By 48 hours, there are more Aβ42 adding to the heterogeneous species, shifting the Aβ42/Aβ40 ratio to larger than 1, above the dashed line. This is due to continued binding of Aβ42 from solution to heterogeneous oligomers.

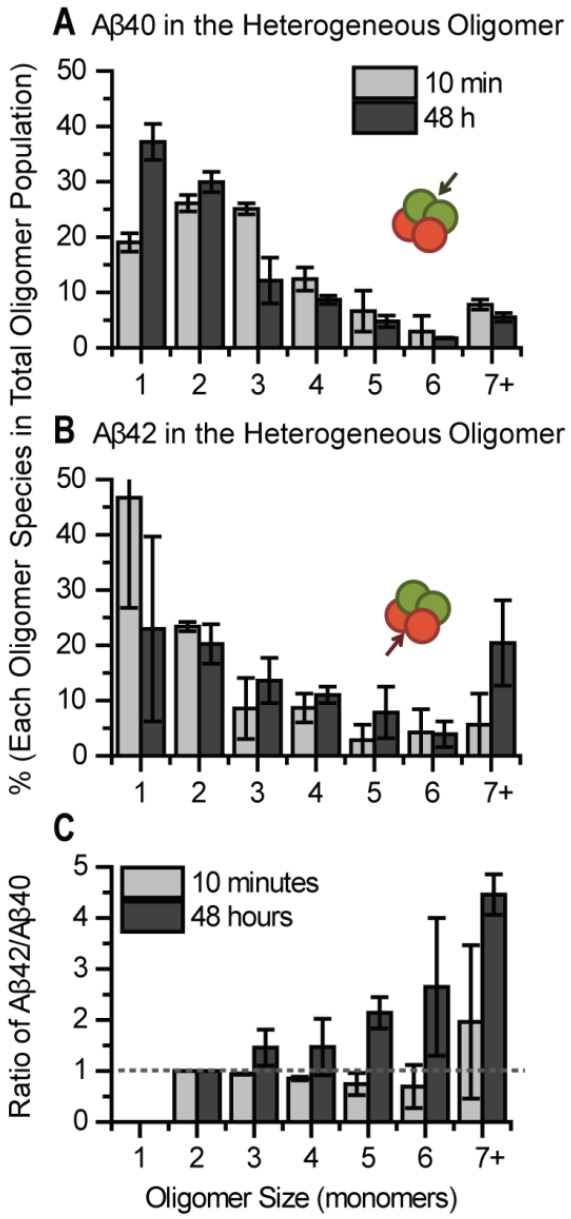

Figure 4-6. Aβ42 fraction in the heterogeneous oligomers increases dramatically over time but not Aβ40. (A) The size of Aβ40 in the heterogeneous species (as indicated by the green arrow) shifts to smaller species after 48 hours (Mann-Whitney U test, p = 8.6E-7). (B) The size of Aβ42 in the heterogeneous species (as indicated by the red arrow) increases considerably up to 48 hours (Mann-Whitney U test, p = 6.3E-7). (C) The ratio was calculated by dividing the number of Aβ42 monomer by the number of Aβ40 monomer in each individual heterogeneous species. The dashed line indicates ratio 1 at which value the amount of Aβ42 is equal to Aβ40. Data was calculated from two

different experiments, at least 5 images each. Each image contained at least 50 oligomers. Error bars represent standard deviation of the mean.

CHAPTER 5

DISCUSSION AND CONCLUSIONS

5-1 Introduction

The pure interaction between Aβ isoforms (*i.e.* Aβ40, Aβ42, and the mixture) and the model membrane is first discussed in this Chapter. This model membrane study provides a foundation of structural information for different oligomer species. This structural information can further be applied to the Aβ aggregation observed on the neuronal cell membrane. Moreover, a detailed discussion of the single molecule FRET experiment reveals synergistic interactions between Aβ40 and Aβ42 on the rat primary neuronal cells. Combining results obtained from the model membrane and the neuronal cell membrane, a more complete picture of Aβ and live-cell membrane interaction will be provided. Implications from our studies may also explain the toxicity from different oligomers and Aβ42:Aβ40 ratios observed in several studies.

5-2 Aβ Oligomerization on the model membrane

When incubated in solution at nM concentrations Aβ binds to phospholipid membranes initially forming mostly mobile monomers and dimers (~3 peptides/μm^2) as well as a small number of immobile species composed of larger oligomers (these contain ~1 peptide/μm^2). Both mobile and immobile species binds tightly to the membrane but at very low saturation levels (approximately 2 peptides per million lipids) calculated based on a cross section for a lipid molecule of 1 nm^2 (Figure 3-9E). Similar low Aβ saturation level in has been previously reported (152, 160, 170), but is atypical for membrane-binding peptides that typically reach saturation at approximately 1 peptide per 100 lipids.

The basis for the low solubility of monomeric Aβ in the lipid bilayer is unclear; however, it is not likely due to the presence of imperfections or "sweet spots" in the membrane (or the glass substrate) to which the peptide adheres, for the following reasons: 1. The monomers are predominantly freely mobile on the membrane and are not anchored in fixed spots. Indeed, when fluorescently labeled lipids are added during membrane preparation, the membranes exhibit full fluorescent recovery after photo bleaching (FRAP), confirming the normal mobility of the lipids. 2. Free diffusion was also observed for Aβ bound to agarose-supported lipid membranes (which also exhibited Aβ saturation at a similar peptide/lipid ratio) (152), as well as on membranes supported on glass that was cleaned through extensive washing. 3. Similar results have been reported for Aβ on large liposomes (170). Notably, the low saturation level is not due to the presence of a small fraction of "impure peptide" in our samples that exhibits high membrane-binding affinity because our results indicate an identical level of membrane saturation when the peptide concentration in solution is increased from 2 nM to 100 nM (160), which would have increased the amount of available "impure peptide" and binding by an identical factor. The basis for the low saturation density for peptide binding remains under investigation.

The stationary oligomers were found to be immobilized over prolonged time periods. One explanation is that Aβ may come into contact with the membrane-supporting cover glass since the length of an Aβ chain extended in a β strand is about 15 nm (151), significantly longer than the lipid bilayer thickness (~5 nm) plus the water layer between the lipid bilayer and the cover glass (~0.1 nm) (135, 171). FRAP studies also indicated that the lipids remain mobile in the presence of Aβ in solution even after 120-hour incubation, further indicating that oligomer movement is not due to immobilization of the lipids (see Chapter 2-3-2). Although the glass-binding mechanism remains unclear, it is worth noticing that the density of the immobilized oligomers did not correlate with glass surface imperfections as detected in scanning electron microscope (SEM) images of cleaned cover glass; the latter revealed a smooth surface at a 10-nm resolution (Figure 5-1). Although defects involving local chemically modified lipids or glass may not be detected by fluorescence or SEM, from our observations and those previously reported, we hypothesize that the Aβ immobilization indicates that the peptide

adopts a conformation that enables it to insert across the lipid bilayer and interact with the glass surface.

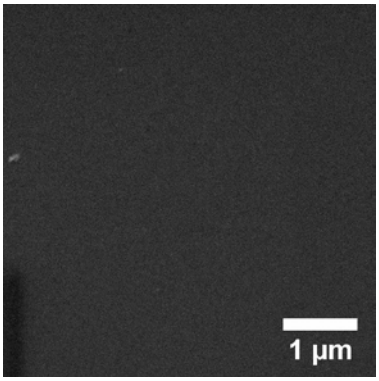

Figure 5-1. SEM image of pre-cleaned cover glass shows no detectable defect.

More than 90% of Aβ in solution is monomeric (Figure 3-1) while the membrane-bound immobile species contain less than 30% monomer (Figures 3-7, and Figure 3-9). Based on the idea that immobilized peptides and oligomers are transmembrane and bind to the glass, it is possible that less immobilized monomer indicates that the monomeric conformation exhibits a lower probability of inserting across the membrane to interact with the glass surface. Similar to antimicrobial peptides, amyloid peptides are amphipathic; their monomeric form lies in the intermediate region between the lipid head group and acyl chains as shown in Figure 5-2 (151, 167, 172).

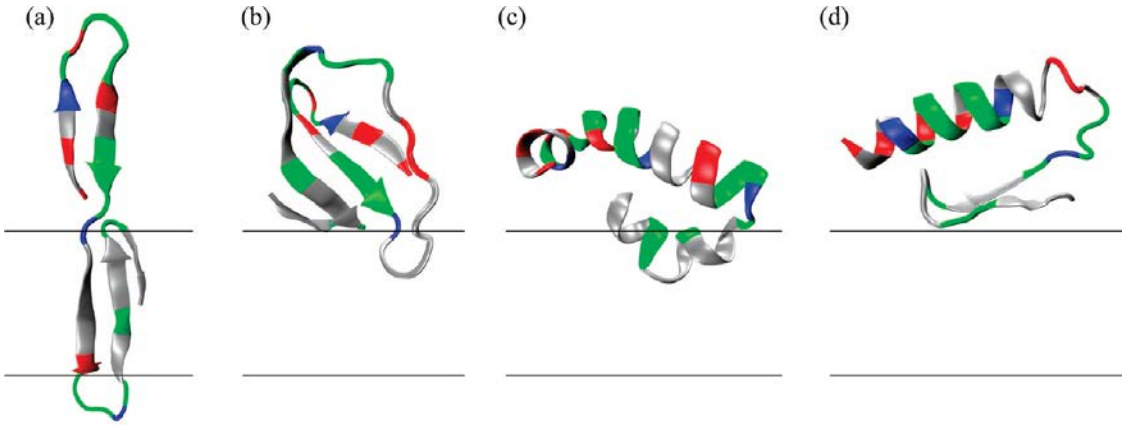

Figure 5-2. Low-lying structures in terms of potential energy are shown for the Aβ42 monomer. (a) the membrane-spanning β-sheet; (b) the β-sheet structure adsorbed on the surface, which was found to be lowest in energy; (c) the helix-kink-helix structure at the membrane-water interface, which was identified as the next most stable structure; and (d) a structure with a mixed helical/ β-sheet conformation. The residues are colored according to their physicochemical properties (blue, basic; red, acidic; gray, hydrophobic; green, polar); the sequence of Aβ42 is D1-A2-E3-F4-R5-H6-D7-S8-G9-Y10-E11-V12-H13-H14-Q15-K16-L17-V18-F19-F20-A21-E22-D23-V24-G25-S26-N27-K28-G29-A30-I31-I32-G33-L34-M35-V36-G37-G38-V39-V40-I41-A42. The black lines denote the boundary between the hydrophobic core and polar headgroup regions of the membrane (151).

In contrast, less than 20% of the dimer is present in solution, but the membrane-bound immobile oligomers contain approximately 30% dimer one minute after the Aβ solution was incubated with the membrane (Figure 3-7). *In vivo* single-molecule studies also indicate that neuronal cell membranes contain predominantly dimers under physiological conditions (153, 154, 161, 162). A recent study using hAPP transgenic mice also indicates that Aβ in the interstitial fluid (ISF) of a 24-month-old mouse brain is primarily monomeric, whereas the membrane-associated Aβ contained more dimers (173). These all in line with the rapid dimer association shown in Figure 3-6, suggesting that most of the dimers (*i.e.*, Aβ40, Aβ42, or a heterogeneous dimer) form structures that allow them to rapidly incorporate into the membrane and form complete transmembrane conformation as predicted by the simulation model as shown in Figure 5-3 (151).

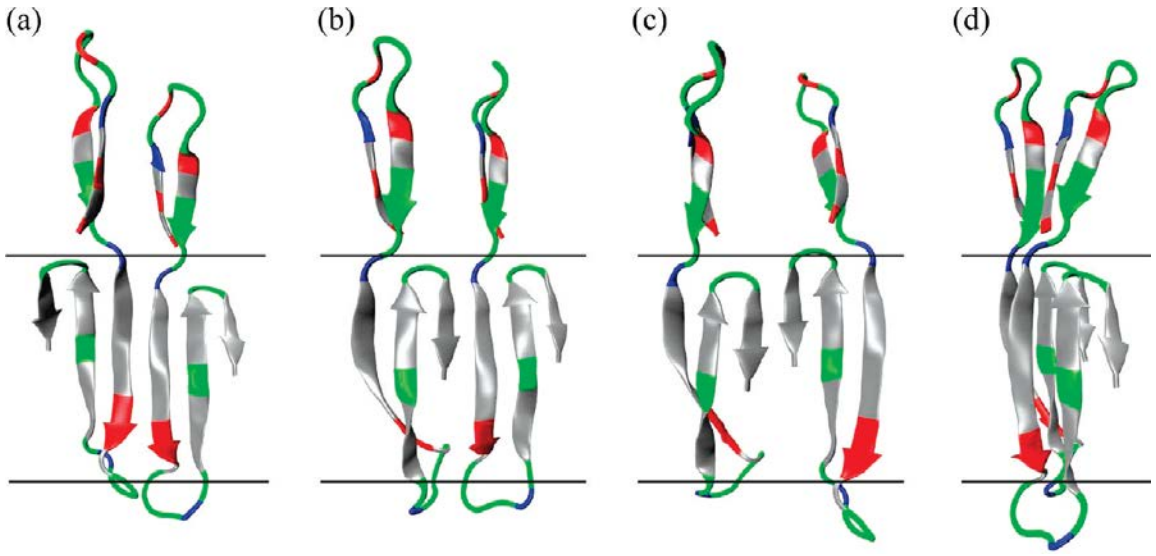

Figure 5-3. Dimer structures in the membrane. (a) CNNC, (b) NCNC, (c) NCCN, and (d) 2NCb. The residues are colored according to their physicochemical properties: blue, basic; red, acidic; gray, hydrophobic; green, polar. The black lines denote the boundary between the hydrophobic core and polar headgroup regions of the membrane (151).

Not only does the dimer dominate the initial immobile oligomer formed at the membrane as shown in Figures 3 and 4, but certain dimers maintain a structure that allows them to freely diffuse in/on the membrane (Figure 3-2). Interestingly, the diffusion coefficient of mobile Aβ40 dimer is the lowest and its motion is more anomalous than other mobile species (Figure 3-4 and 3-5). This may be due to the lack of the four additional hydrophobic residues at the C-terminus of the Aβ40 dimer as compared to Aβ42 dimer. Perhaps the Aβ40 dimer can adopt a fully transmembrane conformation faster and is likely to be affected by the glass surface and stationary oligomers (obstacles).

This existence of both mobile and immobile dimers suggests that dimers may serve as an important intermediate in the Aβ aggregation and immobilization process since all larger oligomers are immobile. Indeed, endogenous Aβ dimers isolated from AD patients impair synaptic plasticity and memory (59). The Aβ dimer can also induce tau hyperphosphorylation and neuritic degeneration (2). While these results are not sufficient

to conclude that the dimer directly impairs neuronal dysfunction, they emphasize the importance of the dimer.

Initial oligomer immobilization is an important step for nucleation-dependent oligomer growth at the membrane (Figure 3-9). Significant oligomer growth occurs only in the presence of either Aβ40 or Aβ42 in solution. These additional peptides interacting with the lipid surface have been suggested to increase the internal surface tension within the lipid bilayer due to collision, or due to non-ideal acyl chain packing (174). The formation of a fully transmembrane oligomer may release this tension, as it creates an additional membrane surface without distorting and thinning the acyl region. Additional oligomer growth on the originally immobilized seeds (*i.e.*, immobilized oligomers) can also aid in minimizing the surface tension without generating new oligomer sites.

Oligomer growth was observed after a 120-hour incubation of Aβ with the membrane; the impact of the additional two residues at Aβ42's C-terminus is readily apparent from the slower growth of immobile Aβ42 oligomers in comparison to immobile Aβ40 oligomers (Figure 3-9). A study using Monte Carlo simulation suggests that these two additional hydrophobic residues render Aβ42 more likely to remain within the lipid tail groups, whereas the C-terminus of Aβ40 is likely to reach the other side of the lipid head groups as shown in Figure 5-4 (167).

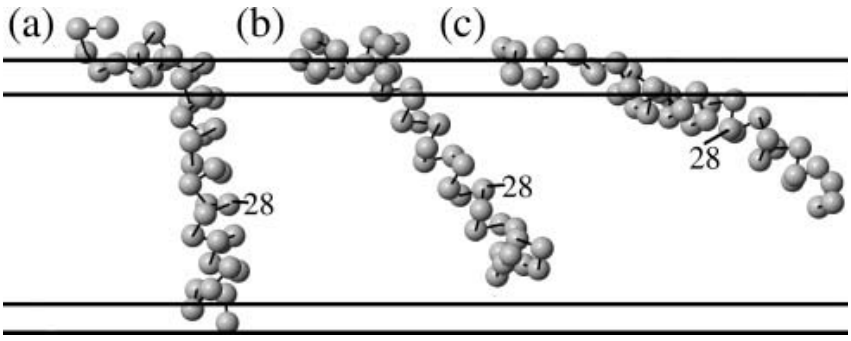

Figure 5-4. Primary inserted conformations of the Aβ peptide. We find that in every case, the inserted peptides can adopt essentially three different conformations. Mutations appear to alter the percentage of steps the peptide spends in each conformation but do not fundamentally change the conformations. (a) Transbilayer. The peptide inserts with the last several residues near the C-terminus in the lower lipid head region; the portion

crossing the bilayer is roughly helical. (b) Fully inserted. Similar to (a), except the last several residues are not anchored in the lower head region, meaning that the conformation is fairly flexible. (c) Partially inserted. Similar to (b), except now much more of the peptide is tethered to the upper head region by the polar residues 22–23 and 26–28, whereas before only residues 1–15 or so were in the upper head region. The conformations shown are for Aβ40, but Aβ42 has similar conformations with two additional residues (Isoleucine and alanine) at the C-terminus. And Aβ40 has higher chance of adopting conformation (a), whereas Aβ42 has higher chance of adopting conformation (b) (167).

A recent *in vivo* study indicates that endocytosis of Aβ42 requires dynamin to provide energy, whereas endocytosis of Aβ40 is energy independent making Aβ40 more easily internalized (175). In addition, we have previously shown that the level of cell membrane-bound Aβ40 was reduced by approximately twofold more than the level of Aβ42 in the absence of free Aβ in the incubation media within 24 hours (154). These results are likely due to the two additional hydrophobic residues in Aβ42 that capture Aβ42 among the lipid tail groups, whereas Aβ40 is able to more readily cross the membrane. Put together, these results support our hypothesis that immobilization on the model membrane is likely due to the formation of a transmembrane Aβ structure that may be immobilized on the glass surface. Because the structure of Aβ40 enables it to insert across the membrane more readily than Aβ42, the formation of higher-order immobile oligomers are more significant, as shown in Figure 3-9.

In Chapter 4, the single-molecule studies on rat primary hippocampal neurons indicate that when 1-4 nM of an Aβ40:Aβ42 mixture is incubated with neurons, larger aggregates develop at the cell membrane in comparison to those created by either Aβ40 or Aβ42 alone. We also found that, Aβ42 accumulates at the cell membrane to a greater extent than Aβ40 (154, 161). This result seemingly contradicts our current results (Figure 3-9); however, the internalization rates of the two peptides into the cell have to be considered. As discussed above, Aβ40 more readily traverses the bilayer membrane and hence can be more readily internalized by neuronal cells than Aβ42. This can explain

why Aβ42 accumulates at the neuronal membrane to a greater extent than Aβ40. When Aβ40 is mixed with Aβ42, a lower oligomer density, and marginal oligomer growth, are observed even after prolonged incubation (Figure 3-9). We hypothesize that the interaction between Aβ40 and Aβ42 inhibits further oligomer growth at the supported lipid bilayer, a process that requires free Aβ to adopt a favorable transmembrane conformation, interact with existing immobile seeds, and insert across the membrane. In *in vivo* experiments this cross interactions between Aβ40 and Aβ42 may lead to reduced cell internalization and larger aggregates on the neuronal cell, which may be more toxic, as larger Aβ oligomers correlate with higher cytotoxicity (60, 61). We previously performed single-molecule fluorescence resonance energy transfer (FRET) to study the stoichiometry of the growth of the Aβ40:Aβ42 mixture on the primary neuronal cell. The results suggest that heterogeneous oligomer growth is more rapid than homogeneous Aβ40 or Aβ42 oligomer growth, and the rapid growth is due to continuous Aβ42 binding to existing seeds (161). Kuperstein et al. have shown that neuronal spontaneous postsynaptic depolarization is inhibited when cells are incubated with an Aβ40:Aβ42 ratio of 7:3 (10). Figure 5-5 summarizes the structural implications for Aβ oligomer growth based on observations of Aβ aggregation at the model membrane.

Potential pathways that lead to neuronal cell death in AD have been intensely studied over the last decade (9). However, the molecular mechanism underlying Aβ-membrane interactions has not been characterized due, in part, to the complex nature of these interactions and to technical challenges. However, given the inherent complexity of biological membranes, we utilized a structurally and compositionally simplified model membrane system combined with single-molecule microscopy, which enabled us to quantitatively study the molecular mechanisms and oligomerization by different Aβ species. In this system the monomer is highly mobile in the membrane, whereas the dimer constitutes an intermediate state and can be either mobile or immobile. Higher-order oligomers may form from the initial immobilized membrane-crossing “seeds”. Immobilization is thus an initial step in oligomerization, the latter occurring upon the incorporation of free Aβ into immobilized oligomers. The formation of higher-order oligomers, however, is only possible if they are not rapidly removed from the cell surface. Additional hydrophobic residues at the Aβ42 C-terminus likely reduce its ability to fully

traverse the membrane and to be readily cleared by the cell in comparison to Aβ40. Interestingly, Aβ42 appears to interfere with the ability of Aβ 40 to form a fully transmembrane structure, which results in dramatic growth of mixed oligomers at the cell membrane. This study provides direct evidence for synergistic interactions between Aβ40 and Aβ42 on a model membrane. The experimental approaches herein are not limited to Alzheimer's peptide research but can be more generally applicable to other protein-membrane interaction studies.

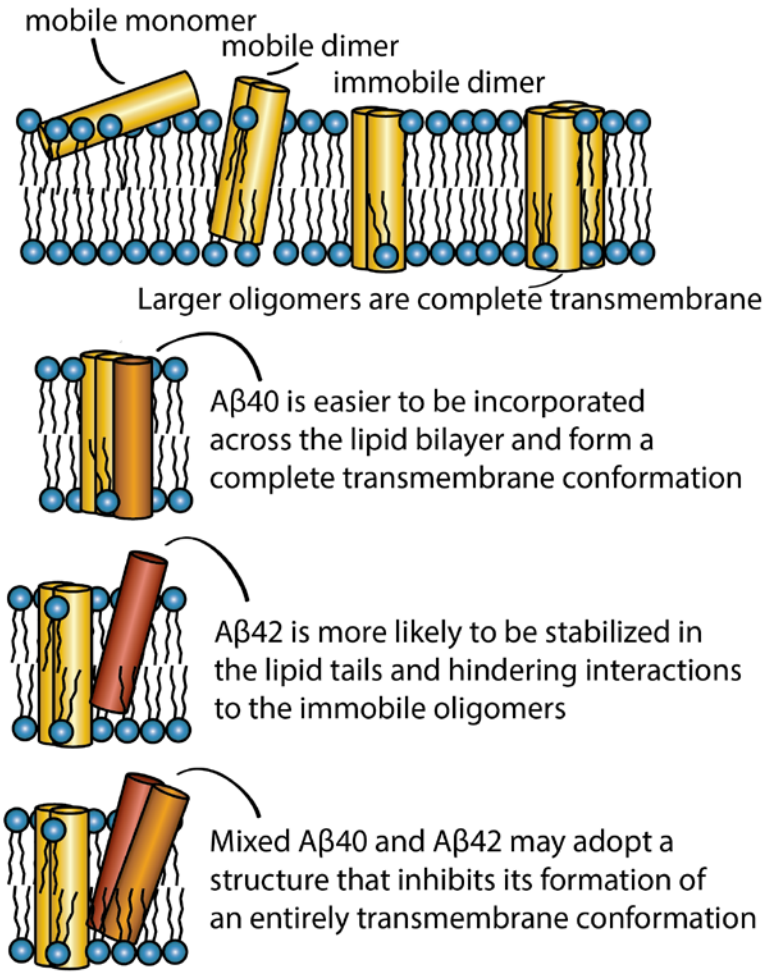

Figure 5-5. Models that summarize the structural properties of monomer, dimer, and different Aβ isoforms on the membrane.

5-3 Aβ Oligomerization on the neuronal cells

In vivo studies have shown that high ratios of Aβ40/Aβ42 may protect neurons from the deleterious effects of Aβ42 (116, 117). This might suggest that lowering the absolute amounts of Aβ in AD patients could be less crucial than the restoration of the correct ratios of Aβ peptides. However, little is known about possible cooperative effects between Aβ42 and Aβ40 under *in vivo* conditions. Aβ42/Aβ40 dependent aggregation kinetics has been measured and extensively studied revealing that a slight increase in the Aβ42 fraction has a significant effect on oligomerization rate and cytotoxicity (10, 11, 15, 126–129). However, the peptide concentrations used in these studies (μM) were at least 10^3 times higher than the physiological relevant concentration (pM-nM). Although one

could argue the local *in vivo* Aβ concentration might transiently reach μM levels, the overall kinetics and mechanisms of Aβ oligomerization almost certainly behave differently from those at physiological peptide concentrations on neuronal membranes. Moreover, the distribution of the various Aβ oligomers in solution is both concentration and buffer/ionic strength depend, and hence the Aβ oligomers prepared in solution may differ significantly from membrane bound oligomers (176). To avoid these complications, we directly monitored Aβ40 and Aβ42 oligomers that form on the surface of primary hippocampal neurons under physiological conditions, using single molecule microscopy. Labeling Aβ40 with the FRET donor and Aβ42 with the FRET acceptor reveals the stoichiometry of homogeneous and heterogeneous Aβ oligomers that may further explain the pathogenesis of AD. Direct observation of Aβ on cultured neurons removes the ambiguity caused by SDS-PAGE treatment (See review (176)), and provides structural information for each type of oligomer on or inside the membrane which is new information.

We have shown that when dissolved as monomeric peptide at nM concentration, both Aβ40 and Aβ42 remain predominantly monomeric (~90%) in solution (154) even after prolonged incubation up to 120 hours (Figure 3-1). On the cell membrane each peptide formed a distribution of small oligomers peaking at dimers and with less than 10% of the peptide found in species larger than tetramers (Figure 4-2). Moreover, these oligomers formed quickly (i.e., within 10 min) and showed very little further growth over 48 hours (Figure 4-2). This behavior has also been reported earlier using single molecule microscopy (153, 154, 162).

Molecular dynamics simulation has shown that Aβ dimerizes strongly when it interacts with anionic lipid membrane (177) which agrees with the findings in the model membrane work where Aβ incubated at nM concentration with a model membrane (POPC:POPG 80:20), Aβ initially binds as rapidly diffusing monomers (160) and then slowly oligomerizes to form mostly immobile dimers and trimers. It seems likely that this last step is also the first step for oligomerization of Aβ on the neuronal membrane following binding.

A plausible explanation for the abundance and immobility of dimers/trimers is that these species incorporate into the membrane (as opposed to be surface bound) and are both more stable and less mobile in this state. Hence the membrane selectively incorporates the dimer/trimer through a direct insertion mechanism (160). In the case of model membranes the oligomers' immobilization may indicate that the bound peptide cross the bilayer and become anchored to the surface of the supporting cover slip. A parallel picture for neurites is that binding to surface protein complexes or to intracellular/cytoskeletal elements may be the origin for the oligomers' immobility.

In the current study we observe that at nM concentration neither Aβ40 nor Aβ42 oligomerizes on the neuronal membrane to form significant populations of oligomers larger than tetramers, even after prolonged incubation. The peptide forms a stable mixture of small oligomeric species that changes very little between 10 min and 48 hours. This behavior is in sharp contrast to Aβ behavior at μM concentrations where the peptide oligomers form rapidly and continuously grow over time to eventually form fibrils within few hours (10, 11). No fibrils appear at 1-4 nM peptide concentrations either in solution or on the neuronal membrane up to 48 hours. Moreover, the model membrane data revealed that when incubated at nM concentrations with a model membrane, both Aβ40 and Aβ42 develop significantly large oligomers over time; again, this does not happen when the peptides interact with neuronal membranes and is likely due to the equilibrium balance between cell clearance and continued peptide binding from the solution (154).

In what perhaps constitutes the most important observation made in the current study, a dramatic change in the oligomerization reaction sequence was discovered when the cells were exposed to a 1:1 mixture of Aβ40 and Aβ42. Significantly larger membrane-bound oligomers developed within 10 min, with species larger than tetramers constituting over 50% of total peptide (as opposed to less than 10% for homogeneous peptide samples, see Figure 4-5) and with some additional growth occurring over 48 hours. Concomitantly, the fraction of monomeric peptide completely disappeared and the dimeric fraction was dramatically reduced.

These observations clearly suggest a synergy of binding between Aβ40 and Aβ42 to the neuronal membrane where initial Aβ40 binding creates "nucleation sites" whose

structure favors additional Aβ42 binding to form larger, Aβ42-rich, assemblies. Direct evidence for the formation of these heterogeneous oligomers is provided by FRET (Figures 2-8 and 4-1) which reveals that the chromophores attached to the two different peptides are indeed within several nanometers of each other. An alternate model, where the initial Aβ40 binds to a membrane-associated factor (protein) and this complex binds Aβ42 with high affinity cannot be ruled out; however, there is no compelling indication for this in our data (Aβ40 binding does not show any site-preference).

Our results are summarized in Figure 5-6 and show that when equal concentrations of Aβ42 or Aβ40 were incubated with neurons, slightly more Aβ42 oligomers formed on the neuronal membrane (Figure 4-3 and 4-4), and the Aβ42 species grew slightly larger than Aβ40 (Figure 4-2 and 4-5). A possible explanation for this is that Aβ42 possesses a higher affinity towards the membrane, hence the higher membrane concentration. In light of recent evidence showing that cells can internalize single Aβ oligomers (175), an alternate explanation is that the clearance of membrane bound Aβ42 is slower than that of Aβ40. Moreover, the use of FRET at the single molecule level reveals a strong cooperativity between Aβ40 and Aβ42, the oligomers appear to grow exclusively by adding Aβ42 to "seeds" formed by heterogeneous Aβ40/42 and (mostly dimeric) homogeneous Aβ40, which later becomes heterogeneous oligomers and accelerate further attraction of Aβ42, as reflected by the fact that the ratio of Aβ42/Aβ40 increases in individual oligomers with increasing size (Figure 4-6).

The importance of this observation is threefold: (1) the increase in the size of heterogeneous oligomers may also indicate the oligomer aggregation rate is faster than the cellular clearance rate; (2) the presence of membrane bound Aβ40 is necessary for Aβ42 to form heterogeneous oligomers and without Aβ40, the homogenous Aβ42 grows only moderately; and (3) the AD brain may contain abundant membrane bound heterogeneous oligomers, which accelerate the association of cerebrospinal fluid (CSF) Aβ42 and increase the burden of Aβ42 in the membrane, resulting in the decreased Aβ42/Aβ40 ratio in CSF but an increased ratio in the plasma membrane.

A lowering of the level of monomeric Aβ42 in human CSF has been widely validated as a robust biomarker for the diagnosis of AD, even in its earliest clinical stages

(178–182). Mechanistically, the progressive accumulation of insoluble Aβ42 enriched deposits in brain parenchyma has been suggested to explain the decline in the level of the highly self-aggregating Aβ42 monomer in both CSF and brain interstitial fluid (179, 183). Aβ42 has been shown to associate with loosely membrane-bound pool of brain parenchyma in plaque rich mice brains, thereby dropping Aβ42/Aβ40 ratio in the CSF but increasing this ratio in the membrane (173). These observations support the notion that the association of Aβ42 with the membrane is more favorable than the association of Aβ40 and is possibly accelerated by membrane bound heterogeneous oligomers.

Larger Aβ oligomers have been shown to correlate with higher cytotoxicity (60, 61). The finding here that larger peptide oligomers contain increasing fractions of Aβ42 raises the interesting possibility that the higher toxicity is due to the fact that heterogeneous Aβ oligomers are more toxic than homogeneous ones. Jin et al. reported that synthetically made Aβ40 dimers (produced by crosslinking Aβ40 S26C via a disulfide bond) always required much higher concentrations (>100-fold) to induce cytoskeletal disruption comparable to those of the endogenous dimers isolated from AD cortex (100). Given that heterogeneous oligomers are larger and have been reported in Alzheimer's disease brain (59), we hypothesize that endogenous Aβ is likely to contain heterogeneous Aβ which form larger oligomers and can cause higher cytotoxicity than synthetic pure Aβ40 or Aβ42. An experiment with cross-linked heterogeneous synthetic dimer could support this hypothesis.

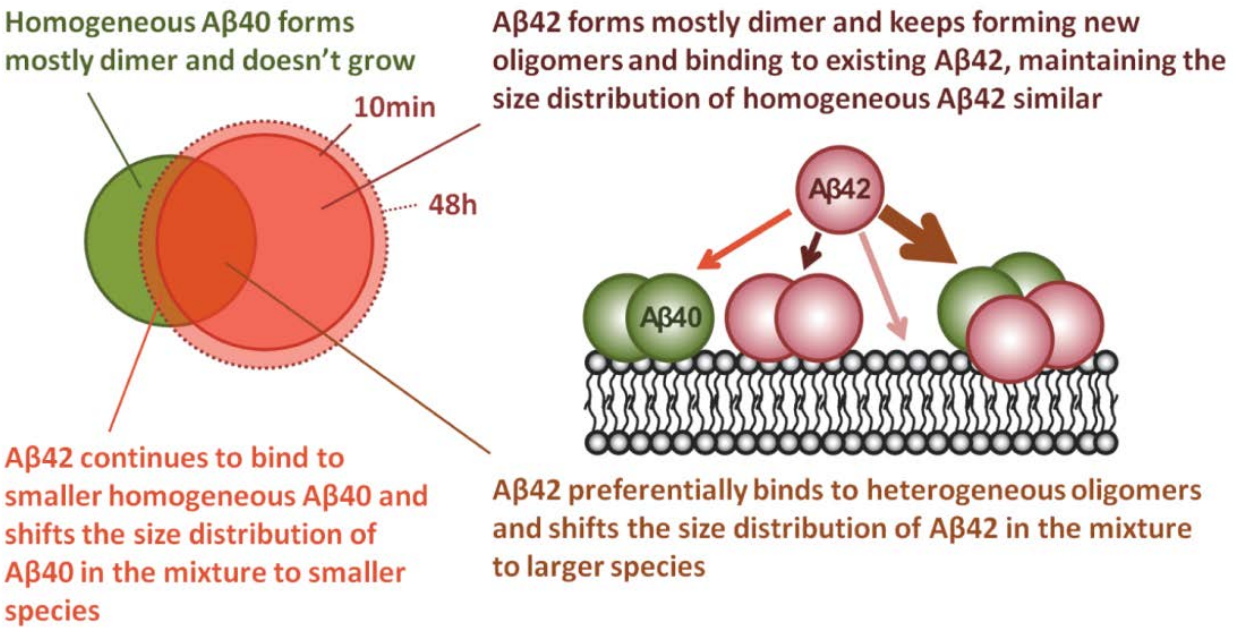

Figure 5-6. Summary of synergistic interactions between Aβ40 and Aβ42 on the neurons. For Aβ40, the total number of membrane bound oligomers (including both homogeneous and heterogeneous species) does not change, suggesting either no solution Aβ40 binds to the membrane or the association and dissociation of solution Aβ40 to the membrane reach the equilibrium. Size of homogeneous Aβ40 remains mostly dimeric. For Aβ42, the total number of membrane bound oligomers increases. Solution Aβ42 preferentially binds heterogeneous species, increasing the Aβ42/Aβ40 ratio in each mixture. Solution Aβ42 also binds to homogeneous Aβ40, increasing the number of heterogeneous species and shifting the fraction of Aβ40 in the heterogeneous oligomer to a slightly smaller species. However, the solution Aβ42 forms new oligomers and also binds to homogeneous Aβ42, therefore maintaining the size of homogeneous Aβ42 unchanged.

5-4 Conclusion from the model membrane to the cell membrane

The oligomeric Aβ species believed to feature in Alzheimer's disease are known to be numerous and to dynamically interchange, making their characterization challenging and the assignment of disease-related effects to specific oligomers a daunting task. In addition, the concentration of Aβ in bodily fluids is in the nM range or lower, making its study by traditional approaches difficult. Single-molecule microscopy lends itself to work at physiological peptide concentrations and allows one to directly follow the evolution of monomeric Aβ on the model membrane (based on TIRF) and as well as the neuronal membrane (confocal microscopy with FLIM). These studies provide a detailed molecular mechanism for the synergistic interaction Aβ40 and Aβ42 on the membrane, and these are particularly relevant to the detection and characterization of the initial stages of Aβ-induced AD-associated pathology. Here is a brief comparison of Aβ oligomerization behaviors on the model membrane and neuronal cells:

	On Model Membrane *	On Neuronal Membrane **	Hypothesis
Aβ40	1. Monomer is very mobile. 2. Mobile dimer has confined motion. 3. Dimer is the major immobile species upon initial incubation. 4. Dramatic oligomerization over 120 hours.	1. Dimer is the major species of immobile population over 48 hours. 2. No oligomer growth over 48 hours. Probably reach the equilibrium between membrane association and cell internalization.	Higher chance of forming complete transmembrane conformation, especially when it forms dimer and larger oligomers.
Aβ42	1. Both the monomer and dimer are very mobile. 2. Dimer is again the major species initially. 3. Oligomer growth is less than Aβ40.	1. Dimer is the major species of the immobile population which later shifts to slightly bigger oligomers over 48 hours. 2. Oligomer density is slightly higher than Aβ40.	Less chance than Aβ40 to form the complete transmembrane conformation.
Mixture	1. Both the monomer and dimer are very mobile. 2. Dimer is also the major species initially. 3. Density of immobile oligomer is less than Aβ40 and Aβ42. 4. Almost on oligomer growth over 120 hours	1. Trimer and tetramer are the major species. 2. Oligomers growth rapidly via recruiting free Aβ42 over 48 hours.	Aβ40 and Aβ42 inhibit each other and form poorly transmembrane conformation.

* Do not need to consider cell internalization mechanism for the model membrane system.

** Mobile Aβ could not be observed on the neuronal membrane under the confocal imaging method. This is due to image acquisition speed is much slower than the movement of mobile species.

Our findings here provide detailed insight into structure, dynamics and the mechanism of different types of membrane bound Aβ. Therefore, besides considering the reduction in the quantity of Aβ as a therapeutic strategy, the pathogenic interactions between different Aβ isoforms may also be important. Moreover, the methodologies developed herein are not limited to Alzheimer's research and are applicable to several other protein-membrane studies and live-cell imaging.

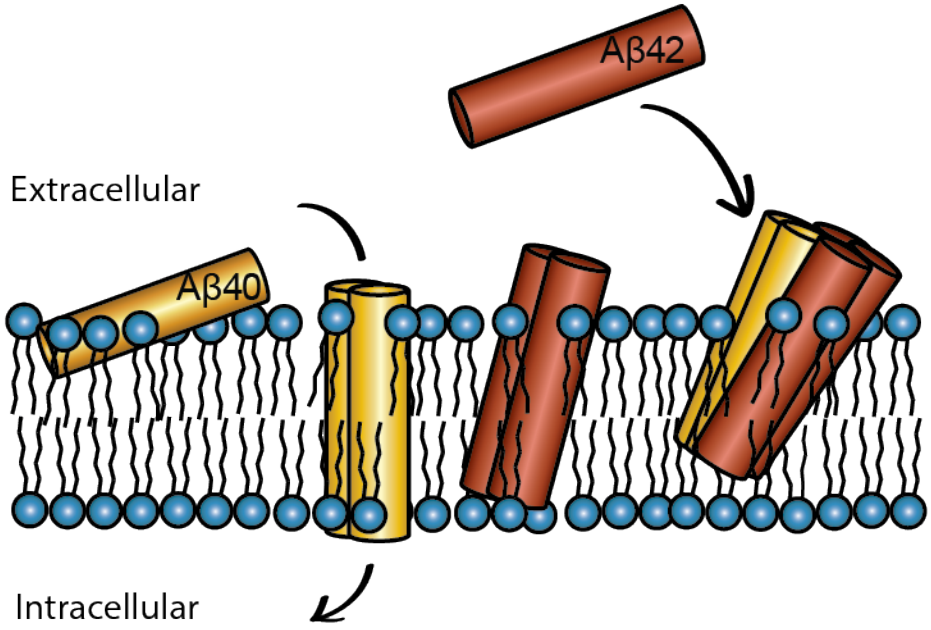

Figure 5-7. Hypothesis that explains how Aβ40 and Aβ42 interact on the cell membrane. Aβ40 dimer is more likely to form a fully transmembrane structure than Aβ42; therefore Aβ40 can be transported from extracellular to intracellular more easily than Aβ42. As a result, Aβ40 oligomerizes or accumulates slower than Aβ42 on the cell membrane. When Aβ40 binds to Aβ42, an even less transmembrane conformation is formed, resulting in more difficult internalization process for the cell. As a result, the

mixed oligomer can aggregate on the cell surface faster than either Aβ40 or Aβ42, and the oligomerization for mixed oligomer is mainly via recruiting free Aβ42.

5-5 Future Directions

Reading thus far, you, who care about my research, must are aware that the growth of these Aβ aggregates is exclusively by addition of Aβ42. A strong cooperativity between Aβ40 and Aβ42 is revealed, where both pure protein forms very little aggregates larger than dimers, but where membrane bound Aβ40 can seed the addition of Aβ42 to form increasingly larger aggregates. Understanding whether these heterogeneous larger aggregates are more toxic than those homogeneous oligomers is another step forward for Alzheimer's research.

Calcium influx into the cell can be caused by binding of Aβ oligomers to the membrane, and this calcium leakage is a well known indicator for the cell toxicity (153, 184, 185). To compare the toxicity driven by homogeneous Aβ40, Aβ42 and heterogeneous Aβ, similar experiment described in Chapter 4 can be used; in addition to adding fluorescently labeled Aβ (Hilyte-555 and Hilyte-647), neuronal cells need to be loaded with the fluorescent calcium indicator Fluo4-AM (excitation at 488 nm). Therefore, membrane bound Aβ can be identified along with the corresponding cell toxicity.

Combining the fluorescence microscopy with electrophysiology experiments done on the brain slice (or a live brain) will make the current hypothesis more physiological relevant. The oligomers have been shown to potently inhibit long-term potentiation (LTP), enhance long-term depression (LTD) and reduce dendritic spine density in normal rodent hippocampus. The Aβ concentrations used in LTP and LTD can be as low as pM to nM (59), which is ideal for single molecule experiments. Multi-photon microscopy is often used to image thick samples such as the brain tissue. However, conventional fluorescent dyes (*e.g.* Alexa and Hilyte dyes) suffer from fast photobleaching upon multi-photon excitation. This results in difficulty in conducting single molecule studies. A photo-resistible small fluorescence molecule must be developed and conjugated to Aβ.

REFERENCES

1. Savonenko, A. V, T. Melnikova, A. Hiatt, T. Li, P.F. Worley, et al. 2012. Alzheimer's therapeutics: translation of preclinical science to clinical drug development. Neuropsychopharmacology. 37: 261–77.

2. Jin, M., N. Shepardson, T. Yang, G. Chen, D. Walsh, et al. 2011. Soluble amyloid -protein dimers isolated from Alzheimer cortex directly induce Tau hyperphosphorylation and neuritic degeneration. Proc. Natl. Acad. Sci. 108: 5819–24.

3. Haass, C., and D.J. Selkoe. 2007. Soluble protein oligomers in neurodegeneration: lessons from the Alzheimer's amyloid beta-peptide. Nat. Rev. Mol. Cell Biol. 8: 101–12.

4. Palop, J.J., and L. Mucke, Mucke. 2010. Amyloid-beta-induced neuronal dysfunction in Alzheimer's disease: from synapses toward neural networks. Nat. Neurosci. 13: 812–8.

5. Meilandt, W.J., G.-Q. Yu, J. Chin, E.D. Roberson, J.J. Palop, et al. 2008. Enkephalin elevations contribute to neuronal and behavioral impairments in a transgenic mouse model of Alzheimer's disease. J. Neurosci. 28: 5007–17.

6. Sanchez-Mejia, R.O., J.W. Newman, S. Toh, G.-Q. Yu, Y. Zhou, et al. 2008. Phospholipase A2 reduction ameliorates cognitive deficits in a mouse model of Alzheimer's disease. Nat. Neurosci. 11: 1311–8.

7. Bero, A.W., P. Yan, J.H. Roh, J.R. Cirrito, F.R. Stewart, et al. 2011. Neuronal activity regulates the regional vulnerability to amyloid-β deposition. Nat. Neurosci. 14: 750–6.

8. Wu, J., R.S. Petralia, H. Kurushima, H. Patel, M. Jung, et al. 2011. Arc/Arg3.1 regulates an endosomal pathway essential for activity-dependent β-amyloid generation. Cell. 147: 615–28.

9. Querfurth, H.W., and F.M. LaFerla. 2010. Alzheimer's disease. N. Engl. J. Med. 362: 329–44.

10. Kuperstein, I., K. Broersen, I. Benilova, J. Rozenski, W. Jonckheere, et al. 2010. Neurotoxicity of Alzheimer's disease Aβ peptides is induced by small changes in the Aβ42 to Aβ40 ratio. EMBO J. 29: 3408–20.

11. Pauwels, K., T.L. Williams, K.L. Morris, W. Jonckheere, A. Vandersteen, et al. 2012. Structural basis for increased toxicity of pathological aβ42:aβ40 ratios in Alzheimer disease. J. Biol. Chem. 287: 5650–60.

12. Jarrett, J.T., E.P. Berger, and P.T. Lansbury. 1993. The carboxy terminus of the beta amyloid protein is critical for the seeding of amyloid formation: implications for the pathogenesis of Alzheimer's disease. Biochemistry. 32: 4693–7.

13. Hasegawa, K., I. Yamaguchi, S. Omata, F. Gejyo, and H. Naiki. 1999. Interaction between A beta(1-42) and A beta(1-40) in Alzheimer's beta-amyloid fibril formation in vitro. Biochemistry. 38: 15514–21.

14. Bitan, G., S.S. Vollers, and D.B. Teplow. 2003. Elucidation of primary structure elements controlling early amyloid beta-protein oligomerization. J. Biol. Chem. 278: 34882–9.

15. Murray, M.M., S.L. Bernstein, V. Nyugen, M.M. Condron, D.B. Teplow, et al. 2009. Amyloid beta protein: Abeta40 inhibits Abeta42 oligomerization. J. Am. Chem. Soc. 131: 6316–7.

16. Bernstein, S.L., N.F. Dupuis, N.D. Lazo, T. Wyttenbach, M.M. Condron, et al. 2009. Amyloid-β protein oligomerization and the importance of tetramers and dodecamers in the aetiology of Alzheimer's disease. Nat. Chem. 1: 326–31.

17. Dahlgren, K.N., A.M. Manelli, W.B. Stine, L.K. Baker, G.A. Krafft, et al. 2002. Oligomeric and fibrillar species of amyloid-beta peptides differentially affect neuronal viability. J. Biol. Chem. 277: 32046–53.

18. Roher, A.E., J.D. Lowenson, S. Clarke, A.S. Woods, R.J. Cotter, et al. 1993. beta-Amyloid-(1-42) is a major component of cerebrovascular amyloid deposits: implications for the pathology of Alzheimer disease. Proc. Natl. Acad. Sci. U. S. A. 90: 10836–40.

19. Gravina, S.A., L. Ho, C.B. Eckman, K.E. Long, L. Otvos, et al. 1995. Amyloid beta protein (A beta) in Alzheimer's disease brain. Biochemical and immunocytochemical analysis with antibodies specific for forms ending at A beta 40 or A beta 42(43). J. Biol. Chem. 270: 7013–6.

20. Suzuki, N., T.T. Cheung, X.D. Cai, A. Odaka, L. Otvos, et al. 1994. An increased percentage of long amyloid beta protein secreted by familial amyloid beta protein precursor (beta APP717) mutants. Science. 264: 1336–40.

21. Iwatsubo, T., A. Odaka, N. Suzuki, H. Mizusawa, N. Nukina, et al. 1994. Visualization of Aβ42(43) and Aβ40 in senile plaques with end-specific Aβ monoclonals: Evidence that an initially deposited species is Aβ42(43). Neuron. 13: 45–53.

22. Younkin, S.G. 1995. Evidence that A beta 42 is the real culprit in Alzheimer's disease. Ann. Neurol. 37: 287–8.

23. Hou, L., H. Shao, Y. Zhang, H. Li, N.K. Menon, et al. 2004. Solution NMR studies of the A beta(1-40) and A beta(1-42) peptides establish that the Met35 oxidation state affects the mechanism of amyloid formation. J. Am. Chem. Soc. 126: 1992–2005.

24. Uversky, V.N. 2009. Intrinsic disorder in proteins associated with neurodegenerative diseases. Front. Biosci. (Landmark Ed. 14: 5188–238.

25. Ball, K.A., A.H. Phillips, P.S. Nerenberg, N.L. Fawzi, D.E. Wemmer, et al. 2011. Homogeneous and heterogeneous tertiary structure ensembles of amyloid-β peptides. Biochemistry. 50: 7612–28.

26. Tycko, R. 2011. Solid-state NMR studies of amyloid fibril structure. Annu. Rev. Phys. Chem. 62: 279–99.

27. Lührs, T., C. Ritter, M. Adrian, D. Riek-Loher, B. Bohrmann, et al. 2005. 3D structure of Alzheimer's amyloid-beta(1-42) fibrils. Proc. Natl. Acad. Sci. U. S. A. 102: 17342–7.

28. Petkova, A.T., Y. Ishii, J.J. Balbach, O.N. Antzutkin, R.D. Leapman, et al. 2002. A structural model for Alzheimer's beta -amyloid fibrils based on experimental constraints from solid state NMR. Proc. Natl. Acad. Sci. U. S. A. 99: 16742–7.

29. Antzutkin, O.N., R.D. Leapman, J.J. Balbach, and R. Tycko. 2002. Supramolecular structural constraints on Alzheimer's beta-amyloid fibrils from electron microscopy and solid-state nuclear magnetic resonance. Biochemistry. 41: 15436–50.

30. Malinchik, S.B., H. Inouye, K.E. Szumowski, and D.A. Kirschner. 1998. Structural analysis of Alzheimer's beta(1-40) amyloid: protofilament assembly of tubular fibrils. Biophys. J. 74: 537–45.

31. Stromer, T., and L.C. Serpell. 2005. Structure and morphology of the Alzheimer's amyloid fibril. Microsc. Res. Tech. 67: 210–7.

32. Ball, K.A., A.H. Phillips, D.E. Wemmer, and T. Head-Gordon. 2013. Differences in β-strand Populations of Monomeric Aβ40 and Aβ42. Biophys. J. 104: 2714–2724.

33. Roychaudhuri, R., M. Yang, A. Deshpande, G.M. Cole, S. Frautschy, et al. 2013. C-terminal turn stability determines assembly differences between Aβ40 and Aβ42. J. Mol. Biol. 425: 292–308.

34. Bitan, G., M.D. Kirkitadze, A. Lomakin, S.S. Vollers, G.B. Benedek, et al. 2003. Amyloid beta -protein (Abeta) assembly: Abeta 40 and Abeta 42 oligomerize through distinct pathways. Proc. Natl. Acad. Sci. U. S. A. 100: 330–5.

35. Maji, S.K., R.R. Ogorzalek Loo, M. Inayathullah, S.M. Spring, S.S. Vollers, et al. 2009. Amino acid position-specific contributions to amyloid beta-protein oligomerization. J. Biol. Chem. 284: 23580–91.

36. Lazo, N.D., M.A. Grant, M.C. Condron, A.C. Rigby, and D.B. Teplow. 2005. On the nucleation of amyloid beta-protein monomer folding. Protein Sci. 14: 1581–96.

37. Wong, P.T., J.A. Schauerte, K.C. Wisser, H. Ding, E.L. Lee, et al. 2009. Amyloid-beta membrane binding and permeabilization are distinct processes influenced separately by membrane charge and fluidity. J. Mol. Biol. 386: 81–96.

38. Ogawa, M., M. Tsukuda, T. Yamaguchi, K. Ikeda, T. Okada, et al. 2011. Ganglioside-mediated aggregation of amyloid β-proteins (Aβ): comparison between Aβ-(1-42) and Aβ-(1-40). J. Neurochem. 116: 851–7.

39. Aisenbrey, C., T. Borowik, R. Byström, M. Bokvist, F. Lindström, et al. 2008. How is protein aggregation in amyloidogenic diseases modulated by biological membranes? Eur. Biophys. J. 37: 247–55.

40. Byström, R., C. Aisenbrey, T. Borowik, M. Bokvist, F. Lindström, et al. 2008. Disordered proteins: biological membranes as two-dimensional aggregation matrices. Cell Biochem. Biophys. 52: 175–89.

41. Hebda, J.A., and A.D. Miranker. 2009. The interplay of catalysis and toxicity by amyloid intermediates on lipid bilayers: insights from type II diabetes. Annu. Rev. Biophys. 38: 125–52.

42. Matsuzaki, K., S.A. Jayasinghe, and R. Langen. 2007. Membrane interaction of islet amyloid polypeptide. Biochim. Biophys. Acta - Biomembr. 1768: 2002–2009.

43. Chi, E.Y., C. Ege, A. Winans, J. Majewski, G. Wu, et al. 2008. Lipid membrane templates the ordering and induces the fibrillogenesis of Alzheimer's disease amyloid-beta peptide. Proteins. 72: 1–24.

44. Busciglio, J., A. Pelsman, C. Wong, G. Pigino, M. Yuan, et al. 2002. Altered metabolism of the amyloid beta precursor protein is associated with mitochondrial dysfunction in Down's syndrome. Neuron. 33: 677–88.

45. Selkoe, D.J. 2001. Alzheimer's disease: genes, proteins, and therapy. Physiol. Rev. 81: 741–66.

46. Tanzi, R.E., and L. Bertram. 2005. Twenty years of the Alzheimer's disease amyloid hypothesis: a genetic perspective. Cell. 120: 545–55.

47. Lue, L.F., Y.M. Kuo, A.E. Roher, L. Brachova, Y. Shen, et al. 1999. Soluble amyloid beta peptide concentration as a predictor of synaptic change in Alzheimer's disease. Am. J. Pathol. 155: 853–62.

48. McLean, C.A., R.A. Cherny, F.W. Fraser, S.J. Fuller, M.J. Smith, et al. 1999. Soluble pool of Abeta amyloid as a determinant of severity of neurodegeneration in Alzheimer's disease. Ann. Neurol. 46: 860–6.

49. Wang, J., D.W. Dickson, J.Q. Trojanowski, and V.M. Lee. 1999. The levels of soluble versus insoluble brain Abeta distinguish Alzheimer's disease from normal and pathologic aging. Exp. Neurol. 158: 328–37.

50. Klein, W.L., G.A. Krafft, and C.E. Finch. 2001. Targeting small Abeta oligomers: the solution to an Alzheimer's disease conundrum? Trends Neurosci. 24: 219–24.

51. Glabe, C.G. 2008. Structural classification of toxic amyloid oligomers. J. Biol. Chem. 283: 29639–43.

52. Tomic, J.L., A. Pensalfini, E. Head, and C.G. Glabe. 2009. Soluble fibrillar oligomer levels are elevated in Alzheimer's disease brain and correlate with cognitive dysfunction. Neurobiol. Dis. 35: 352–8.

53. Mc Donald, J.M., G.M. Savva, C. Brayne, A.T. Welzel, G. Forster, et al. 2010. The presence of sodium dodecyl sulphate-stable Abeta dimers is strongly associated with Alzheimer-type dementia. Brain. 133: 1328–41.

54. Terry, R.D., E. Masliah, D.P. Salmon, N. Butters, R. DeTeresa, et al. 1991. Physical basis of cognitive alterations in Alzheimer's disease: synapse loss is the major correlate of cognitive impairment. Ann. Neurol. 30: 572–80.

55. Price, J.L., and J.C. Morris. 1999. Tangles and plaques in nondemented aging and "preclinical" Alzheimer's disease. Ann. Neurol. 45: 358–68.

56. Aizenstein, H.J., R.D. Nebes, J.A. Saxton, J.C. Price, C.A. Mathis, et al. 2008. Frequent amyloid deposition without significant cognitive impairment among the elderly. Arch. Neurol. 65: 1509–17.

57. Reiman, E.M., K. Chen, X. Liu, D. Bandy, M. Yu, et al. 2009. Fibrillar amyloid-beta burden in cognitively normal people at 3 levels of genetic risk for Alzheimer's disease. Proc. Natl. Acad. Sci. U. S. A. 106: 6820–5.

58. Martins, I.C., I. Kuperstein, H. Wilkinson, E. Maes, M. Vanbrabant, et al. 2008. Lipids revert inert Abeta amyloid fibrils to neurotoxic protofibrils that affect learning in mice. EMBO J. 27: 224–33.

59. Shankar, G.M., S. Li, T.H. Mehta, A. Garcia-Munoz, N.E. Shepardson, et al. 2008. Amyloid-beta protein dimers isolated directly from Alzheimer's brains impair synaptic plasticity and memory. Nat. Med. 14: 837–42.

60. O'Nuallain, B., D.B. Freir, A.J. Nicoll, E. Risse, N. Ferguson, et al. 2010. Amyloid -Protein Dimers Rapidly Form Stable Synaptotoxic Protofibrils. J. Neurosci. 30: 14411–14419.

61. Ono, K., M.M. Condron, and D.B. Teplow. 2009. Structure-neurotoxicity relationships of amyloid beta-protein oligomers. Proc. Natl. Acad. Sci. U. S. A. 106: 14745–50.

62. Lesné, S., M.T. Koh, L. Kotilinek, R. Kayed, C.G. Glabe, et al. 2006. A specific amyloid-beta protein assembly in the brain impairs memory. Nature. 440: 352–7.

63. Lambert, M.P., A.K. Barlow, B.A. Chromy, C. Edwards, R. Freed, et al. 1998. Diffusible, nonfibrillar ligands derived from Abeta1-42 are potent central nervous system neurotoxins. Proc. Natl. Acad. Sci. U. S. A. 95: 6448–53.

64. Gong, Y., L. Chang, K.L. Viola, P.N. Lacor, M.P. Lambert, et al. 2003. Alzheimer's disease-affected brain: presence of oligomeric A beta ligands (ADDLs) suggests a molecular basis for reversible memory loss. Proc. Natl. Acad. Sci. U. S. A. 100: 10417–22.

65. Lacor, P.N., M.C. Buniel, P.W. Furlow, A.S. Clemente, P.T. Velasco, et al. 2007. Abeta oligomer-induced aberrations in synapse composition, shape, and density provide a molecular basis for loss of connectivity in Alzheimer's disease. J. Neurosci. 27: 796–807.

66. Lashuel, H.A., D. Hartley, B.M. Petre, T. Walz, and P.T. Lansbury. 2002. Neurodegenerative disease: amyloid pores from pathogenic mutations. Nature. 418: 291.

67. Hepler, R.W., K.M. Grimm, D.D. Nahas, R. Breese, E.C. Dodson, et al. 2006. Solution state characterization of amyloid beta-derived diffusible ligands. Biochemistry. 45: 15157–67.

68. Lin, H., R. Bhatia, and R. Lal. 2001. Amyloid beta protein forms ion channels: implications for Alzheimer's disease pathophysiology. FASEB J. 15: 2433–44.

69. Kagan, B.L., R. Azimov, and R. Azimova. 2004. Amyloid peptide channels. J. Membr. Biol. 202: 1–10.

70. Arispe, N., E. Rojas, and H.B. Pollard. 1993. Alzheimer disease amyloid beta protein forms calcium channels in bilayer membranes: blockade by tromethamine and aluminum. Proc. Natl. Acad. Sci. U. S. A. 90: 567–71.

71. Arispe, N., H.B. Pollard, and E. Rojas. 1993. Giant multilevel cation channels formed by Alzheimer disease amyloid beta-protein [A beta P-(1-40)] in bilayer membranes. Proc. Natl. Acad. Sci. U. S. A. 90: 10573–7.

72. Arispe, N., H.B. Pollard, and E. Rojas. 1996. Zn2+ interaction with Alzheimer amyloid beta protein calcium channels. Proc. Natl. Acad. Sci. 93: 1710–1715.

73. Mirzabekov, T.A., M.C. Lin, and B.L. Kagan. 1996. Pore formation by the cytotoxic islet amyloid peptide amylin. J. Biol. Chem. 271: 1988–92.

74. POLLARD, H.B., E. ROJAS, and N. ARISPE. 1993. A New Hypothesis for the Mechanism of Amyloid Toxicity, Based on the Calcium Channel Activity of Amyloid β Protein (AβP) in Phospholipid Bilayer Membranes. Ann. N. Y. Acad. Sci. 695: 165–168.

75. Volles, M.J., S.-J. Lee, J.-C. Rochet, M.D. Shtilerman, T.T. Ding, et al. 2001. Vesicle Permeabilization by Protofibrillar α-Synuclein: Implications for the Pathogenesis and Treatment of Parkinson's Disease †. Biochemistry. 40: 7812–7819.

76. Volles, M.J., and P.T. Lansbury. 2002. Vesicle Permeabilization by Protofibrillar α-Synuclein Is Sensitive to Parkinson's Disease-Linked Mutations and Occurs by a Pore-like Mechanism †. Biochemistry. 41: 4595–4602.

77. Kim, H.-Y., M.-K. Cho, A. Kumar, E. Maier, C. Siebenhaar, et al. 2009. Structural properties of pore-forming oligomers of alpha-synuclein. J. Am. Chem. Soc. 131: 17482–9.

78. Monoi, H., S. Futaki, S. Kugimiya, H. Minakata, and K. Yoshihara. 2000. Poly-l-Glutamine Forms Cation Channels: Relevance to the Pathogenesis of the Polyglutamine Diseases. Biophys. J. 78: 2892–2899.

79. Kourie, J.I., P. V Farrelly, and C.L. Henry. 2001. Channel activity of deamidated isoforms of prion protein fragment 106-126 in planar lipid bilayers. J. Neurosci. Res. 66: 214–20.

80. Quist, A., I. Doudevski, H. Lin, R. Azimova, D. Ng, et al. 2005. Amyloid ion channels: a common structural link for protein-misfolding disease. Proc. Natl. Acad. Sci. U. S. A. 102: 10427–32.

81. Lashuel, H.A., and P.T. Lansbury. 2006. Are amyloid diseases caused by protein aggregates that mimic bacterial pore-forming toxins? Q. Rev. Biophys. 39: 167–201.

82. Hajieva, P., C. Kuhlmann, H.J. Luhmann, and C. Behl. 2009. Impaired calcium homeostasis in aged hippocampal neurons. .

83. Lashuel, H.A., D.M. Hartley, B.M. Petre, J.S. Wall, M.N. Simon, et al. 2003. Mixtures of Wild-type and a Pathogenic (E22G) Form of Aβ40 in Vitro Accumulate Protofibrils, Including Amyloid Pores. J. Mol. Biol. 332: 795–808.

84. Kayed, R., Y. Sokolov, B. Edmonds, T.M. McIntire, S.C. Milton, et al. 2004. Permeabilization of lipid bilayers is a common conformation-dependent activity of soluble amyloid oligomers in protein misfolding diseases. J. Biol. Chem. 279: 46363–6.

85. Sokolov, Y., J.A. Kozak, R. Kayed, A. Chanturiya, C. Glabe, et al. 2006. Soluble amyloid oligomers increase bilayer conductance by altering dielectric structure. J. Gen. Physiol. 128: 637–47.

86. Valincius, G., F. Heinrich, R. Budvytyte, D.J. Vanderah, D.J. McGillivray, et al. 2008. Soluble amyloid beta-oligomers affect dielectric membrane properties by bilayer insertion and domain formation: implications for cell toxicity. Biophys. J. 95: 4845–61.

87. Sparr, E., M.F.M. Engel, D. V. Sakharov, M. Sprong, J. Jacobs, et al. 2004. Islet amyloid polypeptide-induced membrane leakage involves uptake of lipids by forming amyloid fibers. .

88. Domanov, Y.A., and P.K.J. Kinnunen. 2008. Islet Amyloid Polypeptide Forms Rigid Lipid–Protein Amyloid Fibrils on Supported Phospholipid Bilayers. J. Mol. Biol. 376: 42–54.

89. Rausch, J.M., J.R. Marks, R. Rathinakumar, and W.C. Wimley. 2007. Beta-sheet pore-forming peptides selected from a rational combinatorial library: mechanism of pore formation in lipid vesicles and activity in biological membranes. Biochemistry. 46: 12124–39.

90. Huang, H.W. 2000. Action of Antimicrobial Peptides: Two-State Model †. Biochemistry. 39: 8347–8352.

91. Bechinger, B., and K. Lohner. 2006. Detergent-like actions of linear amphipathic cationic antimicrobial peptides. Biochim. Biophys. Acta - Biomembr. 1758: 1529–1539.

92. Decker, H., S. Jürgensen, M.F. Adrover, J. Brito-Moreira, T.R. Bomfim, et al. 2010. N-methyl-D-aspartate receptors are required for synaptic targeting of Alzheimer's toxic amyloid-β peptide oligomers. J. Neurochem. 115: 1520–9.

93. De Felice, F.G., P.T. Velasco, M.P. Lambert, K. Viola, S.J. Fernandez, et al. 2007. Abeta oligomers induce neuronal oxidative stress through an N-methyl-D-aspartate receptor-dependent mechanism that is blocked by the Alzheimer drug memantine. J. Biol. Chem. 282: 11590–601.

94. Wang, H.Y., D.H. Lee, M.R. D'Andrea, P.A. Peterson, R.P. Shank, et al. 2000. beta-Amyloid(1-42) binds to alpha7 nicotinic acetylcholine receptor with high affinity. Implications for Alzheimer's disease pathology. J. Biol. Chem. 275: 5626–32.

95. Cissé, M., B. Halabisky, J. Harris, N. Devidze, D.B. Dubal, et al. 2011. Reversing EphB2 depletion rescues cognitive functions in Alzheimer model. Nature. 469: 47–52.

96. Srikanth, V., A. Maczurek, T. Phan, M. Steele, B. Westcott, et al. 2011. Advanced glycation endproducts and their receptor RAGE in Alzheimer's disease. Neurobiol. Aging. 32: 763–77.

97. Simakova, O., and N.J. Arispe. 2007. The cell-selective neurotoxicity of the Alzheimer's Abeta peptide is determined by surface phosphatidylserine and cytosolic ATP levels. Membrane binding is required for Abeta toxicity. J. Neurosci. 27: 13719–29.

98. Kawahara, M., N. Arispe, Y. Kuroda, and E. Rojas. 1997. Alzheimer's disease amyloid beta-protein forms Zn(2+)-sensitive, cation-selective channels across excised membrane patches from hypothalamic neurons. Biophys. J. 73: 67–75.

99. Jo, J., D.J. Whitcomb, K.M. Olsen, T.L. Kerrigan, S.-C. Lo, et al. 2011. Aβ(1-42) inhibition of LTP is mediated by a signaling pathway involving caspase-3, Akt1 and GSK-3β. Nat. Neurosci. 14: 545–7.

100. Li, S., M. Jin, T. Koeglsperger, N.E. Shepardson, G.M. Shankar, et al. 2011. Soluble Aβ oligomers inhibit long-term potentiation through a mechanism involving excessive activation of extrasynaptic NR2B-containing NMDA receptors. J. Neurosci. 31: 6627–38.

101. Renner, M., P.N. Lacor, P.T. Velasco, J. Xu, A. Contractor, et al. 2010. Deleterious effects of amyloid beta oligomers acting as an extracellular scaffold for mGluR5. Neuron. 66: 739–54.

102. Rönicke, R., M. Mikhaylova, S. Rönicke, J. Meinhardt, U.H. Schröder, et al. 2011. Early neuronal dysfunction by amyloid β oligomers depends on activation of NR2B-containing NMDA receptors. Neurobiol. Aging. 32: 2219–28.

103. Camandola, S., and M.P. Mattson. 2011. Aberrant subcellular neuronal calcium regulation in aging and Alzheimer's disease. Biochim. Biophys. Acta. 1813: 965–73.

104. Decker, H., K.Y. Lo, S.M. Unger, S.T. Ferreira, and M.A. Silverman. 2010. Amyloid-beta peptide oligomers disrupt axonal transport through an NMDA receptor-dependent mechanism that is mediated by glycogen synthase kinase 3beta in primary cultured hippocampal neurons. J. Neurosci. 30: 9166–71.

105. Du, H., L. Guo, F. Fang, D. Chen, A.A. Sosunov, et al. 2008. Cyclophilin D deficiency attenuates mitochondrial and neuronal perturbation and ameliorates learning and memory in Alzheimer's disease. Nat. Med. 14: 1097–105.

106. Sheng, Z.-H., and Q. Cai. 2012. Mitochondrial transport in neurons: impact on synaptic homeostasis and neurodegeneration. Nat. Rev. Neurosci. 13: 77–93.

107. Vossel, K.A., K. Zhang, J. Brodbeck, A.C. Daub, P. Sharma, et al. 2010. Tau reduction prevents Abeta-induced defects in axonal transport. Science. 330: 198.

108. Butterfield, S.M., and H.A. Lashuel. 2010. Amyloidogenic protein-membrane interactions: mechanistic insight from model systems. Angew. Chem. Int. Ed. Engl. 49: 5628–54.

109. Duff, K., C. Eckman, C. Zehr, X. Yu, C.M. Prada, et al. 1996. Increased amyloid-beta42(43) in brains of mice expressing mutant presenilin 1. Nature. 383: 710–3.

110. Scheuner, D., C. Eckman, M. Jensen, X. Song, M. Citron, et al. 1996. Secreted amyloid beta-protein similar to that in the senile plaques of Alzheimer's disease is increased in vivo by the presenilin 1 and 2 and APP mutations linked to familial Alzheimer's disease. Nat. Med. 2: 864–70.

111. Bentahir, M., O. Nyabi, J. Verhamme, A. Tolia, K. Horré, et al. 2006. Presenilin clinical mutations can affect gamma-secretase activity by different mechanisms. J. Neurochem. 96: 732–42.

112. De Strooper, B. 2007. Loss-of-function presenilin mutations in Alzheimer disease. Talking Point on the role of presenilin mutations in Alzheimer disease. EMBO Rep. 8: 141–6.

113. Hellström-Lindahl, E., M. Viitanen, and A. Marutle. 2009. Comparison of Abeta levels in the brain of familial and sporadic Alzheimer's disease. Neurochem. Int. 55: 243–52.

114. Citron, M., D. Westaway, W. Xia, G. Carlson, T. Diehl, et al. 1997. Mutant presenilins of Alzheimer's disease increase production of 42-residue amyloid beta-protein in both transfected cells and transgenic mice. Nat. Med. 3: 67–72.

115. Mann, D.M., T. Iwatsubo, N.J. Cairns, P.L. Lantos, D. Nochlin, et al. 1996. Amyloid beta protein (Abeta) deposition in chromosome 14-linked Alzheimer's disease: predominance of Abeta42(43). Ann. Neurol. 40: 149–56.

116. Wang, R., B. Wang, W. He, and H. Zheng. 2006. Wild-type presenilin 1 protects against Alzheimer disease mutation-induced amyloid pathology. J. Biol. Chem. 281: 15330–6.

117. Kim, J., L. Onstead, S. Randle, R. Price, L. Smithson, et al. 2007. Abeta40 inhibits amyloid deposition in vivo. J. Neurosci. 27: 627–33.

118. Jarrett, J.T., and P.T. Lansbury. 1993. Seeding "one-dimensional crystallization" of amyloid: a pathogenic mechanism in Alzheimer's disease and scrapie? Cell. 73: 1055–8.

119. Chen, Y.-R., and C.G. Glabe. 2006. Distinct early folding and aggregation properties of Alzheimer amyloid-beta peptides Abeta40 and Abeta42: stable trimer or tetramer formation by Abeta42. J. Biol. Chem. 281: 24414–22.

120. Schmidt, M., C. Sachse, W. Richter, C. Xu, M. Fändrich, et al. 2009. Comparison of Alzheimer Abeta(1-40) and Abeta(1-42) amyloid fibrils reveals similar protofilament structures. Proc. Natl. Acad. Sci. U. S. A. 106: 19813–8.

121. Kirschner, D.A., C. Abraham, and D.J. Selkoe. 1986. X-ray diffraction from intraneuronal paired helical filaments and extraneuronal amyloid fibers in Alzheimer disease indicates cross-beta conformation. Proc. Natl. Acad. Sci. U. S. A. 83: 503–7.

122. Sikorski, P., E.D.T. Atkins, and L.C. Serpell. 2003. Structure and Texture of Fibrous Crystals Formed by Alzheimer's Aβ(11–25) Peptide Fragment. Structure. 11: 915–926.

123. Yoshiike, Y., D.-H. Chui, T. Akagi, N. Tanaka, and A. Takashima. 2003. Specific compositions of amyloid-beta peptides as the determinant of toxic beta-aggregation. J. Biol. Chem. 278: 23648–55.

124. Snyder, S.W., U.S. Ladror, W.S. Wade, G.T. Wang, L.W. Barrett, et al. 1994. Amyloid-beta aggregation: selective inhibition of aggregation in mixtures of amyloid with different chain lengths. Biophys. J. 67: 1216–28.

125. Frost, D., P.M. Gorman, C.M. Yip, and A. Chakrabartty. 2003. Co-incorporation of A beta 40 and A beta 42 to form mixed pre-fibrillar aggregates. Eur. J. Biochem. 270: 654–63.

126. Jan, A., O. Gokce, R. Luthi-Carter, and H.A. Lashuel. 2008. The ratio of monomeric to aggregated forms of Abeta40 and Abeta42 is an important determinant of amyloid-beta aggregation, fibrillogenesis, and toxicity. J. Biol. Chem. 283: 28176–89.

127. Yan, Y., and C. Wang. 2007. Abeta40 protects non-toxic Abeta42 monomer from aggregation. J. Mol. Biol. 369: 909–16.

128. Ungureanu, A.-A., I. Benilova, M.J. Van Bael, C. Van Haesendonck, and C. Bartic. 2012. AFM investigation of the aggregation behavior of Alzheimer's disease Aβ peptides. Nanotechnol. (IEEE-NANO), 12th IEEE Conf. .

129. Viet, M.H., and M.S. Li. 2012. Amyloid peptide Aβ40 inhibits aggregation of Aβ42: evidence from molecular dynamics simulations. J. Chem. Phys. 136: 245105.

130. Walter, N.G., C.-Y. Huang, A.J. Manzo, and M.A. Sobhy. 2008. Do-it-yourself guide: how to use the modern single-molecule toolkit. Nat. Methods. 5: 475–89.

131. Vestergaard, M., T. Hamada, and M. Takagi. 2008. Using model membranes for the study of amyloid beta:lipid interactions and neurotoxicity. Biotechnol. Bioeng. 99: 753–63.

132. Mäler, L., and A. Gräslund. 2009. Artificial membrane models for the study of macromolecular delivery. Methods Mol. Biol. 480: 129–39.

133. Bütikofer, P., Z.W. Lin, D.T. Chiu, B. Lubin, and F.A. Kuypers. 1990. Transbilayer distribution and mobility of phosphatidylinositol in human red blood cells. J. Biol. Chem. 265: 16035–8.

134. Morrissey, J.H. Morrissey Lab Protocol for Preparing Phospholipid Vesicles (SUV) by Sonication. Avanti Polar Lipids website. .

135. Cremer, P.S., and S.G. Boxer. 1999. Formation and Spreading of Lipid Bilayers on Planar Glass Supports. J. Phys. Chem. B. 103: 2554–2559.

136. Mingeot-Leclercq, M.-P., M. Deleu, R. Brasseur, and Y.F. Dufrêne. 2008. Atomic force microscopy of supported lipid bilayers. Nat. Protoc. 3: 1654–9.

137. Axelrod, D. 1981. Cell-substrate contacts illuminated by total internal reflection fluorescence. J. Cell Biol. 89: 141–5.

138. AXELROD, D., D. KOPPEL, J. SCHLESSINGER, E. ELSON, and W. WEBB. 1976. Mobility measurement by analysis of fluorescence photobleaching recovery kinetics. Biophys. J. 16: 1055–1069.

139. SOUMPASIS, D. 1983. Theoretical analysis of fluorescence photobleaching recovery experiments. Biophys. J. 41: 95–97.

140. Veatch, S.L., B.B. Machta, S.A. Shelby, E.N. Chiang, D.A. Holowka, et al. 2012. Correlation functions quantify super-resolution images and estimate apparent clustering due to over-counting. PLoS One. 7: e31457.

141. Jaqaman, K., D. Loerke, M. Mettlen, H. Kuwata, S. Grinstein, et al. 2008. Robust single-particle tracking in live-cell time-lapse sequences. Nat. Methods. 5: 695–702.

142. Calamai, M., and F.S. Pavone. 2011. Single molecule tracking analysis reveals that the surface mobility of amyloid oligomers is driven by their conformational structure. J. Am. Chem. Soc. 133: 12001–8.

143. Ding, H., P.T. Wong, E.L. Lee, A. Gafni, and D.G. Steel. 2009. Determination of the oligomer size of amyloidogenic protein beta-amyloid(1-40) by single-molecule spectroscopy. Biophys. J. 97: 912–21.

144. Jiang, Y., N.R. Douglas, N.R. Conley, E.J. Miller, J. Frydman, et al. 2011. Sensing cooperativity in ATP hydrolysis for single multisubunit enzymes in solution. Proc. Natl. Acad. Sci. U. S. A. 108: 16962–7.

145. Benson, R.C., R.A. Meyer, M.E. Zaruba, and G.M. McKhann. 1979. Cellular autofluorescence--is it due to flavins? J. Histochem. Cytochem. 27: 44–8.

146. Aubin, J.E. 1979. Autofluorescence of viable cultured mammalian cells. J. Histochem. Cytochem. 27: 36–43.

147. Lundin, K., K. Blomberg, T. Nordström, and C. Lindqvist. 2001. Development of a time-resolved fluorescence resonance energy transfer assay (cell TR-FRET) for protein detection on intact cells. Anal. Biochem. 299: 92–7.

148. Zhou, V., S. Han, A. Brinker, H. Klock, J. Caldwell, et al. 2004. A time-resolved fluorescence resonance energy transfer-based HTS assay and a surface plasmon resonance-based binding assay for heat shock protein 90 inhibitors. Anal. Biochem. 331: 349–57.

149. Xu, Z., K. Nagashima, D. Sun, T. Rush, A. Northrup, et al. 2009. Development of high-throughput TR-FRET and AlphaScreen assays for identification of potent inhibitors of PDK1. J. Biomol. Screen. 14: 1257–62.

150. Roy, R., S. Hohng, and T. Ha. 2008. A practical guide to single-molecule FRET. Nat. Methods. 5: 507–16.

151. Strodel, B., J.W.L. Lee, C.S. Whittleston, and D.J. Wales. 2010. Transmembrane structures for Alzheimer's Aβ(1-42) oligomers. J. Am. Chem. Soc. 132: 13300–12.

152. Schauerte, J.A., P.T. Wong, K.C. Wisser, H. Ding, D.G. Steel, et al. 2010. Simultaneous single-molecule fluorescence and conductivity studies reveal distinct classes of Abeta species on lipid bilayers. Biochemistry. 49: 3031–9.

153. Johnson, R.D., J.A. Schauerte, K.C. Wisser, A. Gafni, and D.G. Steel. 2011. Direct Observation of Single Amyloid-β(1-40) Oligomers on Live Cells: Binding and Growth at Physiological Concentrations. PLoS One. 6: e23970.

154. Johnson, R.D., J.A. Schauerte, C.-C. Chang, K.C. Wisser, J.C. Althaus, et al. 2013. Single-Molecule Imaging Reveals Aβ42:Aβ40 Ratio-Dependent Oligomer Growth on Neuronal Processes. Biophys. J. 104: 894–903.

155. Lakowicz, J.R. 1999. Principles of Fluorescence Spectroscopy. (Kluwer Acad. Plenum Publ. New York). 2nd Ed. .

156. Bateman, D.A., J. McLaurin, and A. Chakrabartty. 2007. Requirement of aggregation propensity of Alzheimer amyloid peptides for neuronal cell surface binding. BMC Neurosci. 8: 29.

157. Chafekar, S.M., F. Baas, and W. Scheper. 2008. Oligomer-specific Abeta toxicity in cell models is mediated by selective uptake. Biochim. Biophys. Acta. 1782: 523–31.

158. Lee, S., N.H. Varvel, M.E. Konerth, G. Xu, A.E. Cardona, et al. 2010. CX3CR1 deficiency alters microglial activation and reduces beta-amyloid deposition in two Alzheimer's disease mouse models. Am. J. Pathol. 177: 2549–62.

159. Jakawich, S.K., H.B. Nasser, M.J. Strong, A.J. McCartney, A.S. Perez, et al. 2010. Local presynaptic activity gates homeostatic changes in presynaptic function driven by dendritic BDNF synthesis. Neuron. 68: 1143–58.

160. Ding, H., J.A. Schauerte, D.G. Steel, and A. Gafni. 2012. β-Amyloid (1-40) Peptide Interactions with Supported Phospholipid Membranes: A Single-Molecule Study. Biophys. J. 103: 1500–9.

161. Chang, C.-C., J.C. Althaus, C.J.L. Carruthers, M.A. Sutton, D.G. Steel, et al. 2013. Synergistic Interactions between Alzheimer's Aβ40 and Aβ42 on the Surface of Primary Neurons Revealed by Single Molecule Microscopy. PLoS One. 8: e82139.

162. Narayan, P., K.A. Ganzinger, J. McColl, L. Weimann, S. Meehan, et al. 2013. Single Molecule Characterization of the Interactions between Amyloid-β Peptides and the Membranes of Hippocampal Cells. J. Am. Chem. Soc. .

163. Nag, S., J. Chen, J. Irudayaraj, and S. Maiti. 2010. Measurement of the attachment and assembly of small amyloid-β oligomers on live cell membranes at physiological concentrations using single-molecule tools. Biophys. J. 99: 1969–75.

164. Nag, S., B. Sarkar, A. Bandyopadhyay, B. Sahoo, V.K.A. Sreenivasan, et al. 2011. Nature of the amyloid-beta monomer and the monomer-oligomer equilibrium. J. Biol. Chem. 286: 13827–33.

165. Saxton, M.J. 1997. Single-particle tracking: the distribution of diffusion coefficients. Biophys. J. 72: 1744–53.

166. Wieser, S., and G.J. Schütz. 2008. Tracking single molecules in the live cell plasma membrane-Do’s and Don't's. Methods. 46: 131–40.

167. Mobley, D.L., D.L. Cox, R.R.P. Singh, M.W. Maddox, and M.L. Longo. 2004. Modeling amyloid beta-peptide insertion into lipid bilayers. Biophys. J. 86: 3585–97.

168. Bitan, G., A. Lomakin, and D.B. Teplow. 2001. Amyloid beta-protein oligomerization: prenucleation interactions revealed by photo-induced cross-linking of unmodified proteins. J. Biol. Chem. 276: 35176–84.

169. Ishii, Y., T. Yoshida, T. Funatsu, T. Wazawa, and T. Yanagida. 1999. Fluorescence resonance energy transfer between single fluorophores attached to a coiled-coil protein in aqueous solution. Chem. Phys. 247: 163–173.

170. Kremer, J.J., and R.M. Murphy. 2003. Kinetics of adsorption of beta-amyloid peptide Abeta(1-40) to lipid bilayers. J. Biochem. Biophys. Methods. 57: 159–69.

171. Johnson, S.J., T.M. Bayerl, D.C. McDermott, G.W. Adam, A.R. Rennie, et al. 1991. Structure of an adsorbed dimyristoylphosphatidylcholine bilayer measured with specular reflection of neutrons. Biophys. J. 59: 289–94.

172. Huang, H.W. 2006. Molecular mechanism of antimicrobial peptides: the origin of cooperativity. Biochim. Biophys. Acta. 1758: 1292–302.

173. Hong, S., O. Quintero-Monzon, B.L. Ostaszewski, D.R. Podlisny, W.T. Cavanaugh, et al. 2011. Dynamic Analysis of Amyloid -Protein in Behaving Mice Reveals Opposing Changes in ISF versus Parenchymal A during Age-Related Plaque Formation. J. Neurosci. 31: 15861–15869.

174. Lee, M.-T., F.-Y. Chen, and H.W. Huang. 2004. Energetics of pore formation induced by membrane active peptides. Biochemistry. 43: 3590–9.

175. Omtri, R.S., M.W. Davidson, B. Arumugam, J.F. Poduslo, and K.K. Kandimalla. 2012. Differences in the Cellular Uptake and Intracellular Itineraries of Amyloid Beta Proteins 40 and 42: Ramifications for the Alzheimer's Drug Discovery. Mol. Pharm. 9: 1887–1897.

176. Benilova, I., E. Karran, and B. De Strooper. 2012. The toxic Aβ oligomer and Alzheimer's disease: an emperor in need of clothes. Nat. Neurosci. 15: 349–57.

177. Davis, C.H., and M.L. Berkowitz. 2010. A molecular dynamics study of the early stages of amyloid-beta(1-42) oligomerization: the role of lipid membranes. Proteins. 78: 2533–45.

178. Motter, R., C. Vigo-Pelfrey, D. Kholodenko, R. Barbour, K. Johnson-Wood, et al. 1995. Reduction of beta-amyloid peptide42 in the cerebrospinal fluid of patients with Alzheimer's disease. Ann. Neurol. 38: 643–8.

179. Fagan, A.M., M.A. Mintun, R.H. Mach, S.-Y. Lee, C.S. Dence, et al. 2006. Inverse relation between in vivo amyloid imaging load and cerebrospinal fluid Abeta42 in humans. Ann. Neurol. 59: 512–9.

180. Fagan, A.M., D. Head, A.R. Shah, D. Marcus, M. Mintun, et al. 2009. Decreased cerebrospinal fluid Abeta(42) correlates with brain atrophy in cognitively normal elderly. Ann. Neurol. 65: 176–83.

181. Shaw, L.M., H. Vanderstichele, M. Knapik-Czajka, C.M. Clark, P.S. Aisen, et al. 2009. Cerebrospinal fluid biomarker signature in Alzheimer's disease neuroimaging initiative subjects. Ann. Neurol. 65: 403–13.

182. Shoji, M., E. Matsubara, M. Kanai, M. Watanabe, T. Nakamura, et al. 1998. Combination assay of CSF tau, A beta 1-40 and A beta 1-42(43) as a biochemical marker of Alzheimer's disease. J. Neurol. Sci. 158: 134–40.

183. Fagan, A.M., C.M. Roe, C. Xiong, M.A. Mintun, J.C. Morris, et al. 2007. Cerebrospinal fluid tau/beta-amyloid(42) ratio as a prediction of cognitive decline in nondemented older adults. Arch. Neurol. 64: 343–9.

184. Demuro, A., E. Mina, R. Kayed, S.C. Milton, I. Parker, et al. 2005. Calcium dysregulation and membrane disruption as a ubiquitous neurotoxic mechanism of soluble amyloid oligomers. J. Biol. Chem. 280: 17294–300.

185. Simakova, O., and N.J. Arispe. 2006. Early and late cytotoxic effects of external application of the Alzheimer's Abeta result from the initial formation and function of Abeta ion channels. Biochemistry. 45: 5907–15.